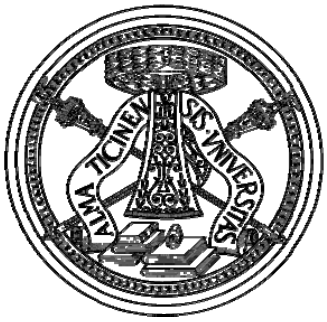

UNIVERSITA' DEGLI STUDI DI PAVIA
FACULTY OF ENGINEERING
DEPARTMENT OF ELECTRICAL, COMPUTER AND BIOMEDICAL ENGINEERING

PHD IN ELECTRONICS, COMPUTER SCIENCE AND ELECTRICAL ENGINEERING

Nicolò Delmonte

Advanced Technologies for SIW Passive Microwave Components

Tutor:
Prof. Maurizio Bozzi

XXXIII cycle, 2020

Contents

List of Figures

List of Tables

Chapter 1

Introduction

In the last few decades, the development of new microwave and mm-wave technologies has been driven by an ever increasing demand for reliable and high speed connectivity.

In particular, wireless communication technologies play a vital role in the telecommunications department. For example, due to the Internet of Things (IoT) phenomenon, it has been predicted that over 28 billion wireless devices will be connected by the end of 2021 [1]. New wireless technologies and infrastructure will be required in order to sustain this growth in the following years [2]. Next-generation communication standards like the 5G are imposing new requirements on the features and characteristics of microwave components. For example, 5G connections operate at higher frequencies compared to previous generation cellphone standards [3], and 5G base station antennas now require beam-forming capabilities [4] in order to satisfy the growing requirements of the wireless infrastructure.

Another source of innovation is the advent of autonomous and semi-autonomous driving systems. Self driving cars require a wide array of sensors in order to safely operate [5, 6]. In this context, mm-wave radars offer various advantages over optical-based systems (LIDAR and video cameras), such as long range detection, accurate relative speed measurement and robust operation in bad weather conditions [7, 8]. Moreover, most autonomous driving systems will employ wireless communication links in order to exchange traffic information between nearby vehicles [9].

In this framework, microwave components should possess a few properties:

- they should be inexpensive to fabricate
- they should be compact and easy to integrate
- they should exhibit low loss and high electromagnetic performance

These characteristics allow to maximize the application range of any microwave component. A small, inexpensive device can be easily integrated

in a larger amount of systems, and high electromagnetic performance aids with the compliance with the radio standards of choice.

Planar microwave technologies have been the main choice for the creation of passive components for consumer applications since the half of the last century. The most well-known and used planar transmission line topologies are the microstrip [10] and the coplanar line [11]. Thanks to their low size and compact form factor, these technologies allow for a very high level of miniaturization. Many fabrication techniques for planar components have been designed and refined over the decades, such as the Printed Circuit Board (PCB) [12] and the Low-Temperature Co-fired Ceramic (LTCC) [13]. Complex planar circuit networks can be connected using multilayer substrate topologies, and some technologies give the option of integrating these structures in semiconductor chips [14]. Over time, the cost of these fabrication techniques has gone down, making planar structures generally inexpensive.

Overall, planar microwave technologies offer an extremely high level of design flexibility. However, they still present some drawbacks. Namely, planar transmission lines tend to be more lossy compared to other traditional technologies. Electromagnetic losses have an impact on the performance of any microwave component, ranging from a degradation of the insertion loss and the selectivity of a filter to the increase of the phase noise of an oscillator. Moreover, most planar topologies tend to be open: this means that they can easily suffer from parasitic coupling and external interference.

In applications where the electromagnetic performance of the components is the top design priority, such as the space and satellite sector or aviation radars, traditional non-planar microwave technologies see widespread use. For example, resonators based on metallic waveguide or coaxial transmission lines can reach very high quality factor values. The dielectric medium of non-planar structures is usually air or vacuum, which eliminate the losses inevitably introduced to planar topologies by the solid substrate materials. Non-planar devices typically demonstrate high power handling capabilities and offer complete electromagnetic shielding, resulting in high signal integrity.

The main problem of non-planar technologies is the size of their components. Due to their working principle, non-planar structure are large and bulky. They also require complex and expensive fabrication techniques, such as mechanical milling. Moreover, they require the design of specialized coupling structures in order to interface with other technologies, resulting in poor system integration. All these reason make non-planar technologies a poor choice for consumer applications.

In this context, the recently developed Substrate Integrated Waveguide (SIW) technology [15] offers an interesting combination between the efficiency and integration capabilities of planar topologies and the high electromagnetic performance of non-planar structures. An SIW structure is the

direct implementation of the classic rectangular waveguide topology on a planar substrate. In the last few years, the SIW technology has been the subject of intense academic research. This lead to the development of many different alternative SIW topologies which aim to improve various characteristics of the technology, such as reducing electromagnetic losses (Air-Filled SIW [16, 17]), increasing the usable frequency bandwidth (Substrate Integrated Ridge Waveguide [18]) and increasing component miniaturization (Substrate Integrated Folded Waveguide [19] and Half-Mode SIW [20]).

The SIW technology has the potential to create the high performance, low cost and highly integrable components required by the current and upcoming wireless technologies, especially at higher frequency bands (mm-wave). The aim of this research is to provide a contribution to the current landscape of microwave components by expanding the application range of the SIW technology. This work opens (chapter 2) by briefly presenting the topology and loss characteristics of the SIW and Half-Mode SIW technologies. The Half-Mode technique is an effective size reduction method, particularly useful at low frequency where the dimension of SIW components is significant. However, its application results in an increase of electromagnetic losses. Chapter 3 presents a systematic study of various compact SIW resonator topologies derived from the Half-Mode technology. In addition, a technique that limits the degradation of the performance is also presented. Chapter 4 shows some special SIW filter topologies, designed to obtain particular responses such as additional transmission zeroes or wider spurious-free bandwidths. In chapter 5, a particular type of reconfigurable array is proposed. This configuration is designed to minimize the amount of control elements required to obtain beam-steering capabilities. This array topology is used to create two antennas for 5G applications based on SIW radiators. Closing thoughts are then provided in chapter 6. The appendix will present some additional microwave components designed during the PhD activity period which are unrelated to the SIW technology.

References

[1] Ericsson, "Cellular networks for massive IoT: Enabling low power wide area applications," 2016.

[2] S. Li, L. D. Xu, and S. Zhao, "5G internet of things: A survey," *Journal of Industrial Information Integration*, vol. 10, pp. 1 – 9, 2018.

[3] M. Agiwal, A. Roy, and N. Saxena, "Next generation 5G wireless networks: A comprehensive survey," *IEEE Communications Surveys and Tutorials*, vol. 18, no. 3, pp. 1617–1655, 2016.

[4] R. S. Yarrabothu and P. Telagathoti, "Massive MIMO and beamforming techniques of 5G networks," *International Journal of Engineering and Advanced Technology*, vol. 9, 2019.

[5] C. Badue, R. Guidolini, R. V. Carneiro, P. Azevedo, V. B. Cardoso, A. Forechi, L. F. R. Jesus, R. F. Berriel, T. M. Paixão, F. W. Mutz, T. Oliveira-Santos, and A. F. de Souza, "Self-driving cars: A survey," *CoRR*, vol. abs/1901.04407, 2019.

[6] J. Kocić, N. Jovičić, and V. Drndarević, "Sensors and sensor fusion in autonomous vehicles," in *2018 26th Telecommunications Forum (TELFOR)*, pp. 420–425, 2018.

[7] S. M. Patole, M. Torlak, D. Wang, and M. Ali, "Automotive radars: A review of signal processing techniques," *IEEE Signal Processing Magazine*, vol. 34, no. 2, pp. 22–35, 2017.

[8] S. Sun, A. P. Petropulu, and H. V. Poor, "MIMO radar for advanced driver-assistance systems and autonomous driving: Advantages and challenges," *IEEE Signal Processing Magazine*, vol. 37, pp. 98–117, July 2020.

[9] J. Wang, J. Liu, and N. Kato, "Networking and communications in autonomous driving: A survey," *IEEE Communications Surveys and Tutorials*, vol. 21, no. 2, pp. 1243–1274, 2019.

[10] D. D. Grieg and H. F. Engelmann, "Microstrip-a new transmission technique for the klilomegacycle range," *Proceedings of the IRE*, vol. 40, no. 12, pp. 1644–1650, 1952.

[11] C. P. Wen, "Coplanar waveguide: A surface strip transmission line suitable for nonreciprocal gyromagnetic device applications," *IEEE Transactions on Microwave Theory and Techniques*, vol. 17, no. 12, pp. 1087–1090, 1969.

[12] C. Coombs, "Printed circuits handbook," 2007.

[13] L. Devlin, G. Pearson, J. Pittock, and B. Hunt, "RF and microwave components in LTCC," 2001.

[14] D. N. McQuiddy, J. W. Wassel, J. B. LaGrange, and W. R. Wisseman, "Monolithic microwave integrated circuits: An historical perspective," *IEEE Transactions on Microwave Theory and Techniques*, vol. 32, no. 9, pp. 997–1008, 1984.

[15] D. Deslandes and K. Wu, "Integrated microstrip and rectangular waveguide in planar form," *IEEE Microwave and Wireless Components Letters*, vol. 11, no. 2, pp. 68–70, 2001.

[16] F. Parment, A. Ghiotto, T. Vuong, J. Duchamp, and K. Wu, "Air-filled substrate integrated waveguide for low-loss and high power-handling millimeter-wave substrate integrated circuits," *IEEE Transactions on Microwave Theory and Techniques*, vol. 63, no. 4, pp. 1228–1238, 2015.

[17] L. Silvestri, A. Ghiotto, C. Tomassoni, M. Boziz, and L. Perregrini, "Partially air-filled substrate integrated waveguide filters with full control of transmission zeros," *IEEE Transactions on Microwave Theory and Techniques*, vol. 67, no. 9, pp. 3673–3682, 2019.

[18] M. Bozzi, S. A. Winkler, and K. Wu, "Broadband and compact ridge substrate-integrated waveguides," *IET Microwaves, Antennas Propagation*, vol. 4, no. 11, pp. 1965–1973, 2010.

[19] N. Grigoropoulos, B. Sanz-Izquierdo, and P. R. Young, "Substrate integrated folded waveguides (SIFW) and filters," *IEEE Microwave and Wireless Components Letters*, vol. 15, no. 12, pp. 829–831, 2005.

[20] Q. Lai, C. Fumeaux, W. Hong, and R. Vahldieck, "Characterization of the propagation properties of the half-mode substrate integrated waveguide," *IEEE Transactions on Microwave Theory and Techniques*, vol. 57, no. 8, pp. 1996–2004, 2009.

Chapter 2

The Substrate Integrated Waveguide (SIW) technology

The *Substrate Integrated Waveguide* (SIW) is a particularly interesting type of transmission line technology. Compared to other traditional types of planar transmission lines (such as the microstrip, stripline, etc.), the SIW technology allows for the realization of completely shielded, low cost and low losses microwave components. Since its introduction in the early 2000s [1], the SIW technology has been the subject of a high amount of academic research. The technology has been applied on a wide spectrum of applications, ranging from sensors [2, 3, 4], to antennas [5, 6], filters [7, 8, 9], and oscillators [10].

The main drawback of the SIW technology is the substrate area occupation: compared with other planar technologies, SIW-based component have a larger footprint. In order to mitigate this problem, a few techniques have been proposed. Those based on the Half-Mode technology [11] are particularly effective, and provide both a reduction in component size and in fabrication complexity. However, as a trade-off, the electromagnetic shielding is lost and the losses increase compared to the standard SIW technology.

This chapter shows a study on the performance and losses of SIW resonators based from the technologies derived from the Half-Mode SIW technique. Resonators are an ideal choice for the study of losses of the technology, since they are simple to design, fabricate and measure. Moreover, resonators are use as the base building block of a large amount of more complex devices like filters, and their characteristics dictate the maximum achievable performance. First, a brief overview of the SIW technology will be presented. Then, ther study of the various resonator topologies will be shown. Finally, a few filters will be presented as example of applications of the compact resonator topologies.

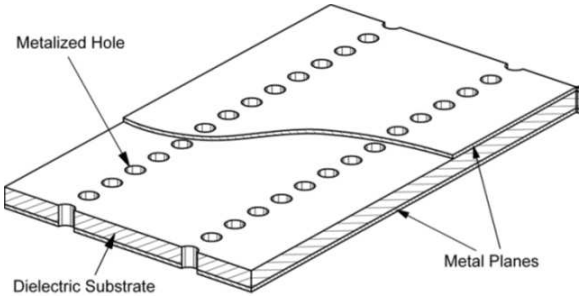

Figure 2.1: Topology of the Substrate Integrated Waveguide transmission line

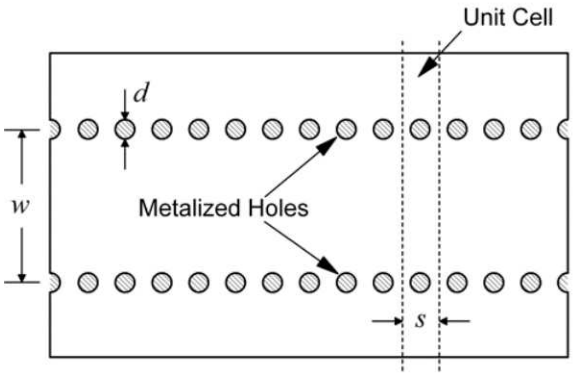

Figure 2.2: Top view of the SIW transmission line

2.1 Substrate Integrated Waveguide technology

The topology of a simple SIW transmission line is shown in figure 2.1. It consists of a layer of dielectric substrate material, metallized on both sides. On the sides of the structure, two parallel rows of metallized holes can be found. These holes, commonly called *vias* or *posts*, connect the top and bottom metal layer of the structure. In this way, the electromagnetic signal can travel inside the substrate and is confined between the two lines of posts.

The design of the SIW transmission line has been inspired by the traditional empty rectangular waveguide technology. Essentially, the SIW technology is a planar implementation of the rectangular waveguide [12]. For this reason, the electromagnetic characteristics of the two technologies are very similar. In fact, the simplest and one of the most used methods to analyse or design an SIW based device is the *equivalent rectangular waveguide model*. The method consists in the synthesis of a rectangular waveguide based on the physical dimensions of the SIW line. Since the properties of the rectangular waveguide are known analytically, they can be computed easily and provide a good approximation for the behaviour of the SIW transmission

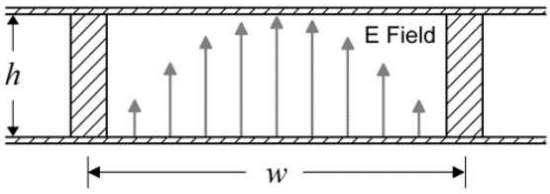

Figure 2.3: Side view of the SIW transmission line and fundamental mode field distribution

line.

Figure 2.2 shows an overhead view of the SIW transmission line. The topology is periodic, and can be completely represented using a few physical dimensions: the post diameter d; the distance between the two via rows w, and the distance between the centres of two consecutive posts s. The other two important parameters are the thickness of the substrate h and its dielectric permittivity ϵ_r. Given these dimensions, the width of the equivalent rectangular transmission line is:

$$w_{eff} = w - \frac{d^2}{0.95s} \tag{2.1}$$

This approximation is accurate as long as $s < 4d$, which covers the vast majority of cases. The value w_{eff} is also called the *effective width* of the transmission line. Since the SIW transmission line has a single conductor, it supports the propagation of TE modes. The fundamental mode is the TE_{10}, and is shown in figure 2.3. Its cutoff frequency is simply computed as:

$$f_{10} = \frac{c}{2w_{eff}\sqrt{\epsilon_r}} \tag{2.2}$$

where c is the speed of light constant. A particular characteristic of the SIW waveguide technology is a reduced number of supported propagation modes compared to the traditional rectangular waveguide. As it is shown in figure 2.2, the side walls of the SIW topology are approximated by the rows of metallized vias. The gaps between the vias make it so the modal current can't flow in the longitudinal direction. For this reason, only the TE_{n0} modes of the rectangular waveguide are supported by the SIW topology.

A very important factor in evaluating the performance of a transmission line technology is electromagnetic losses. SIW has three loss mechanisms: dielectric losses α_d, conductor losses α_c, and radiation losses α_r. The overall loss contribution is the sum of the three terms:

$$\alpha_{TOT}(f) = \alpha_d + \alpha_d + \alpha_r \tag{2.3}$$

The dielectric losses mainly depend on the dielectric loss tangent of the material used as the substrate. Using the equivalent rectangular waveguide model, they can be computed as:

$$\alpha_d(f) = \frac{\pi f \sqrt{\epsilon_r}}{c\sqrt{1-\left(\frac{f_c}{f}\right)^2}} \tan\delta \tag{2.4}$$

where $\tan\delta$ is the dielectric loss tangent, and f_c the modal cutoff frequency. These losses are not affected by the position of the metallized posts.

Conductor losses come from the ohmic losses of the metals in the structure. The equivalent rectangular waveguide model gives:

$$\alpha_c(f) = \frac{\sqrt{\pi f \epsilon_0 \epsilon_r}}{h\sqrt{\sigma_c}} \cdot \frac{1+2\left(\frac{f_c}{f}\right)^2 \frac{h}{w_{eff}}}{\sqrt{1-\left(\frac{f_c}{f}\right)^2}} \tag{2.5}$$

where σ_c is the conductivity of the metal and ϵ_0 is the free space dielectric conductivity. In this case, losses tend to be inversely proportional to the substrate thickness h, as increasing the height of the structure decreases the modal current density.

Radiation losses do not have a counterpart in the equivalent rectangular waveguide model. They arise from the imperfect shielding given by the gaps in the side rows of vias. They strongly depend on the post diameter d and post distance s. However, it has been shown [12] that these contributions are negligible compared to the other two terms as long as $s/d < 2.5$.

The metallic vias at the side of the SIW transmission line form a periodic structure. These kind of structures are known to experience band-gap effects, which could disrupt the performance of the device. These effects depend on the periodicity of the structure (in this case, the distance between adjacent metallic vias). In practice, band-gap effects appear at frequencies much higher than the intended single mode operation bandwidth of any SIW waveguide.

2.2 Half-Mode SIW technology

The physical properties of the SIW transmission line can be exploited in order to obtain considerable size reduction. The electric fields of the TE_{10} fundamental mode of an SIW line (figure 2.3) present an even axis of symmetry along the middle of the structure. This symmetry could be supported by a magnetic wall boundary condition. Given the usually low thickness h of the structure and the presence of the dielectric, a strong capacitive effect is generated in the middle of the topology. This capacitive effect gives a good approximation of a magnetic wall boundary. For this reason, it is

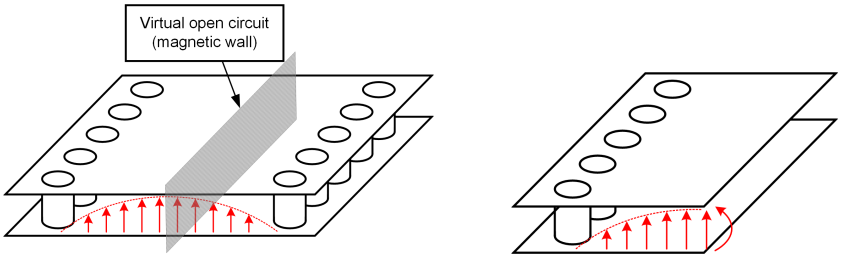

Figure 2.4: Synthesis of the Half-Mode SIW technology

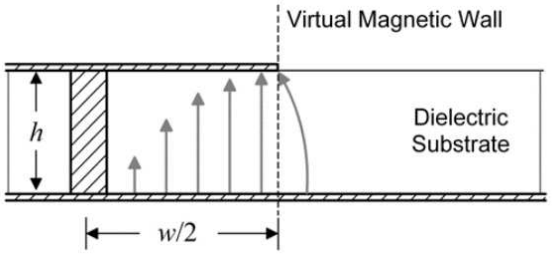

Figure 2.5: Side view of the Half-Mode SIW transmission line and fundamental mode field distribution

ideally possible to remove half of the metallic structure while still retaining the same propagation characteristics. The resulting topology is called *Half-Mode SIW* (HMSIW) [11].

Figure 2.5 shows the cross-section of an HMSIW transmission line. The removal of an entire row of vias and of half of the top metal layer results in an effective 50% decrease in the footprint of the device. The capacitive effect confines most of the modal fields inside the structure; however, since the magnetic boundary along the middle of the structure is not perfect, some fringing fields appear near the open side of the component. This results in an additional radiation loss contribution. The amount of losses strongly depend on the thicknesses and dielectric permittivity of the dielectric, but the overall attenuation is usually close to the standard SIW counterpart except at lower frequencies. In a small band near the lower cut-off, losses increase sharply since the open side of the structure tends to act like a radiating slot.

Due to their working principle, HMSIW structures only support propagating modes with even symmetry. This means that the modal spectrum of HMSIW structures is reduced compared to standard SIW. The only propagating modes are TE_{n0} with odd n. As a consequence, HMSIW structures have a broader single mode bandwidth.

References

[1] D. Deslandes and K. Wu, "Integrated microstrip and rectangular waveguide in planar form," *IEEE Microwave and Wireless Components Letters*, vol. 11, no. 2, pp. 68–70, 2001.

[2] E. Silavwe, N. Somjit, and I. D. Robertson, "A microfluidic-integrated SIW lab-on-substrate sensor for microliter liquid characterization," *IEEE Sensors Journal*, vol. 16, no. 21, pp. 7628–7635, 2016.

[3] C. Chen, J. Xu, and Y. Yao, "SIW resonator humidity sensor based on layered black phosphorus," *Electronics Letters*, vol. 53, no. 4, pp. 249–251, 2017.

[4] T. R. Jones, M. H. Zarifi, and M. Daneshmand, "Miniaturized quarter-mode substrate integrated cavity resonators for humidity sensing," *IEEE Microwave and Wireless Components Letters*, vol. 27, no. 7, pp. 612–614, 2017.

[5] Q. Wu, J. Yin, C. Yu, H. Wang, and W. Hong, "Broadband planar SIW cavity-backed slot antennas aided by unbalanced shorting vias," *IEEE Antennas and Wireless Propagation Letters*, vol. 18, no. 2, pp. 363–367, 2019.

[6] S. Priya, K. Kumar, S. Dwari, and M. K. Mandal, "Circularly polarized self-diplexing SIW cavity backed slot antennas," *IEEE Transactions on Antennas and Propagation*, vol. 68, no. 3, pp. 2387–2392, 2020.

[7] Q. Liu, D. Zhou, Y. Zhang, D. Zhang, and D. Lv, "Substrate integrated waveguide bandpass filters in box-like topology with bypass and direct couplings in diagonal cross-coupling path," *IEEE Transactions on Microwave Theory and Techniques*, vol. 67, no. 3, pp. 1014–1022, 2019.

[8] P. Chu, W. Hong, K. Wang, H. Tang, Z. Hao, J. Chen, and K. Wu, "Balanced substrate integrated waveguide filter," *IEEE Transactions on Microwave Theory and Techniques*, vol. 62, no. 4, pp. 824–831, 2014.

[9] K. Zhou, C. Zhou, and W. Wu, "Substrate-integrated waveguide dual-mode dual-band bandpass filters with widely controllable bandwidth ratios," *IEEE Transactions on Microwave Theory and Techniques*, vol. 65, no. 10, pp. 3801–3812, 2017.

[10] R. Zhang, J. Zhou, Z. Yu, and B. Yang, "A low phase noise feedback oscillator based on SIW bandpass response power divider," *IEEE Microwave and Wireless Components Letters*, vol. 28, no. 2, pp. 153–155, 2018.

[11] W. Hong, B. Liu, Y. Wang, Q. Lai, H. Tang, X. X. Yin, Y. D. Dong, Y. Zhang, and K. Wu, "Half mode substrate integrated waveguide: A new guided wave structure for microwave and millimeter wave application," in *2006 Joint 31st International Conference on Infrared Millimeter Waves and 14th International Conference on Teraherz Electronics*, pp. 219–219, 2006.

[12] R. Garg, I. Bahl, and M. Bozzi, *Microstrip Lines and Slotlines*. Artech House, 2013.

Chapter 3

Performance study of compact SIW resonator topologies

A resonator is a particular kind of microwave component, whose function is to store electromagnetic energy at particular frequencies. Resonators are particularly interesting since they serve as the basis for a large amount of more complex microwave devices, such as filters, multiplexers and oscillators. A common method used to create microwave resonators consists in taking isolated stretches of a transmission line. When this method is applied to the SIW technology, the resulting component is called an SIW cavity resonator.

The study presented in this chapter shows a comparison between the unloaded quality factor of a traditional SIW cavity and a few different compact topologies derived from the Half-Mode technique. The values have been obtained using the commercial FEM-based simulation software *ANSYS Electronic Desktop*. For each topology, a set of resonators based on different substrates and working at different frequencies has been designed. In this way, it is possible to characterize the behaviour of the various topologies in different conditions. The substrates chosen are the commercially available *Taconic TLY-5* ($\epsilon_r = 2.2$, $\tan\delta = 0.0009$) and the *Taconic CER-10* ($\epsilon_r = 10$, $\tan\delta = 0.0035$). The thickness of the substrates have been varied between 10 mil (0.254 mm) and 50 mil (1.27 mm). For each combination of substrate type and thickness, two resonators working respectively at 4 GHz and 10 GHz have been designed for every topology.

3.1 Resonator properties

The behaviour of any microwave resonator can be described using two sets of parameters: the *resonant mode frequencies* (f_r) and their corresponding *unloaded quality factors* (Q_u).

The energy of a resonator is stored in its internal electromagnetic fields; these fields can persist in the structure only by forming specific patterns. These patterns are called *resonant modes*, and each mode exists at a specific frequency. For this reason, resonators can only accept and store energy at certain frequencies, which are called *resonant mode frequencies* f_r. All microwave resonators have an infinite amount of resonant modes. In practice, only the first few modes with the lowest resonant frequency are used for the operation of microwave devices. The resonant mode with the lowest frequency value is called the *fundamental mode* of the structure.

Even if a resonator is left completely isolated, the energy stored inside of it will tend to decay over time. This is due to the electromagnetic loss mechanisms that are found in the structure. The *unloaded quality factor* Q_u is a parameter that quantifies the total amount of losses of a resonator. The relation between losses and quality factor is inversely proportional, so that a resonator with lower losses will have a value of Q_u higher compared to one with high losses. It is important to note that the shape of the resonant mode field pattern may affect the amount of losses in a structure. For this reason, each resonant mode of a resonator is usually associated with a different value of Q_u.

The quality factor Q_u is particularly important when dealing with the practical applications of microwave resonators. In general, devices built using resonators with lower Q_u will have poorer electromagnetic performance (for example, filters will have higher insertion loss and lower selectivity, oscillators will have higher phase noise etc.). The quality factor may determine the choice of a certain device fabrication technology, along with other parameters such as miniaturization, ease of integration and costs.

There are a few ways to calculate the quality factor of a resonator. For some topologies, the modal field distribution is known analytically, which makes it possible to directly compute the value of Q_u from the physical dimensions of the device. Using the equivalent rectangular waveguide model it is possible to obtain a good approximation of the quality factor for traditional SIW resonators. However, this is not a viable option in the case of the compact topologies derived from the Half-Mode technique. A more general approach is the use of numerical methods. Typically, electromagnetic simulator software use techniques such as the *finite element method* (FEM) or the *boundary element method* (BEM) to subdivide the topology of a resonator and compute the properties of its resonant fields. Numerical methods offer a large amount of flexibility on the structures that can be analysed. Finally, a physical prototype can be realized and measured. This method is more costly and time consuming than the others, and for this reason is normally only used to validate the results obtained from other sources.

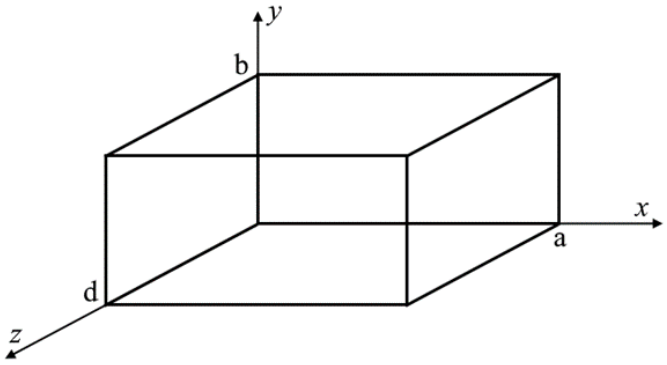

Figure 3.1: Topology of a rectangular cavity resonator

3.1.1 Analysis of the rectangular cavity resonator model

As it was discussed previously, the equivalent rectangular cavity model provides a good approximation for the behaviour of classic SIW structures. The study of the rectangular cavity resonator can provide an useful insight on the performance of SIW devices, making it simpler to find the optimal design conditions for these structures.

The topology of a rectangular cavity resonator is shown in figure 3.1 [1]. It consists of a tract of length d of a rectangular waveguide, with width a and height b. The fundamental resonant mode of the resonator is derived from the TE_{10} propagating mode of the waveguide. The fundamental resonant frequency of the structure is:

$$f_{110} = \frac{1}{2\pi\sqrt{\epsilon\mu}}\sqrt{\left(\frac{\pi}{a}\right)^2 + \left(\frac{\pi}{d}\right)^2} \tag{3.1}$$

It can be seen that the resonant frequency depends on the physical dimensions of the cavity (width a and length d) and on the electromagnetic properties of the filling dielectric (permittivity ϵ and permeability μ). In general, to obtain a low resonant frequency it is either necessary to increase the size of the cavity (higher values of a and d) or load the resonator with a dielectric with high permittivity ϵ.

Obtaining the unloaded quality factor Q_u involves the calculation of all the power loss contribution. By definition, the unloaded quality factor is given by:

$$Q_u = 2\pi f \frac{W_{TOT}}{P_{loss}} \tag{3.2}$$

where W_{TOT} is the total amount of energy stored in the resonator, and P_{loss} is the average power dissipated by the structure. In order to simplify the analysis, each independent source of electromagnetic loss can be studied

individually. In this way, each physical loss mechanism can be assigned an individual partial quality factor value. These partial quality factors can then be combined to obtain the actual Q_u of the resonator. The rectangular cavity resonator has two electromagnetic loss sources: dissipation in the dielectric and ohmic losses in the metal.

Dielectric losses only depend on the properties of the material used to fill the cavity. The amount of dissipated power increases linearly with the stored energy. For this reason, the formula for the *dielectric quality factor* Q_d is:

$$Q_d = \frac{1}{\tan \delta} \tag{3.3}$$

where $\tan \delta$ is the loss tangent of the dielectric material. It can be noted that Q_d is completely independent from the physical dimensions of the cavity. In the case of traditional rectangular cavities, the resonator can be left empty, completely removing this loss contribution. However, SIW structures require a substrate to be fabricated. In this case, Q_d acts as acts as an upper boundary on the performance of all resonators built using a certain material.

Conductor losses come from the modal currents flowing on the metal walls of the cavity. Since ohmic losses depend on the square of the current density, the physical dimensions of the resonator can influence the total amount of dissipated power. The *conductor quality factor* Q_c is given by:

$$Q_c = \frac{(kad)^2 b\eta}{2\pi^2 R_S} \frac{1}{2a^3b + 2bd^3 + a^3d + ad^3} \tag{3.4}$$

where $k = 2\pi f\sqrt{\epsilon\mu}$ is the wavenumber of the dielectric, η is the characteristic impedance of the dielectric and R_S is the surface resistivity of the metal. As the size of the cavity becomes larger, conductor losses tend to get lower. In particular, Q_c becomes higher as the value of the resonator height b increases. This is particularly convenient, since the resonant frequency (equation 3.1) is independent from the parameter b. When dealing with SIW resonators, this means that thicker substrates will decrease conductor losses.

Compared to the traditional rectangular cavities, SIW structures have one additional loss contribution: power leakage through the gaps between the metallized vias. Just like in the case of transmission lines, if the gap is sufficiently small, these losses are negligible compared to the other contributions. However, all the compact resonator topologies derived from the Half-Mode technique have a large open side without any via. In this situation, an additional term of loss called *radiation quality factor* Q_r can be computed. There is no analytical formula to calculate Q_r, so it has to be obtained numerically.

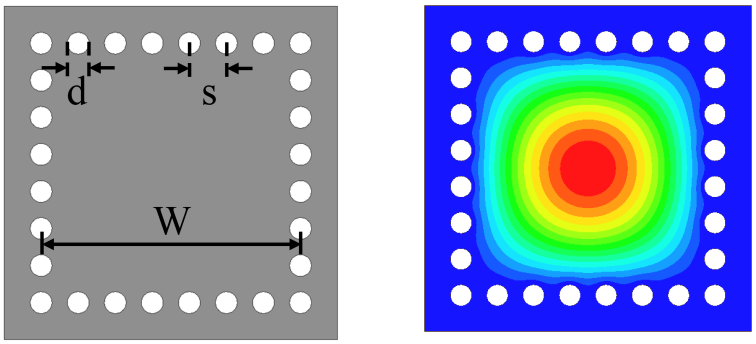

(a) (b)

Figure 3.2: Layout and resonant mode field distribution of the SIW resonator

In the end, the overall unloaded quality factor of a resonator is obtained by combining all the partial loss contributions:

$$\frac{1}{Q_u} = \frac{1}{Q_d} + \frac{1}{Q_c} + \frac{1}{Q_r} \tag{3.5}$$

3.1.2 SIW cavity resonator

The topology of a standard square SIW cavity resonator is shown in figure 3.2a. The area of the resonator is limited by four rows of metallized vias. Out of all the structures studied in this work, this is the one that most resembles a classic rectangular waveguide cavity, both for its shape and for its electromagnetic behaviour. As long as the distance between the metallized vias is sufficiently low, the resonant electromagnetic fields are tightly confined inside the walls of the cavity, and the structure can be assumed to be completely shielded.

The design of the resonator is made simple by the equivalent rectangular waveguide model (equations 2.1 and 3.1). The desired fundamental resonant frequency can be easily obtained by properly selecting the overall size of the resonator W. The physical parameters of the resonators employed in this study are shown in table 3.1. It can be noticed that the resonators designed on CER-10 substrate are significantly smaller than those based on TLY-5; the reason comes from the relative dielectric permeability ϵ_r of the materials, which is substantially higher in the case of CER-10. Note that the thickness of the substrate has no effect on the resonant frequency of he resonator.

In order to study the performance of these resonators, the quality factor of the resonant mode has to be computed. From the analysis of the rectangular cavity shown in the previous section, it is known that the physical parameters of the resonators have an effect on the losses of the structure. However, the cavity size W cannot be changed without modifying the reso-

nant frequency of the device. On the other hand, the via size d and distance s parameters have a very small impact on the behaviour of the resonator as long as the design rule shown previously is satisfied ($s < 2.5d$). As a result, the only physical dimension which can be modified is the thickness of the substrate h.

Table 3.2 shows the simulated unloaded quality factor of the SIW square resonators as the thickness of the substrate is changed. All the metal parts of the structure are defined as copper (conductivity $\sigma = 1.68 \times 10^{-8}\Omega \cdot m$). It can be seen that in every case, a taller substrate is associated with an higher value of Q, which corresponds to a lower amount of losses. Moreover, for any given substrate height, the quality factors of the resonators based on TLY-5 substrate are always higher than those made with CER-10. In order to understand the reasons behind these behaviours, it is particularly useful to study each physical loss mechanism individually. Form the analysis of the rectangular cavity, it is known that two loss contributions are present in the resonator: dielectric and conductor losses.

By using electromagnetic simulator software, it is easy to compute the amount of losses given by each single contribution. The simulated model can be modified in order to leave only one loss mechanism. For example, equation 3.3 shows that the dielectric losses of the cavity are only given by the value of loss tangent $\tan\delta$ of the substrate. For this reason, if the properties of the model are altered so that $\tan\delta = 0$, dielectric losses are completely removed from the simulation. On the other hand, ohmic losses can be removed by replacing all the metals of the structure with a perfect conductor. By leaving active only one loss mechanism at a time, the electromagnetic simulator will compute the quality factor related only to that specific source.

Using this technique, the partial dielectric quality factor Q_d and conductor quality factor Q_c have been computed for all the resonators. The results of the analysis is shown in the plots of figure 3.3. The radiation quality factor Q_r has not been computed since the traditional SIW cavities are assumed to be completely shielded. It can be easily noticed that the dielectric quality factor Q_d of TLY-5 resonators is much higher than that of CER-10 structures, since the loss tangent of the material is significantly lower. For this reason, the unloaded quality factor Q can reach much higher levels. Other than that, it can be seen that the conductor quality factor increases with the thickness of the substrate in all cases (as expected from equation 3.4).

From these results, it can be seen that the overall losses of SIW resonators can be minimized by employing thick substrates with low loss tangents. Meanwhile, materials with high relative dielectric permittivity can be exploited to reduce the dimensions of the components.

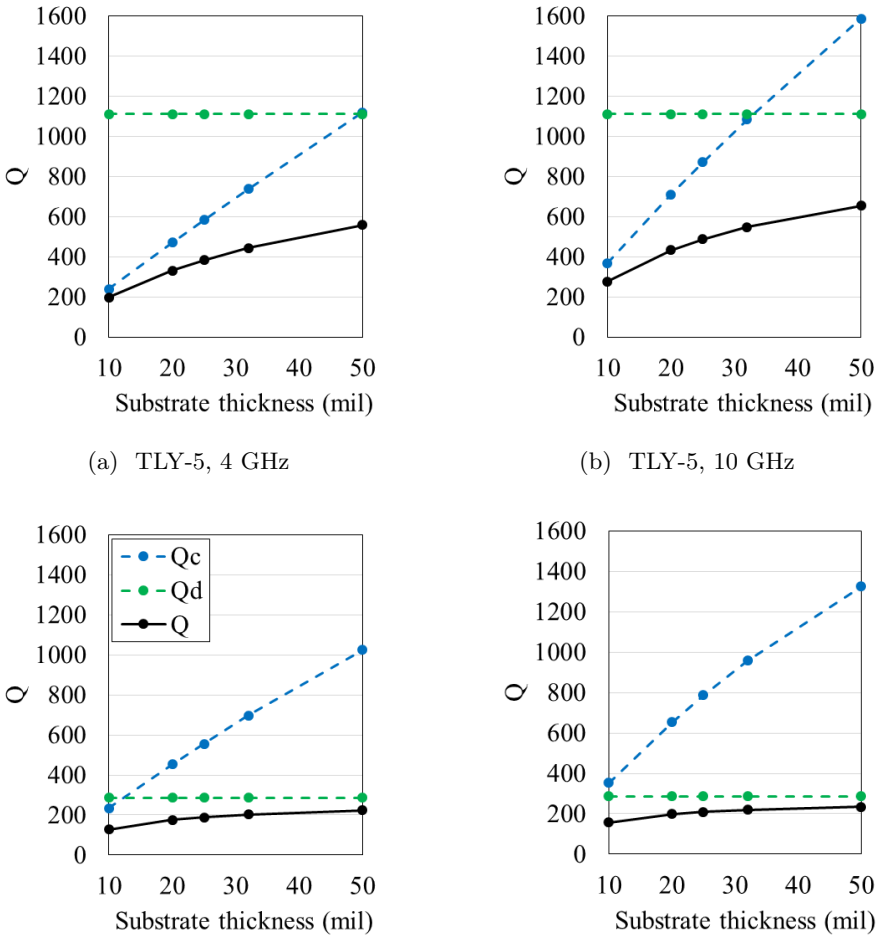

(a) TLY-5, 4 GHz

(b) TLY-5, 10 GHz

(c) CER-10, 4 GHz

(d) CER-10, 10 GHz

Figure 3.3: Effect of the substrate thickness on the loss contributions of the SIW resonator.
Q_c: conductor quality factor. Q_d: dielectric quality factor. Q: overall unloaded quality factor

Table 3.1: Design parameters of the SIW cavity resonators

	TLY-5 4 GHz	TLY-5 10 GHz	CER-10 4 GHz	CER-10 10 GHz
W	36.75 mm	15.4 mm	17.79 mm	7.42 mm
d	1.5 mm	1.5 mm	1.5 mm	1 mm
s	2.45 mm	2.2 mm	2.54 mm	1.48 mm

Table 3.2: Unloaded quality factors Q_u of the SIW cavity resonators

Substrate thickness	TLY-5 4 GHz	TLY-5 10 GHz	CER-10 4 GHz	CER-10 10 GHz
10 mil	197	277.2	128.9	158.1
20 mil	330.5	433.2	175.3	198.8
25 mil	382.4	488.2	188.7	209.6
32 mil	443.1	584.9	202.6	220
50 mil	557.5	653.4	223.4	235

3.1.3 Half-Mode cavity resonator

Looking at the square SIW cavity and its resonant mode from above, a symmetry axis can be noticed along the middle of the structure. Applying the Half-Mode technique consists in removing half of the metal layer of the structure: the resulting Half-Mode cavity is shown in figure 3.4. On the edge of the structure where no metallic posts are present, we find a capacitive effect due to the short distance between the top and bottom metallizations of the substrate; this capacitance will approximate a magnetic wall condition on that side of the structure. The symmetry of the square SIW cavity resonant mode can satisfy this boundary condition, and so the Half-Mode structure can resonate. Figure 3.4b shows the field distribution of the fundamental resonant mode of the Half-Mode cavity. While most of the electromagnetic energy stays inside the structure, the electric field tends to concentrate along the open side of the cavity. Around the same area, some fringing fields similar to those found on the edge of capacitors can also be found.

In theory, a Half-Mode cavity should resonate at the same frequency of a square SIW cavity of exactly twice the area; in practice, however, the fringing field effects will change the electrical length of the structure seen by the resonant mode, shifting it to a slightly lower frequency.

The Half-Mode cavity is an open structure. This means that some of the electromagnetic energy has the potential to be radiated away from the structure. Compared to a closed SIW cavity, radiation is an additional

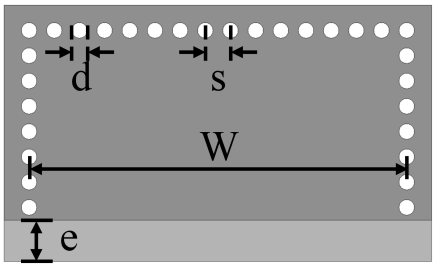

(a)

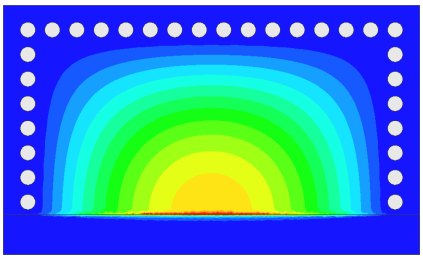

(b)

Figure 3.4: Layout and resonant mode field distribution of the Half-Mode SIW resonator

loss contribution that can heavily affect the overall unloaded quality factor. Looking at the Half-Mode topology, radiation may occur from the fringing fields that form on the open side of the device, a mechanism similar to the planar patch antenna. Some of the power can also leave the structure and travel inside the dielectric medium in the form of a surface wave. Effectively, a small radiating aperture is present at the open side of half-mode structures. Since the radiation efficiency is directly linked to the total area of the aperture, power losses in the cavity increase rapidly with the thickness of the substrate. Also, substrates with high dielectric constant present slightly lower radiation losses since the fields tend to be more confined inside the cavity. The mechanism of dissipation in the conductors of a Half-Mode cavity is the same of the normal SIW resonators. The Half-Mode structure conductor quality factor Q_c is a bit lower than the SIW counterparts because of the lower size of the overall device. Losses in the dielectric should be independent on the size and shape of the structure; however, due to the fringing field effect, part of the resonant mode is outside of the dielectric medium and lays in the air that surrounds the structure. For this reason the dielectric quality factor Q_d is slightly higher than the one of normal SIW structures and tends to increase with the substrate thickness, since the fields become less confined.

The most important feature of the Half-Mode SIW topology is the re-

Table 3.3: Design parameters of the Half-Mode SIW cavity resonators

	TLY-5 4 GHz	TLY-5 10 GHz	CER-10 4 GHz	CER-10 10 GHz
W	36.5 mm	15.2 mm	17.8 mm	7.42 mm
d	1.5 mm	1.5 mm	1.5 mm	1 mm
s	2.43 mm	2.17 mm	2.54 mm	1.48 mm
e	7 mm	5 mm	5 mm	3 mm

Table 3.4: Unloaded quality factors Q_u of the Half-Mode SIW cavity resonators

Substrate thickness	TLY-5 4 GHz	TLY-5 10 GHz	CER-10 4 GHz	CER-10 10 GHz
10 mil	122.5	139.8	106.4	106.6
20 mil	86.6	146.9	113.6	89.5
25 mil	72.5	135.2	109	78.5
32 mil	58.3	120.2	100.7	64.3
50 mil	37.8	94.5	79.6	37.8

duced footprint compared to classic square SIW cavities operating at the same frequency. As a trade-off, the lack of complete electromagnetic shielding means that the resonators have a lower quality factor due to radiation losses. The dimensions of the designed Half-Mode resonators are shown in table 3.3, while the calculated quality factors are shown in table 3.4.

While the quality factor of the normal SIW cavities grows steadily with the height of the substrate, in this case it tends to get lower. The graphs in figure 3.5 show the effect of the substrate thickness on the quality factor in more detail. Radiation has a very large impact on the performance of the resonators, being the dominant source of losses especially with the TLY-5 substrate, since it has a relatively low dielectric permittivity. The quality factor is particularly low at higher frequency since the open side of the structure appears larger in respect to the wavelength, increasing the radiation efficiency.

In conclusion, Half-Mode resonators are best used with thin substrates with high dielectric constant, in mid to low frequency applications. While they can save a significant amount of space compared to normal SIW components, they offer significantly lower quality factors even in the optimal conditions.

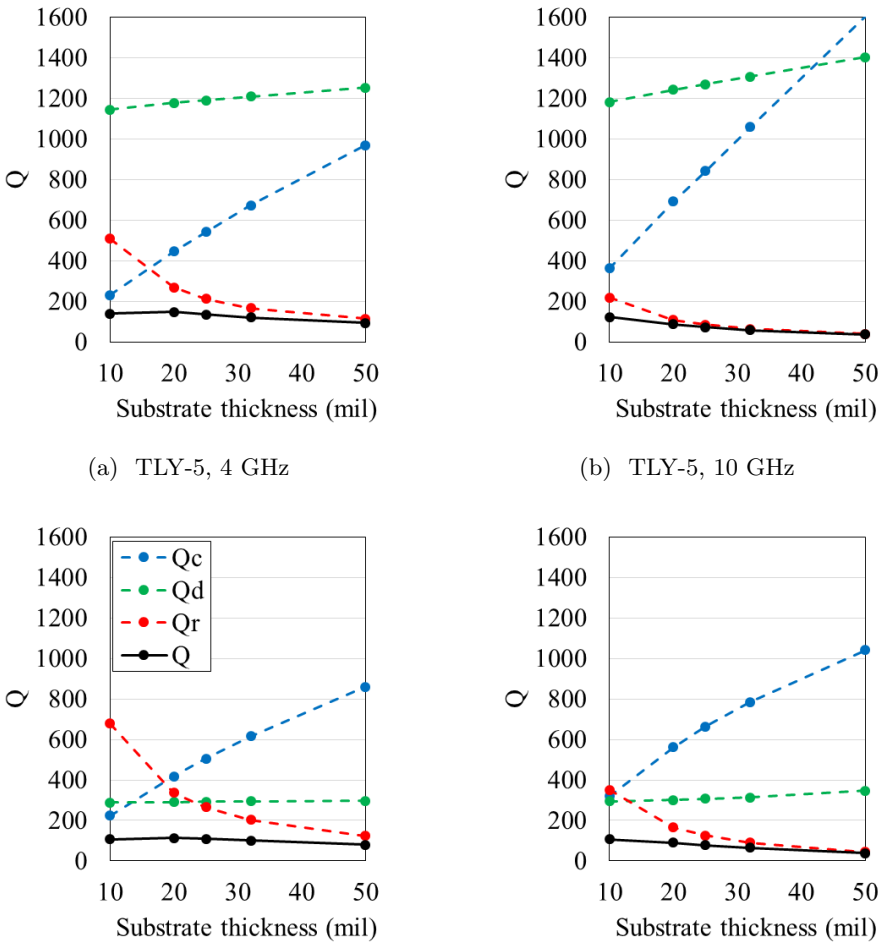

(a) TLY-5, 4 GHz

(b) TLY-5, 10 GHz

(c) CER-10, 4 GHz

(d) CER-10, 10 GHz

Figure 3.5: Effect of the substrate thickness on the loss contributions of the Half-Mode SIW resonator. Q_c: conductor quality factor. Q_d: dielectric quality factor. Q_r: radiation quality factor. Q: overall unloaded quality factor

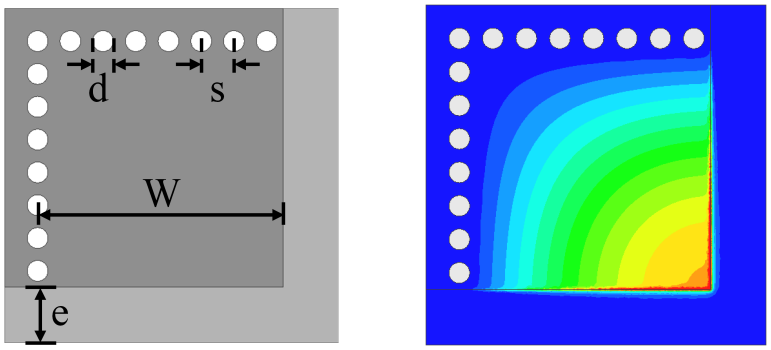

(a) (b)

Figure 3.6: Layout and resonant mode field distribution of the Quarter-Mode SIW resonator

3.1.4 Quarter-Mode cavity resonator

The resonant mode of the Half-Mode resonator topology (figure 2.5) presents an additional symmetry axis. By applying the same size reduction concept, it is possible to remove an additional part of metal layer, obtaining the Quarter-Mode resonator topology shown in figure 3.6. The Quarter-Mode topology is the natural evolution of the Half-Mode resonator, so they share many characteristics. The resonant frequency of the cavity is mainly controlled by the length w, and that parameter has to be adjusted depending on the substrate thickness because of the fringing fields on the open sides of the device. Working with the same substrate and at the same frequency, the value of w tends to be slightly lower than half the cavity length of the corresponding Half-Mode resonator.

Power loss comes from the same sources of the previous topologies. The small size of the cavity means that the conductor losses increase slightly, lowering a bit the quality factor of the contribution Q_c compared to the respective Half-Mode structure. Depending on the characteristics of the substrate, the resonant fields can be more or less confined inside the cavity. A less confined mode will lower the dielectric losses, since more of the fields lay outside the substrate, but will also increase the total radiated power.

The final physical parameters of all the designed resonators are shown in table 3.5, while the computed quality factors can be seen in table 3.6. The charts in figure 3.7 show the quality factor loss contributions in more detail. In the case of the 4 GHz CER-10 resonator, the radiation quality factor Q_r is significantly higher than in the corresponding Half-Mode structure for this reason the overall unloaded quality factor is higher across the whole range of values of the substrate thickness. The topology works well with the high dielectric constant of the CER-10 substrate, meaning that

Table 3.5: Design parameters of the Quarter-Mode SIW cavity resonators

	TLY-5 4 GHz	TLY-5 10 GHz	CER-10 4 GHz	CER-10 10 GHz
W	18.1 mm	7.7 mm	8.9 mm	3.7 mm
d	1.5 mm	1.5 mm	1.5 mm	1 mm
s	2.41 mm	2.2 mm	2.54 mm	1.48 mm
e	7 mm	5 mm	5 mm	2.5 mm

Table 3.6: Unloaded quality factors Q_u of the Quarter-Mode SIW cavity resonators

Substrate thickness	TLY-5 4 GHz	TLY-5 10 GHz	CER-10 4 GHz	CER-10 10 GHz
10 mil	117.6	69.6	114.9	105.5
20 mil	101.4	40.6	135.1	83.4
25 mil	91	31.4	137.8	70.2
32 mil	76.2	24.2	128.8	57.4
50 mil	53.1	14	106.2	32.4

the radiated power is lower given the lower intensity of the fringing fields. However, this effect becomes less important as the frequency increases: the quality factor of the 10 GHz CER-10 resonator is on the same level of its respective half-mode version. On the other hand, the structures based on TLY-5 show poor electromagnetic field confinement. For this reason, the dielectric quality factor Q_d rapidly increases with the height of the substrate. However, radiation losses are very high, to the point that the other contributions become negligible compared to it.

The Quarter-Mode topology is a step forward in the miniaturization of SIW cavity resonators. In terms of performance, it offers an improvement over the half-mode structures only at lower frequencies and with substrates with high dielectric constant. Otherwise, the large amount of radiation losses makes this topology not ideal.

3.1.5 Eight-Mode cavity resonator

The concept of searching for possible symmetries in the resonant modes in order to reduce the size of the resonator can be used once more. From the Quarter-Mode resonant field distribution of figure 3.6b, a symmetry axis can be noticed along the diagonal of the whole structure. Once again, by removing part of the top metallization and the vias we obtain an even smaller topology, called Eighth-Mode since it represents one eighth of the original

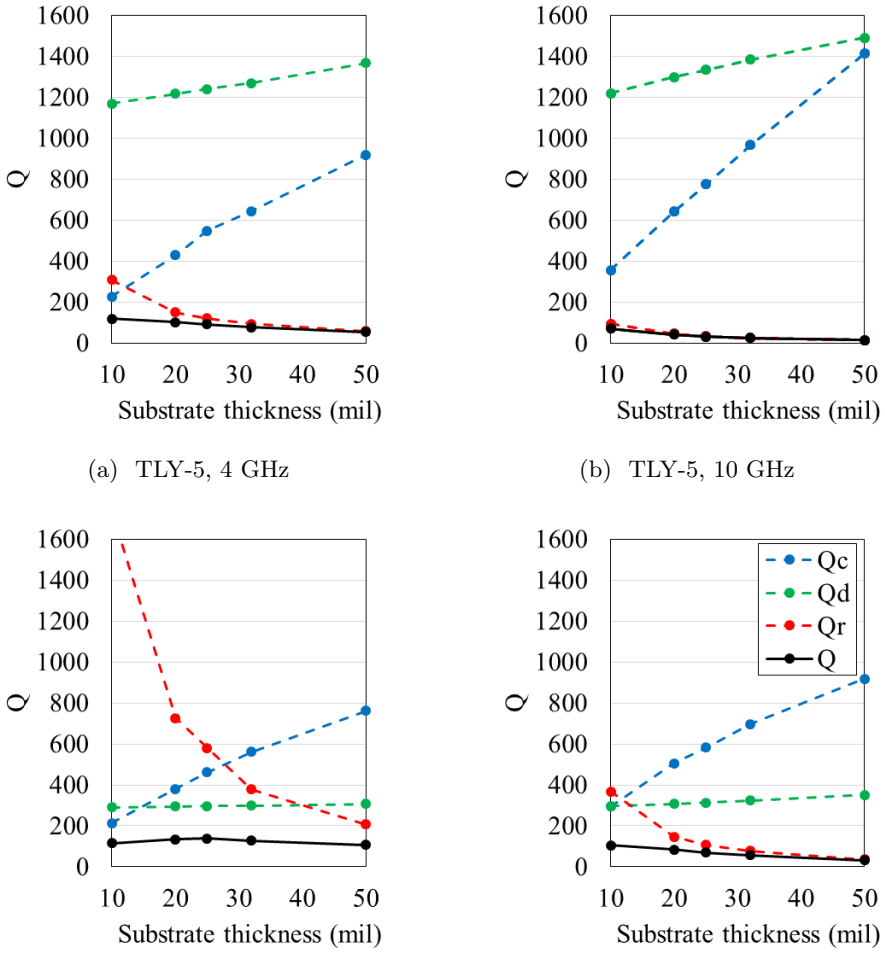

(a) TLY-5, 4 GHz

(b) TLY-5, 10 GHz

(c) CER-10, 4 GHz

(d) CER-10, 10 GHz

Figure 3.7: Effect of the substrate thickness on the loss contributions of the Quarter-Mode SIW resonator. Q_c: conductor quality factor. Q_d: dielectric quality factor. Q_r: radiation quality factor. Q: overall unloaded quality factor

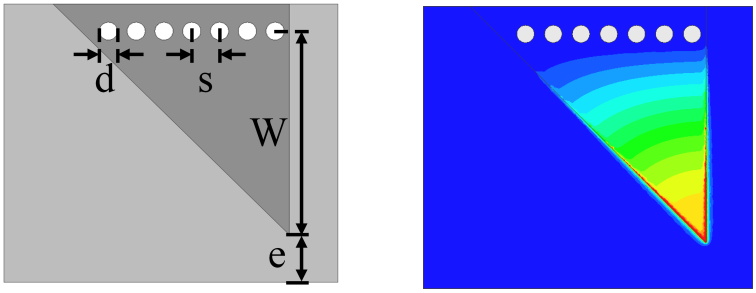

(a) (b)

Figure 3.8: Layout and resonant mode field distribution of the Eighth-Mode SIW resonator

SIW cavity structure. The structure is shown in figure 3.8.

As for the previous topologies, the cavity length w is the main parameter that controls the resonant frequency of the component. The smaller cavity dimension makes the conductor losses slightly higher and, in turn, lower the value of Q_c. The radiation losses of this topology are potentially lower than the Quarter-Mode; the reason comes from the shape of the open edges of the structure. The radiated power comes from the fringing fields of the resonant mode; the fields on the left, tilted side of the structure oscillate with the same phase as the ones on the right side. Due to their orientation, however, the fields on one side will partly cancel out the power coming from the other side. The dielectric losses still depend on the confinement of the resonant mode.

The physical dimensions of all the designed resonators are shown in table 3.7, while the computed quality factors are shown in table 3.8. A detailed view on the various quality factor contributions is presented in the plots of figure 3.9. The results show that the Eighth-Mode topology follows the same trends set by the other open structures: the resonators based on the high permittivity CER-10 substrate offer slightly higher quality factors than their Quarter-Mode counterparts thanks to the reduced amount of radiated power, while the performance of the TLY cavities still suffer from poor field confinement. At higher frequencies, the amount of radiation from the open sides of the topology increases, lowering the overall quality factor of the structures.

3.1.6 Shielded Quarter-Mode cavity resonator and variants

While all the open resonator structures offer a large improvement in the miniaturization compared to standard SIW cavities, their quality factors are relatively low, especially when the substrate thickness is higher. To obtain components that are smaller than the classic SIW cavity while preserving at

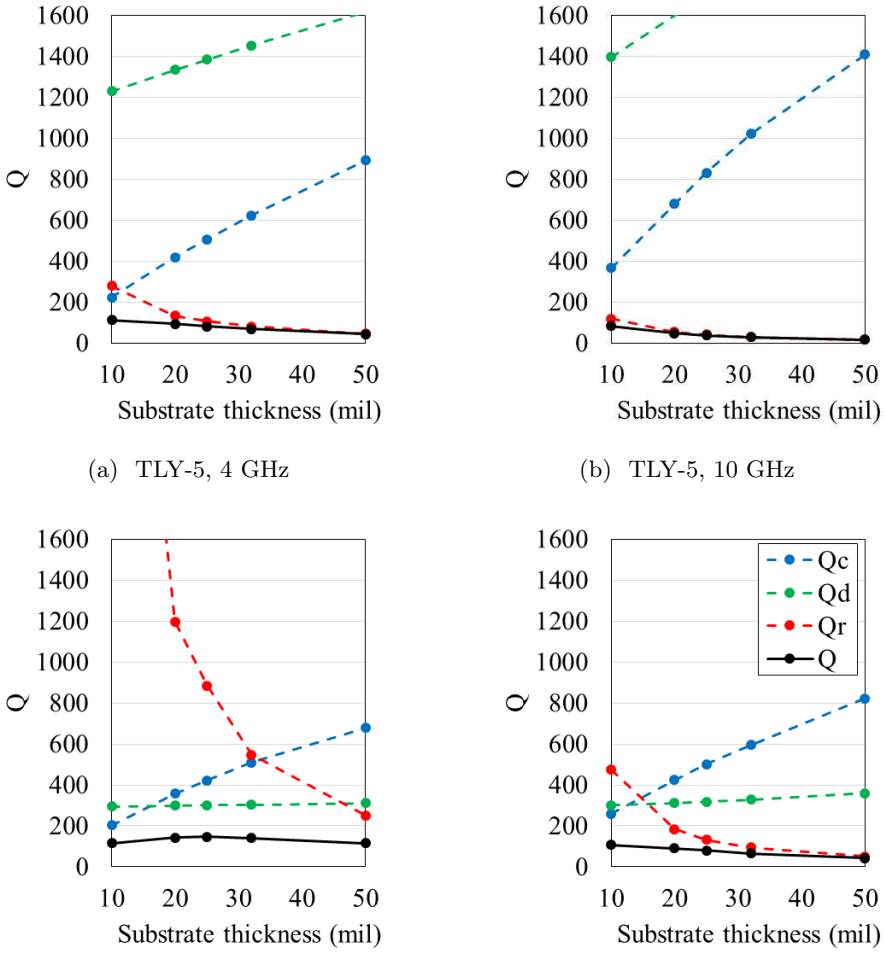

(a) TLY-5, 4 GHz

(b) TLY-5, 10 GHz

(c) CER-10, 4 GHz

(d) CER-10, 10 GHz

Figure 3.9: Effect of the substrate thickness on the loss contributions of the Eighth-Mode SIW resonator. Q_c: conductor quality factor. Q_d: dielectric quality factor. Q_r: radiation quality factor. Q: overall unloaded quality factor

Table 3.7: Design parameters of the Eighth-Mode SIW cavity resonators

	TLY-5 4 GHz	TLY-5 10 GHz	CER-10 4 GHz	CER-10 10 GHz
W	17.95 mm	7.48 mm	8.78 mm	3.51 mm
d	1.5 mm	1.5 mm	1.5 mm	1 mm
s	2.39 mm	2.14 mm	2.51 mm	1.4 mm
e	5 mm	4 mm	5 mm	2.5 mm

Table 3.8: Unloaded quality factors Q_u of the Eighth-Mode SIW cavity resonators

Substrate thickness	TLY-5 4 GHz	TLY-5 10 GHz	CER-10 4 GHz	CER-10 10 GHz
10 mil	112.9	83.7	116.4	107.6
20 mil	94.1	47.9	143.3	90.9
25 mil	81.9	38.2	146.4	78.9
32 mil	68.8	28.6	141.2	65.8
50 mil	42.9	16	115.4	42

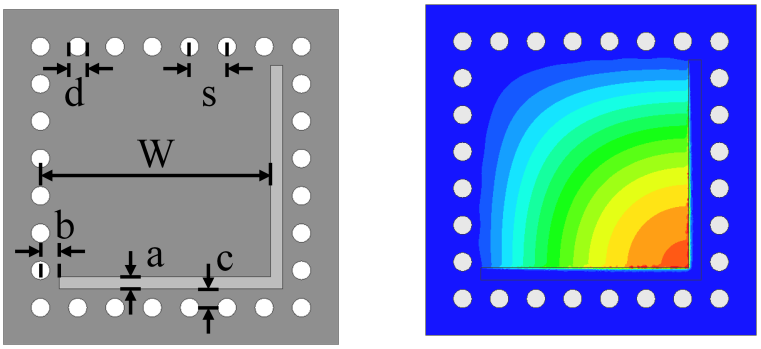

(a) (b)

Figure 3.10: Layout and resonant mode field distribution of the Shielded Quarter-Mode SIW resonator

Table 3.9: Design parameters of the Shielded Quarter-Mode SIW cavity resonators

	TLY-5 4 GHz	TLY-5 10 GHz	CER-10 4 GHz	CER-10 10 GHz
W	18.3 mm	7.7 mm	8.92 mm	3.8 mm
d	1.5 mm	1.5 mm	1.5 mm	1 mm
s	2.97 mm	2.55 mm	2.65 mm	1.67 mm
a	1 mm	1 mm	0.6 mm	0.5 mm
b	1.5 mm	1.5 mm	1 mm	0.7 mm
c	1.5 mm	1.5 mm	1 mm	0.7 mm

least part of their high quality factor, it is necessary to take steps to limit the radiation power loss. To keep the dimensions of the resonator small, it is necessary to use the magnetic wall boundary conditions given by the capacitive effects between the metal plates on the top and bottom faces of the substrate. However, this implies the creation of an open topology; it is impossible to cover the edges of the structure without using at least a multilayer planar technology, increasing the design complexity. Still, the only way to reduce the amount of power leaving the resonator is to modify the structure near the discontinuity.

A way to reduce the intensity of radiation is to place a partial shield in the form of rows of metallized posts near the open edge of the structures. When applied to the Quarter-Mode topology, the resulting structure is shown in figure 3.10. The partial electrical shielding strongly reduces the structure radiation loss, by making the propagation of surface wave in the substrate impossible. The rows of metallic posts, also help to lower the radiation efficiency of the fringing fields. In the end, even if the radiation cannot be completely eliminated, the radiation quality factor Q_r of the Shielded Quarter-Mode structures is higher than the other open topologies, especially with thicker substrates. As a side effect, the modal surface current density tends to be higher near the open edges, increasing the conductor losses compared to the other topologies; this leads to a lower conductor quality factor Q_c. Finally, the losses in the dielectric are the around the same as the other structures.

Alternative topologies for electromagnetic shielding

Usually, in order to obtain the compact resonator topologies, only the top metal layer of the substrate is removes, while the bottom layer is left untouched. In this case, the side view of the shielded resonator can be seen in figure 3.12a.

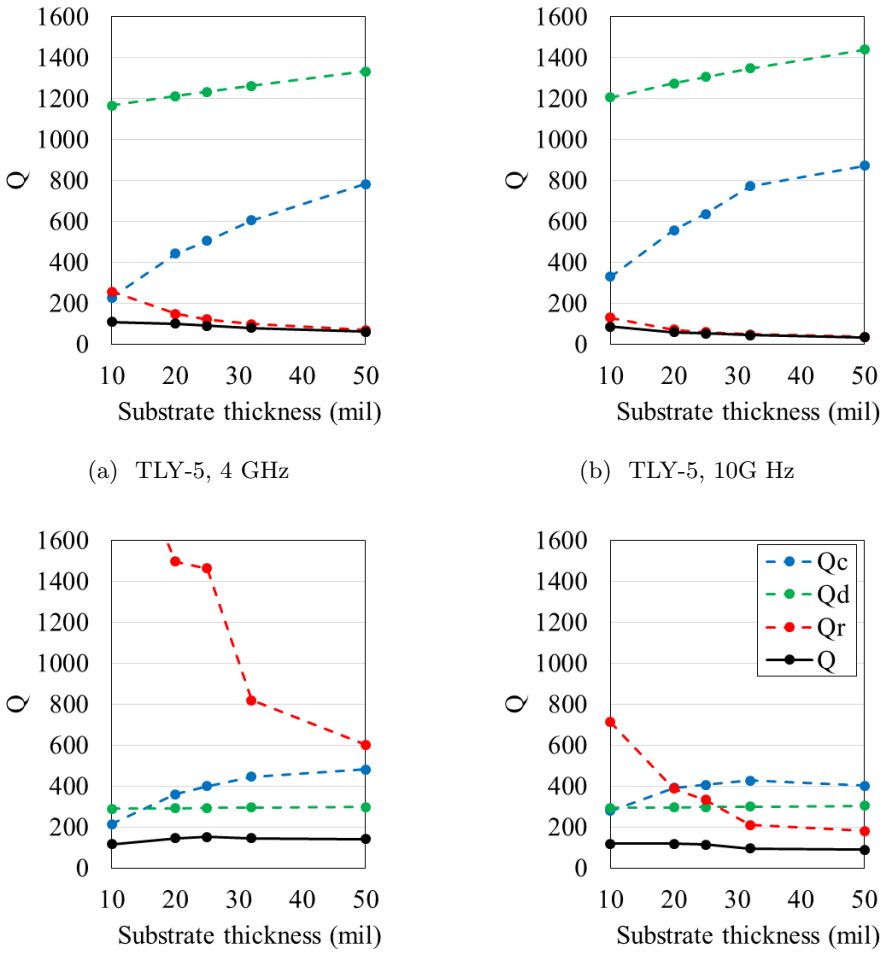

(a) TLY-5, 4 GHz

(b) TLY-5, 10G Hz

(c) CER-10, 4 GHz

(d) CER-10, 10 GHz

Figure 3.11: Effect of the substrate thickness on the loss contributions of the Shielded Quarter-Mode SIW resonator. Q_c: conductor quality factor. Q_d: dielectric quality factor. Q_r: radiation quality factor. Q: overall unloaded quality factor

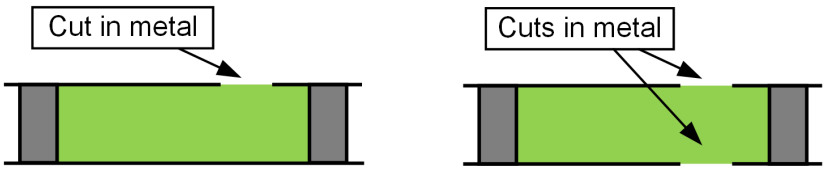

(a) (b)

Figure 3.12: Different approaches for the shielding of Quarter-Mode resonators

Table 3.10: Unloaded quality factors Q_u of the Shielded Quarter-Mode SIW cavity resonators

Substrate thickness	TLY-5 4 GHz	TLY-5 10 GHz	CER-10 4 GHz	CER-10 10 GHz
10 mil	109.7	86.2	116.9	118.8
20 mil	101.6	60	145.6	117.6
25 mil	91.4	52.2	151.8	113.4
32 mil	79.3	44.9	145.8	95.6
50 mil	60.5	34.3	141	88.4

Table 3.11: Unloaded quality factors Q_u of the modified dual-layer Shielded Quarter-Mode SIW cavity resonators

Substrate thickness	TLY-5 4 GHz	TLY-5 10 GHz	CER-10 4 GHz	CER-10 10 GHz
10 mil	135.7	124.3	118	126.7
20 mil	147.8	95	154.2	135.5
25 mil	135.1	84.7	161.1	133.6
32 mil	125.7	73.2	166	129.9
50 mil	97.7	53.2	160.5	118.4

By acting on both metal layers, it is possible to change the boundary conditions in the open edge of the structure. In this way, the effectiveness of the shielding may change. A possible strategy is to remove an area of the bottom metal layer with the same shape as the top layer. The side view of this dual-layer Shielded Quarter-Mode topology is shown in figure 3.12b. The top view is the same as the normal Shielded topology of figure 3.10. The results of the analysis of the dual-layer Shielded topology are shown in table 3.11, while the loss contribution details are presented in figure 3.13. It can be seen that, compared to the single-layer topology, all the structures show an increase in their quality factor. This is because of a further lowering in the amount of radiation, which increases the contribution of Q_r. This can be especially appreciated when the substrate is thicker.

Another approach is the partial removal of the substrate along the gap between the resonator and the electromagnetic shielding, as seen in figure 3.14. This can be achieved with production techniques that employ mechanical drilling and routing. In theory, the truncation of the substrate may result in a stronger confinement of the resonant fields inside the resonator. The results of the analysis of this topology are shown in table 3.12 and in figure 3.15. It can be seen that the shielding effect of this topology is actu-

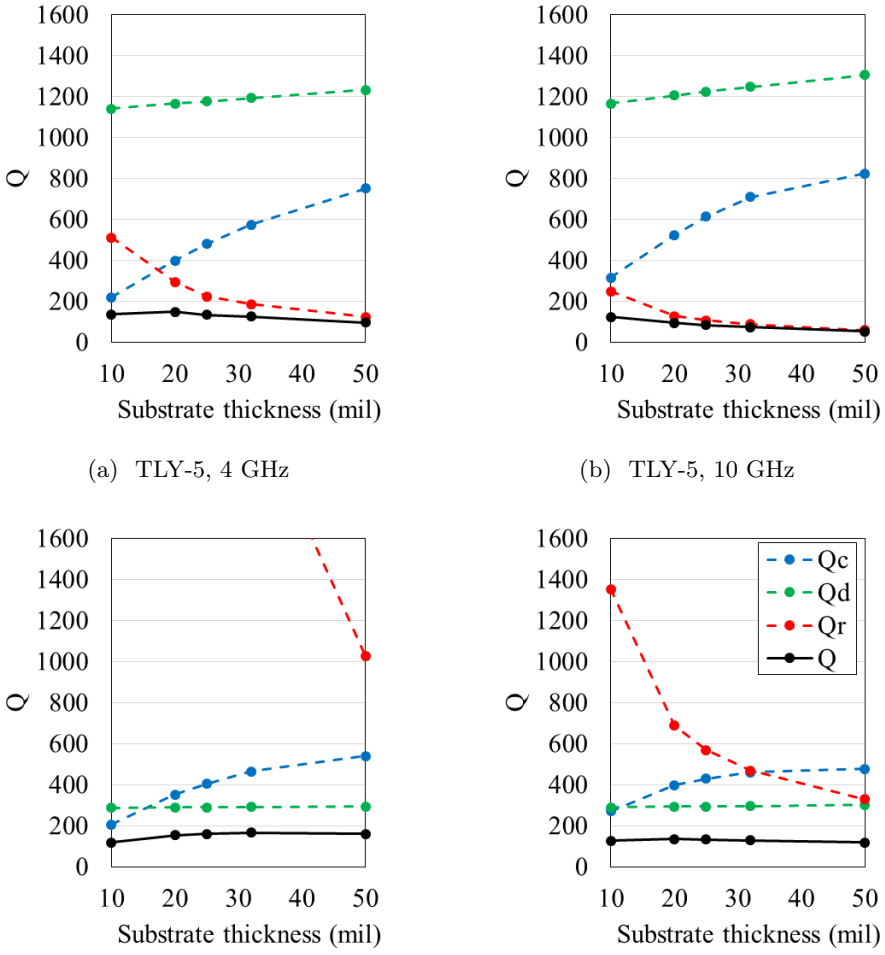

(a) TLY-5, 4 GHz

(b) TLY-5, 10 GHz

(c) CER-10, 4 GHz

(d) CER-10, 10 GHz

Figure 3.13: Effect of the substrate thickness on the loss contributions of the alternative dual-layer Shielded Quarter-Mode SIW resonator. Q_c: conductor quality factor. Q_d: dielectric quality factor. Q_r: radiation quality factor. Q: overall unloaded quality factor

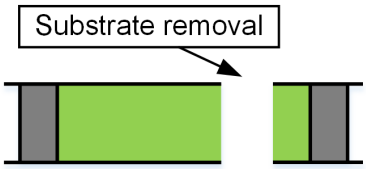

(a)

Figure 3.14: Side view of the Shielding topology with substrate removal

Table 3.12: Unloaded quality factors Q_u of the modified Shielded Quarter-Mode SIW cavity resonators, employing partial substrate removal

Substrate thickness	TLY-5 4 GHz	TLY-5 10 GHz	CER-10 4 GHz	CER-10 10 GHz
10 mil	136.4	124.1	116	125.2
20 mil	143	93.3	144.9	133.5
25 mil	135.9	81.6	149.7	129.9
32 mil	121.2	68.3	151.1	124.6
50 mil	91.8	49.4	147.5	114.3

ally lower than the dual-layer technique, since the fringing fields that appear inside the gap can more freely radiate in the surrounding space.

Design properties of the electromagnetic shield

When designing the shielded resonator, the size of the gap between the edge of the cavity and the shielding structure (parameter a from figure 3.10a) is particularly important. When decreasing the size of the gap, the amount of fringing field on the edge of the resonator becomes lower, and as a result Q_r increases. However, at the same time, the modal surface current density tends to be higher near the gap, increasing the conductor losses and lowering Q_c. For this reason, there is usually an optimum gap size that maximizes the overall quality factor of the structure. This dimension depends on how dominant the radiation losses are compared to the other contributions.

To show this effect, the dual-layer Shielded Quarter-Mode cavities that have been presented in the previous section have been modified by changing the size of the gap a between 0.2 and 1 mm. In particular, the results of the analysis of the 4 GHz structures operating at 4 GHz are presented in table 3.13 and figure 3.16. Structures where the radiation loss is particularly strong, such as the TLY-5 resonator, require very small gaps in order to obtain an increase of the quality factor. On the other hand, structures with a more balanced loss distribution like the CER-10 cavity have a smoother variation of the quality factor with the size of the gap.

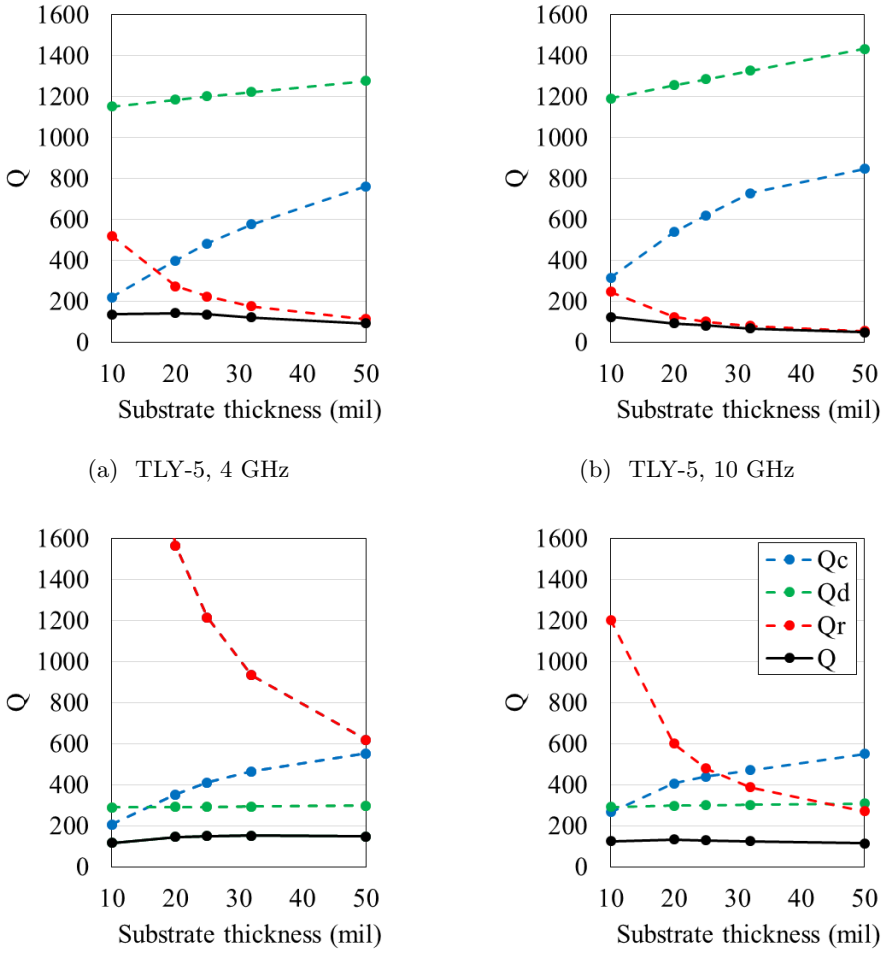

(a) TLY-5, 4 GHz

(b) TLY-5, 10 GHz

(c) CER-10, 4 GHz

(d) CER-10, 10 GHz

Figure 3.15: Effect of the substrate thickness on the loss contributions of the alternative Shielded Quarter-Mode SIW resonator with partial substrate removal. Q_c: conductor quality factor. Q_d: dielectric quality factor. Q_r: radiation quality factor. Q: overall unloaded quality factor

Table 3.13: Effect of gap width on the quality factor of Shielded Quarter-Mode SIW resonators. Operating frequency 4 GHz, substrate thickness 50 mil.

Gap width a	TLY-5 Q_u	CER-10 Q_u
0.2 mm	100.4	139.9
0.4 mm	101.9	156.7
0.6 mm	99.1	160.5
0.8 mm	98.2	161.3
1 mm	97.7	160

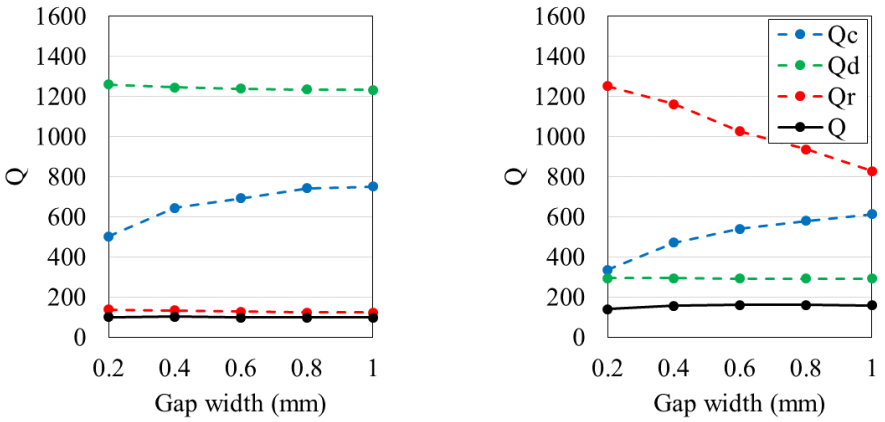

(a) TLY-5, 50 mil, 4 GHz

(b) CER-10, 50 mil, 4 GHz

Figure 3.16: Effect of the gap width a on the loss contributions of the alternative Shielded Quarter-Mode SIW resonator with cuts on both metal layers. Q_c: conductor quality factor. Q_d: dielectric quality factor. Q_r: radiation quality factor. Q: overall unloaded quality factor

3.1.7 Physical prototype measurements

To verify the data obtained by simulations that was presented in the previous chapter, a few prototypes of some of the resonators taken into exam have been designed, built and then measured. In particular, the resonators topologies that have been chosen to be built and measured as prototypes are the normal SIW cavity, the Quarter-Mode cavity, the Eighth-Mode cavity and the dual-layer Shielded Quarter-Mode cavity. For each topology, two versions have been designed: both operate at 4 GHz on CER-10 dielectric material, one with substrate thickness of 25 mil and another with thickness of 50 mil.

All the filters have been fabricated in the Microwave Laboratory of the University of Pavia. The components have been created by machining the substrates provided by Taconic using the CNC milling machine LPKF Protomat E33. This instrument allows for the selective removal of the metal layer and the drilling of the via holes. The vias have been metallized using the LPKF ProConduct silver-based conductive paste. In order to measure the resonators, each cavity is coupled to a short, 50 Ω microstrip line. This line is then connected to an Anritsu 37347C Vector Network Analyser through the Anritsu 3680-20 test fixture.

The quality factor of the prototypes have been measured using the reflection method [2]. The value of Q is extracted by looking at the frequency behaviour of the resonator (in particular, at the frequency bandwidth of the resonance). The effects of the coupling of the structure can be estimated and compensated by measuring the phase and the amount of reflection at resonance.

The results of the measurements are presented in table 3.14. The measurements fall in line with the quality factors computed and shown previously. The resonance of every prototype is shifted higher in frequency of a few hundred MHz. The reason behind this is that the actual value of the dielectric constant of the substrate differs from the nominal one.

Due to their fabrication techniques, each dielectric slab presents a slightly different dielectric constant, especially in the case of materials with high permittivity like CER-10. The increase in the resonant frequency indicates a lower dielectric constant. Another reason for the shift can be the presence of fabrication errors, since both the size of the structure and the coupling mechanism affect the resonant frequency. Measurements are compatible with the permittivity values of $\epsilon_r = 9.65$ for the substrate with thickness 25 mil, and $\epsilon_r = 9.6$ for the one with thickness 50 mil. These are around 4% away from the nominal value of the relative permittivity of the CER-10 material ($\epsilon_r = 10$), and are within the typical tolerance limits.

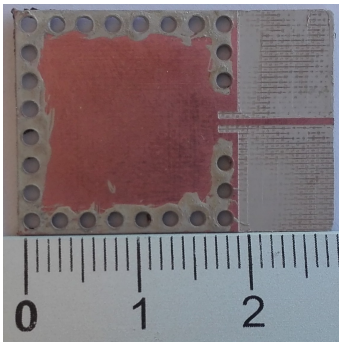

(a) SIW, 25 mil

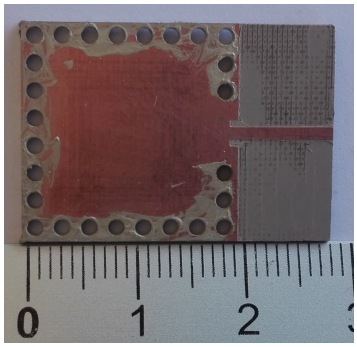

(b) SIW, 50 mil

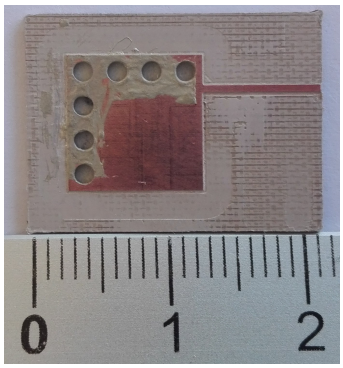

(c) Quarter-Mode SIW, 25 mil

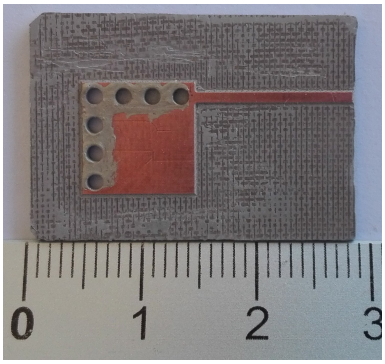

(d) Quarter-Mode SIW, 50 mil

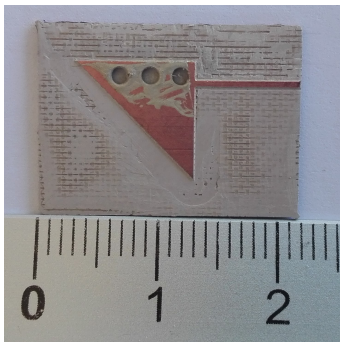

(e) Eighth-Mode SIW, 25 mil

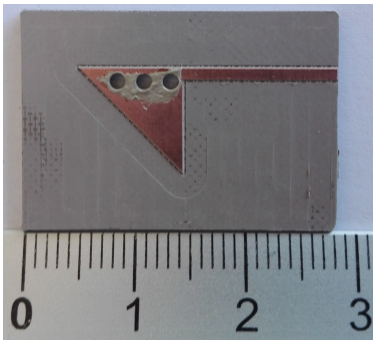

(f) Eighth-Mode SIW, 50 mil

Figure 3.17: Photo of the resonator prototypes

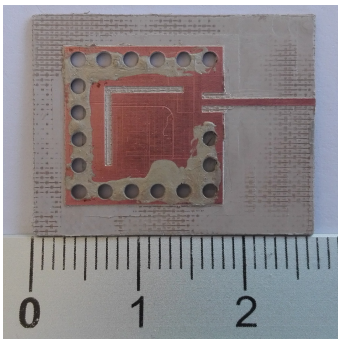

(g) Shielded Quarter-Mode SIW, 25 mil, top

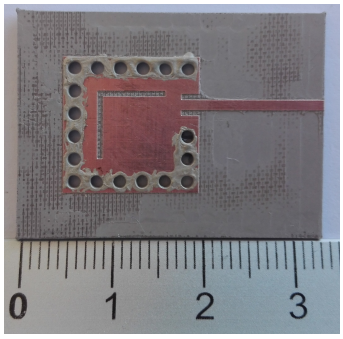

(h) Shielded Quarter-Mode SIW, 50 mil, top

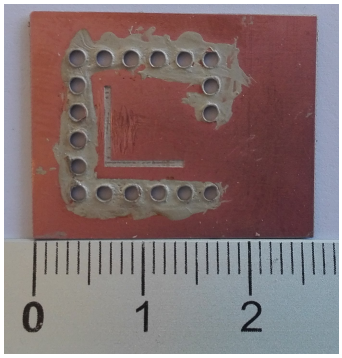

(i) Shielded Quarter-Mode SIW, 25 mil, bottom

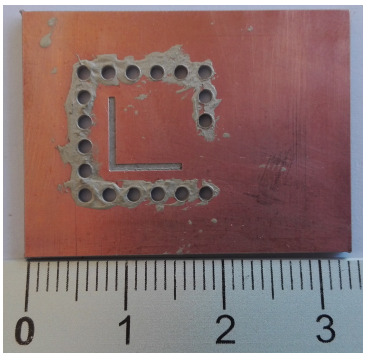

(j) Shielded Quarter-Mode SIW, 50 mil, bottom

Figure 3.17: Photo of the resonator prototypes

Table 3.14: Results of the measurements of the various SIW cavity resonators

Topology	Substrate thickness (h)	Measured unloaded quality factor Q_u	Measured frequency f
Traditional SIW	25 mil	155.3	4.068 GHz
	50 mil	166.7	4.08 GHz
Quarter-Mode SIW	25 mil	94.3	4.116 GHz
	50 mil	71.6	4.274 GHz
Shielded Quarter-Mode SIW	25 mil	103.5	4.044 GHz
	50 mil	124	4.166 GHz
Eighth-Mode SIW	25 mil	98.5	4.3 GHz
	50 mil	92.6	4.404 GHz

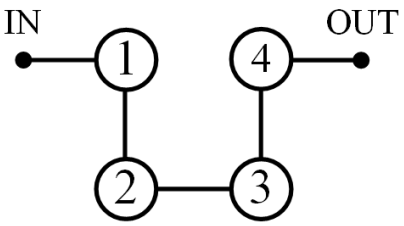

Figure 3.18: Topology of the 4-element folded inline Quarter-Mode filter

Table 3.15: Design parameters of the four-cavity Quarter-Mode filters with the inline folded topology

	Classical Q-M SIW	Shielded Q-M SIW
W	8.9 mm	8.7 mm
L	12 mm	11.8 mm
W_s	1.2 mm	1.2 mm
p_s	3.2 mm	3 mm
a	4.2 mm	4.2 mm
b	4.3 mm	4.2 mm
c	2.9 mm	3 mm
d	0.8 mm	0.8 mm
e	-	0.4 mm
f	-	1.2 mm

3.2 Sample Shielded Quarter-Mode filters

The best way to show the properties and qualities of a microwave technology is to analyse an application example. In the case of resonators, the design of a filter is particularly convenient to study the difference between different topologies.

The filter presented in [3] has been chosen to make a comparison between the normal Quarter-Mode resonator topology and the proposed Shielded version. The topology of the filter is shown in 3.18. It consists of four Quarter-Mode cavities, which are placed in a folded inline configuration, with the open side pointing outwards. This configuration is a good showcase for the miniaturization capabilities of the Quarter-Mode topology, since it allows for the implementation of a four-pole filter over the footprint of a single classical SIW resonator. The cavities are coupled by the proximity of their open sides, and the amount of coupling can be controlled by acting on the row of vias that separates the cavities.

This topology has been used to design two different versions of the filter:

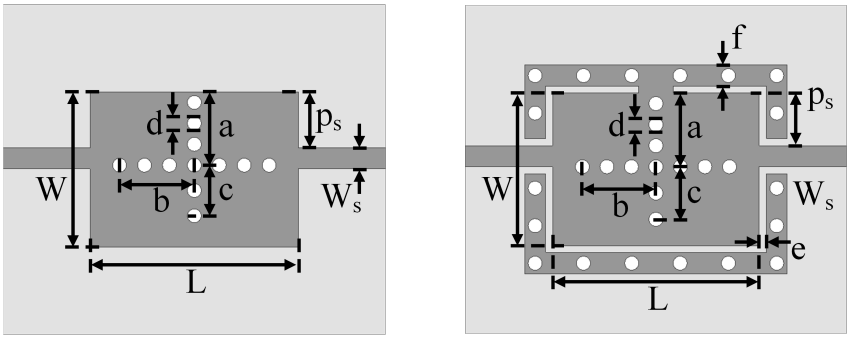

(a) Quarter-Mode (b) Shielded Quarter-Mode

Figure 3.19: Physical dimensions of the 4-element folded inline Quarter-Mode filter

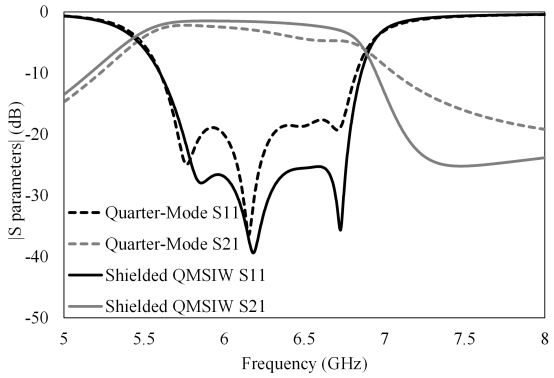

Figure 3.20: Frequency response of the 4-element folded inline Quarter-Mode filter

one based on the normal Quarter-Mode resonator technology, and another using dual-layer Shielded Quarter-Mode cavities. All the structures have been designed to operate around 6 GHz with a 20% fractional bandwidth, using a CER-10 substrate with thickness of 50 mil. The images of figure 3.19 show the physical parameters of the two filters. The value of these parameters is presented in table 3.15.

The frequency response of the devices can be seen in figure 3.20. The comparison between the two topologies shows that the shielded topology has a significant advantage over the normal Quarter-Mode. The insertion loss of the two filters are respectively -2.2 dB for the normal Quarter-Mode filter and -1.5 dB for the Shielded version the maximum difference in the S21 parameters is 2.3 dB at around 6.55 GHz. The area of the Shielded component is ∼22% higher than the other.

From the frequency response, it can be seen that the losses of the filters

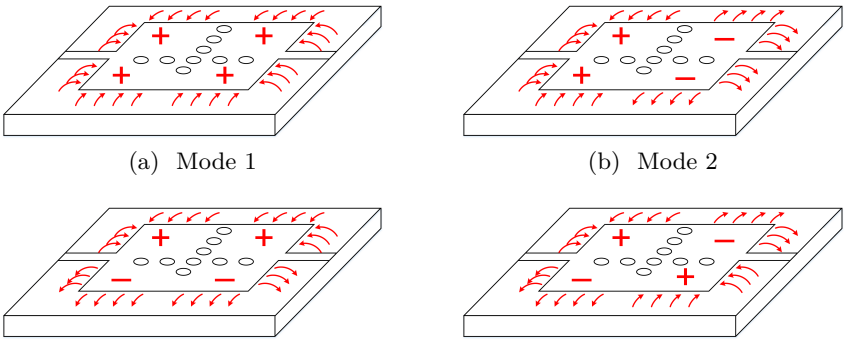

(a) Mode 1 (b) Mode 2

(c) Mode 3 (d) Mode 4

Figure 3.21: Layout of the resonant modes of the Quarter-Mode filter

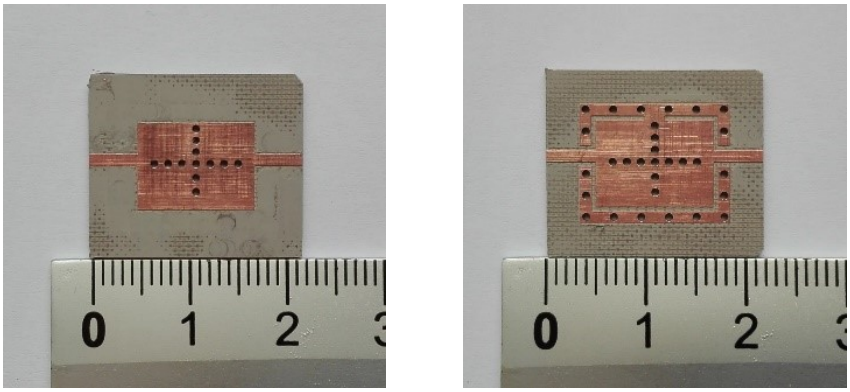

(a) Quarter-Mode (b) Shielded Quarter-Mode

Figure 3.22: Physical dimensions of the 4-element folded inline Quarter-Mode filter

are not constant along the entire operation bandwidth, especially in the case of the non-shielded filter. This can be explained by examining the resonant fields of the structure. Being a 4-cavity filter, the device will present four different resonant modes in the band of operation. These modes will generate some fringing fields on the edge of the structure. The polarity of these fringing field is different from each mode. 3.21 shows a schematic view of the various modes. For the purpose of radiation, the fringing fields of some of these modes (1 and 4) will cancel each other, reducing the losses coming from this mechanism. In the other cases (mode 2 and 3), however, the fringing fields will oscillate in phase, enhancing the radiation and producing the spike in losses that can be seen at around 6.5 GHz. Since in this case the main loss contribution is radiation leakage, the Shielded topology is particularly effective in increasing the performance of the filter.

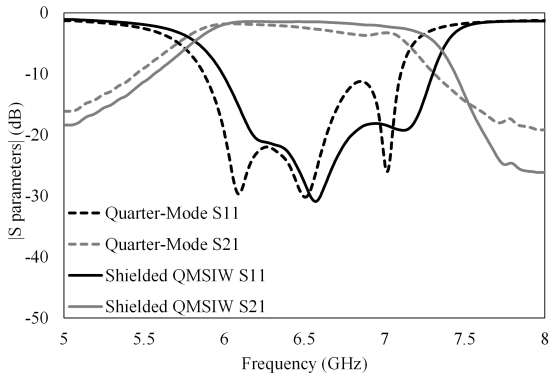

Figure 3.23: Measurements of the prototypes of the 4 element folded inline Quarter-Mode filter

For both filters, a prototype has been fabricated and measured using the same technique as the compact resonator prototypes shown in the previous section. An image of the two filters is shown in 3.22 The results of the measurements is presented in the graph of figure 3.23 As with the resonators, the filters present a shift towards higher frequencies compatible with a dielectric permittivity of the substrate of $\epsilon_r = 9.6$. The shift between the two versions of the filter can be explained in a slight overmilling of the Shielded Quarter-Mode component, which is more sensitive to fabrication errors. Regardless, the comparison confirms the difference in performance between the two topologies.

The study of resonator losses and the design of sample filters resulted in the following publications: [4, 5, 6, 7, 8, 9].

References

[1] D. M. Pozar, *Microwave Engineering.* Wiley, 2004.

[2] R. J. Cameron, R. Mansour, and C. M. Kudsia, *Microwave Filters for Communication Systems: Fundamentals, Design and Applications.* Wiley, 2007.

[3] Zhenyu Zhang, Ning Yang, and Ke Wu, "5-GHz bandpass filter demonstration using quarter-mode substrate integrated waveguide cavity for wireless systems," in *2009 IEEE Radio and Wireless Symposium*, pp. 95–98, 2009.

[4] N. Delmonte, M. Bozzi, L. Perregrini, and C. Tomassoni, "Cavity resonator filters in shielded quarter-mode substrate integrated waveguide technology," in *2018 IEEE MTT-S International Microwave Workshop Series on Advanced Materials and Processes for RF and THz Applications (IMWS-AMP)*, pp. 1–3, 2018.

[5] N. Delmonte, M. Bozzi, L. Perregrini, and C. Tomassoni, "Miniaturization and quality-factor in substrate integrated waveguide cavities," in *2018 IEEE MTT-S International Conference on Numerical Electromagnetic and Multiphysics Modeling and Optimization (NEMO)*, pp. 1–4, 2018.

[6] N. Delmonte, C. Tomassoni, M. Bozzi, and L. Perregrini, "Compact resonators in substrate integrated waveguide technology," in *2018 IEEE MTT-S International Wireless Symposium (IWS)*, pp. 1–3, 2018.

[7] N. Delmonte, M. Bozzi, L. Perregrini, and C. Tomassoni, "Miniaturized SIW filters based on shielded quarter-mode cavities," in *2019 IEEE MTT-S International Conference on Numerical Electromagnetic and Multiphysics Modeling and Optimization (NEMO)*, pp. 1–3, 2019.

[8] N. Delmonte, C. Tomassoni, M. Bozzi, and L. Perregrini, "Performance study of compact substrate integrated waveguide resonators," in *XXII Riunione Nazionale di Elettromagnetismo (XXII RiNEm)*, pp. 1–3, 2018.

[9] N. Delmonte, C. Tomassoni, L. Perregrini, and M. Bozzi, "Modified quarter-mode substrate integrated waveguides cavities: Performance study and application to filters," *International Journal of RF and Microwave Computer-Aided Engineering*, vol. 31, no. 3, p. e22524, 2021.

Chapter 4

Advanced topologies for SIW filters

One of the main strengths of the Substrate Integrated Waveguide technology is its great flexibility. When it is applied to the design of microwave filters, it can be combined with a great deal of different techniques and technologies in order to obtain a variety of filtering responses. This chapter will present a few different filter models where the properties of the SIW technology and its compact versions have been exploited to achieve some particular effects.

4.1 Prefiltering for the improvement of out-of-band performance

As it was discussed in the previous chapters, the main advantage of the Substrate Integrated Waveguide over other planar transmission line technologies are the very low losses and high electromagnetic performance. This makes the SIW technology ideal for the development of narrow-band, highly selective microwave filters.

As with any other kind of resonator, SIW cavities have an unlimited amount of resonant modes. Usually, when a resonator is used as the base for the creation of a filter, only the fundamental or the first few modes are considered in the design. The remaining resonances are considered as spurious, and their effect is the formation of upper band-pass frequencies. There are particular types of resonators with a more sparse modal spectrum: these structures can be used to obtain filters with wider rejection bandwidths. However, these structures usually have poorer performance compared to the classic SIW cavities. Some examples of resonators with wider spurious-free regions are the compact SIW structures presented in the previous chapters.

One way to increase the out-of-band performance of SIW components is employing the dual filter topology shown in figure 4.1 [1]. The device is divided in two stages: a prefilter which is composed of compact resonators

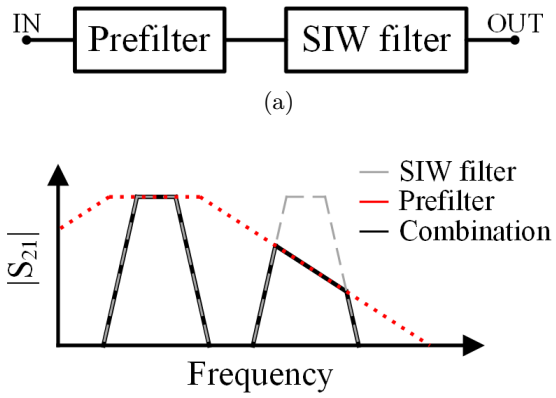

Figure 4.1: Scheme of the prefilter technique

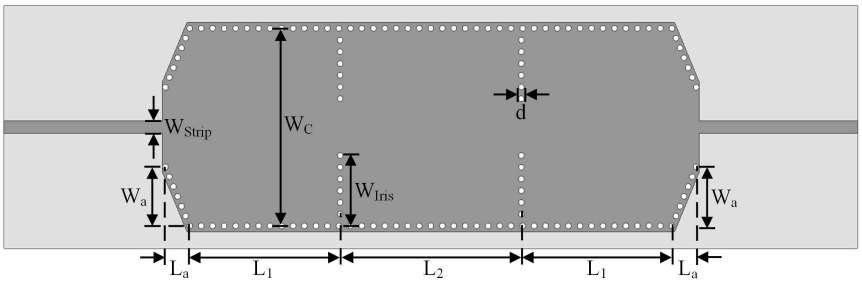

Figure 4.2: Layout of the SIW filter without a prefilter stage

with wide spurious-free bandwidth, and a SIW filter which provides the high selectivity. Normally, the prefilter would degrade the performance of the rest of the device. However, the insertion loss of a filter depends both on the quality factor and the amount of coupling of the resonators. Devices with strongly coupled cavities are not very affected by the resonator Q. The prefilter can then be created using the more lossy compact resonators without impacting the performance of the overall device. High amounts of coupling means that the prefilter will have a broadband response; this is not a problem for the design of narrowband filters, since the SIW stage will provide the selectivity. The only restriction on the band of the prefilter is to be small enough to block the first spurious resonance of the SIW stage.

In order to study the effectiveness of this technique, two filters have been designed. The first is a simple 3-cavity inline SIW filter. The second is the same structure with the addition of a 2-cavity prefilter based on quarter-wave microstrip stub resonators. This topology has been chosen since it allows for the creation of particularly compact structures.

The layout of the simple SIW resonator is shown in figure 4.2. The

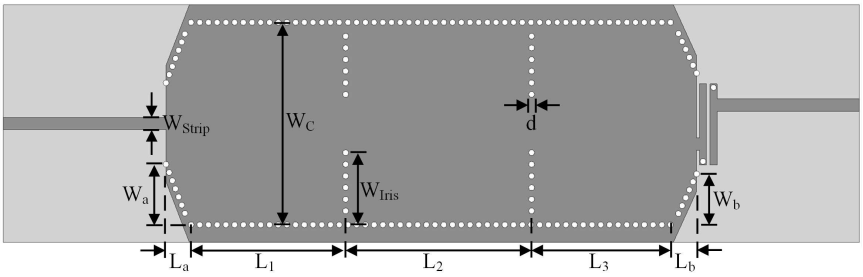

(a) SIW filter

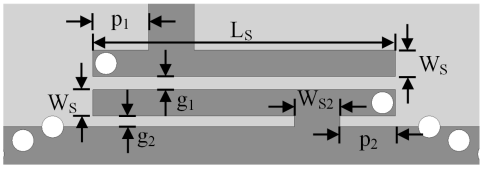

(b) Prefilter

Figure 4.3: Layout of the SIW filter with a prefilter stage

structure has been designed to have a 2.9% fractional bandwidth centred at 4 GHz. The design parameters are shown in table 4.1. The dielectric used is a Taconic TLX-9 substrate (permittivity $\epsilon_r = 2.55$, loss tangent $\tan\delta = 0.0022$) with thickness 0.76 mm (30 mil). The frequency behaviour of this component is shown in figure 4.4. The device has an insertion loss of -2.1 dB, and the first spurious frequency can be seen at around 6 GHz.

The second structure is the same layout, modified to have the microstrip stub prefilter before the SIW resonators. The layout is presented in 4.3. The physical dimensions had to be slightly retuned, and are shown in 4.1. In this case, a physical prototype has also been created and measured, using the same techniques of the components shown in the previous sections. The results of the measurements of the prototype are shown in 4.6. The new filter has a modest increase in the insertion loss, reaching -2.5 dB. However, it can be seen that the out-of-band response has been greatly enhanced. The S_{21} parameter of the device stays below -20 dB up to 11.5 GHz, almost three times the pass-band frequency. Even after that, the transmitted power always stays below -10 dB in the whole measurement band. This is achieved with a negligible increase in the dimensions of the component. The results of this work have been published in [2].

	No prefilter	With prefilter
W_{strip}	2.1 mm	2.1 mm
W_{iris}	12.375 mm	12.375 mm
W_a	10.375 mm	8.275 mm
W_b	-	10.375 mm
W_c	34.75 mm	34.75 mm
W_s	-	1.2 mm
W_{s2}	-	2.1 mm
L_1	26.6 mm	23.9 mm
L_2	32 mm	32 mm
L_3	-	26.6 mm
L_a	4.3 mm	4.5 mm
L_b	-	4.3 mm
L_s	-	13.9 mm
p_1	-	2.55 mm
p_2	-	2.55 mm
g_1	-	0.6 mm
g_2	-	0.5 mm
d	1 mm	1 mm

Table 4.1: Design parameters of the SIW filters with the prefilter

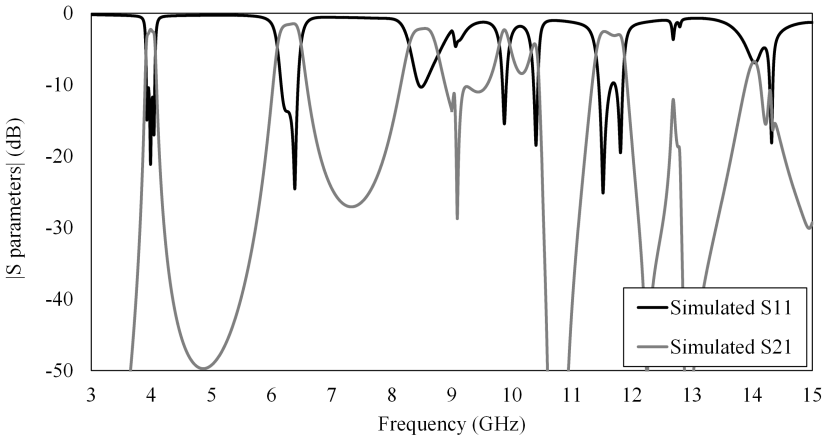

Figure 4.4: Frequency response of the SIW filter without a prefilter stage

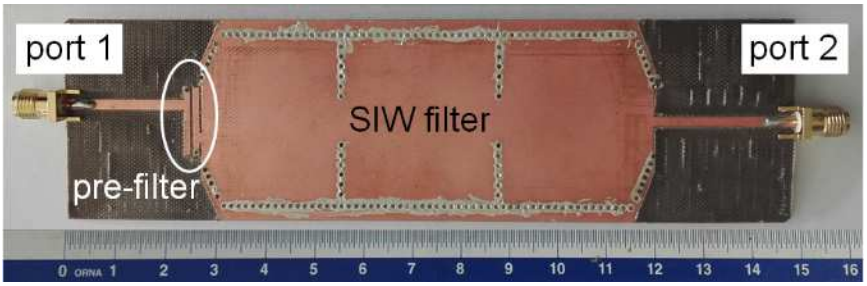

Figure 4.5: Picture of the prototype of the SIW filter with a prefilter stage

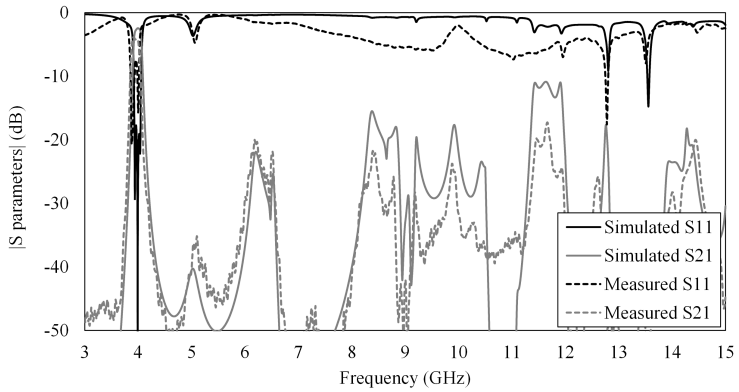

Figure 4.6: Frequency response of the SIW filter with a prefilter stage

4.2 SIW filter with frequency dependent couplings

A common technique that can be used to increase the selectivity of a microwave filter consists in placing transmission zeroes around the pass-band. The number of finite frequency transmission zeroes of a filter depend on its topology [3]. Most of the configurations that allow the control of the transmission zeroes involve the use of folded topologies and cross-coupling between multiple resonators.

Transmission zeroes can also be obtained in simpler topologies such as inline filters with the use of frequency dependent couplings [4]. Depending on the technology used to fabricate the filter, there different ways to obtain this kind of dispersive behaviour. Similar to rectangular waveguide, the frequency dependent couplings in SIW structures are obtained using lateral stubs [5], as shown in figure 4.7a. The input and output of the stub is connected to transmission lines or resonators with width a_0. The stub can transport electromagnetic energy between the ports through two different physical mechanisms. In the first one, the stub acts like a resonator, and the energy passes trough the TE_{201} resonant mode (dashed red lines of the figure). In the second one, the stub behaves as a simple transmission line of

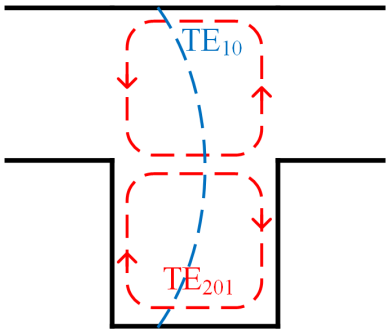

(a) Layout and electric field modes

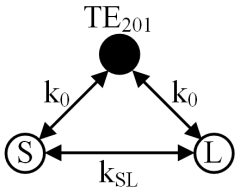

(b) Routing scheme

Figure 4.7: Parallel SIW stub

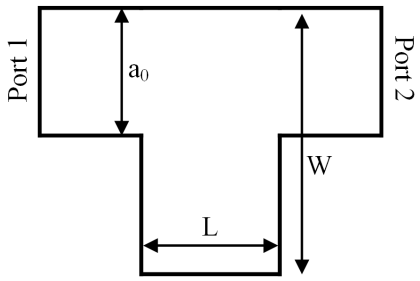

Figure 4.8: Layout of the SIW singlet

width a, and the energy travels using the TE_{10} propagating mode (dashed blue lines of the figure). The dispersive coupling behaviour of the stub comes form the interaction of these two mechanisms. The routing scheme of the stub can be seen in figure 4.7b.

An equivalent circuital model of the stub can be used in order to better represent the behaviour of the parallel stub in the design stage of a microwave filter. The shape and value of the equivalent circuit can be retrieved by analysing the frequency response of a stub connected to a pair of simple transmission lines, as shown in 4.7a. This layout is called the *singlet*. The behaviour of the singlet can be approximated in the most general way using a single shunt reactance X, as shown in the circuit of 4.9a. Due to the dispersive nature of the stub, the value of this reactance will change

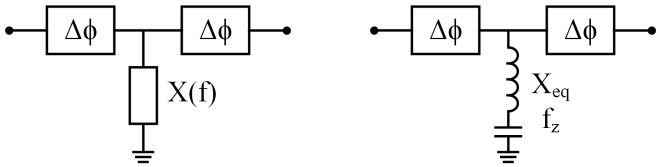

(a) Generic singlet (b) Stopband singlet

Figure 4.9: Equivalent circuit for the SIW singlet

depending on the frequency. The pair of phase shifters $\Delta\phi$ represent the effect of the singlet on the phase of the signal, and cover the propagation inside input transmission lines. The simple layout of the singlet can easily be implemented in a full-wave electromagnetic simulator. The scattering parameters can then be used to retrieve the values of the circuital parameters, using the following equations presented in [6]:

$$X(f) = -\mathrm{Im}\left\{\frac{1}{2}\frac{S_{12}(f)}{S_{11}(f)}\right\} \tag{4.1}$$

$$\Delta\Phi(f) = -\frac{\angle\left\{S_{12}(f) - S_{11}(f)\right\}}{2} \tag{4.2}$$

The effect of the transmission line on $\Delta\phi$ can be removed using deembedding. The values of the couplings seen in 4.7b depend on the physical dimensions of the singlet. For this reason, the reactance parameter X will change depending on the length L and width a of the stub.

In most cases, the singlet shows a frequency response containing one transmission zero and one reflection zero along the single mode bandwidth of the transmission lines. The relative position of these two zeroes mainly depend on the magnitude of the direct input/output coupling k_{SL}. As this value increases, the frequency of the reflection zero is pushed towards infinity, resulting in a response with only a transmission zero. In this case, the structure is called a *stopband singlet* [7]. The equivalent circuit of this structure is represented by a series LC resonator placed in shunt in respect to the transmission line, as shown in 4.9b. The parameters of the series resonator can be defined using the resonant frequency f_z and the reactance slope X_{eq}, and they can once again be retrieved through a full-wave simulation. The resonant frequency corresponds to the position of the transmission zero of the singlet, while the slope parameter is given by:

$$X_{eq} = -\frac{1}{2} f_z \left.\frac{dX(f)}{df}\right|_{f=f_z} \tag{4.3}$$

A 4-element SIW inline filter has been designed as a practical application example of the stopband singlet. The layout of the filter is shown in 4.10. There are two parallel stubs: in this way, two transmission zeroes can be

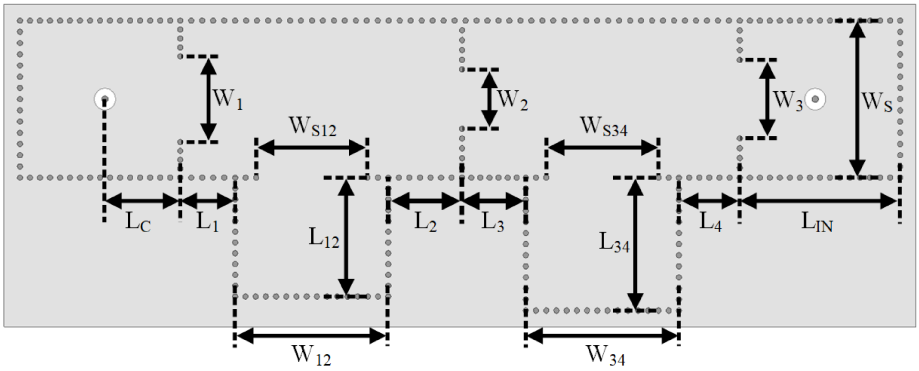

Figure 4.10: Layout of the 4-element SIW filter with frequency dependent couplings

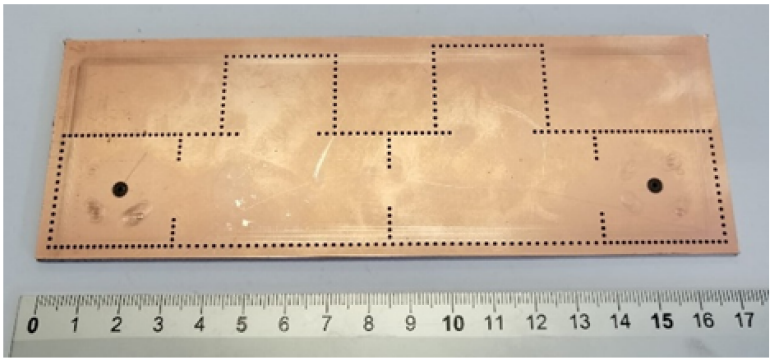

Figure 4.11: Prototype of the 4-element SIW filter with frequency dependent couplings

Physical dimensions	
W_S	29 mm
W_1	15.8 mm
W_2	10.94 mm
W_3	14.5 mm
W_{12}	29 mm
W_{34}	29 mm
W_{S12}	20.96 mm
W_{S34}	21.8 mm
L_{IN}	30.37 mm
L_C	14.27 mm
L_1	10.4 mm
L_2	13.99 mm
L_3	12.07 mm
L_4	11.77 mm
L_{12}	21.94 mm
L_{34}	24.53 mm

Table 4.2: Design parameters of the 4-element SIW filter with frequency dependent couplings

placed around the pass-band of the filter. The other two couplings are obtained using traditional inductive irises. The filter is designed to have a bandwidth of 160 MHz around a central frequency of 5 GHz. The design parameters are shown in table 4.2. The substrate used is a Taconic TLY-5 laminate (dielectric permittivity $\epsilon_r = 2.2$, loss tangent $\tan\delta = 0.0009$) with thickness 1.52 mm (50 mil). A prototype has been fabricated and measured in the University of Pavia. For the production, an LPKF E33 milling machine has been used. The measurement has been made on an Anritsu 37347C VNA. A picture of the device is shown in 4.11. The two areas where the metal has been removed are the place where two standard SMA coaxial probes have been placed in order to measure the device.

The frequency behaviour of the filter is shown in 4.12. Compared to the desired response there is a small shift towards higher frequencies. This is explained by the value of the dielectric permittivity of the slab of substrate used for the prototype, which was computed to be $\epsilon_r = 2.18$ (within the tolerance of the material). The insertion loss of the measured prototype is -1.2 dB. The design procedure for the parallel stubs and the filter can also be found in [8].

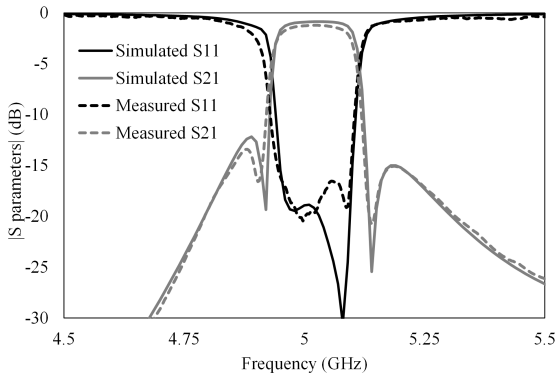

Figure 4.12: Frequency response of the 4-element SIW filter with frequency dependent couplings

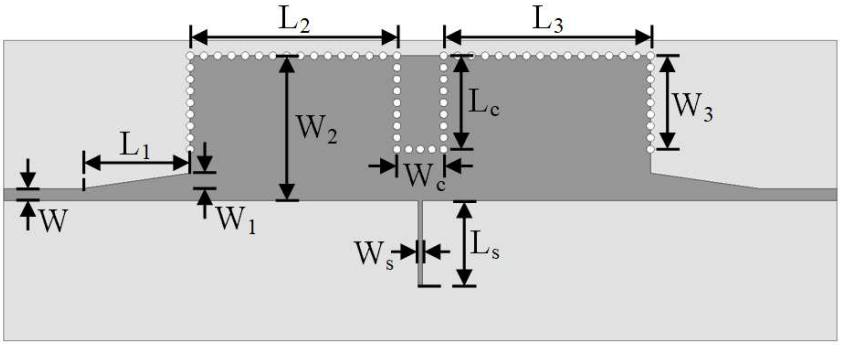

Figure 4.13: Layout of the Half-Mode filter

4.3 Half-Mode SIW filter with frequency dependent couplings

The use of frequency dependent couplings is a general concept, which can be applied to all sorts of filters based on any technology. For this reason, the filter presented in the previous section could be implemented using Half-Mode resonators in order to reduce its footprint. However, the peculiarities of the Half-Mode SIW technology allow to further increase the miniaturization level.

The electromagnetic fields that form around the open side of an Half-Mode SIW structure can be used to gain access to the electromagnetic signal and couple a nearby resonator. In particular, microstrip stubs can be placed directly on the edge of the structure. The stub resonators can be exploited to obtain the frequency dependent couplings required for the synthesis of transmission zeroes.

An bandpass filter based on this hybrid Half-Mode/microstrip technol-

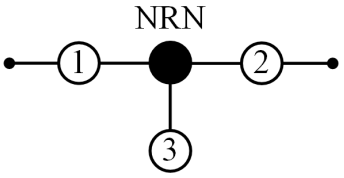

Figure 4.14: Topology of the Half-Mode filter

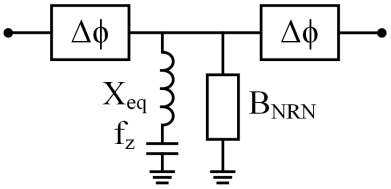

Figure 4.15: Equivalent circuit of the dispersive coupling section

ogy is shown in figure 4.13. It is composed of two Half-Mode SIW cavities and one quarter-wavelength microstrip stub. The behaviour of this filter can be well explained with the use of *non-resonating nodes* (NRNs).

A NRN is a section of the filtering structure which delivers electromagnetic energy without showing resonant behaviour. For example, it can be a short length of transmission line, or a cavity operating far below its fundamental resonant frequency. NRNs offer a great amount of flexibility to the design of a filter, allowing for the realization of frequency dependent couplings and the synthesis of additional transmission zeroes, with a low impact on the complexity of the filter [9, 10].

The routing scheme of the filter is shown in figure 4.14. The Half-Mode cavities represent resonators 1 and 2, while resonator 3 is the open-circuited microstrip stub. The non-resonating node corresponds to the large coupling iris placed between the Half-Mode cavities, which behaves like a small length of SIW transmission line below cut-off. Overall, the combination of the NRN and the side microstrip stub behaves in a very similar way to the side SIW stub presented in the previous section, and can be modelled using the equivalent circuit shown in 4.15. The series LC circuit describes the dispersive nature of the section and returns the appropriate transmission zero, while the fixed susceptance B_{NRN} allows for the additional reflection zero to appear in band.

The device has been designed to work at 4.5 GHz, with a fractional bandwidth of 8%. The dimensions of the synthesised filter are shown in table 4.3. The frequency response of the filter shows three transmission poles and one transmission zero. It is important to notice that the frequency of the transmission zero only depends by the resonance of the microstrip stub, so it can be controlled by acting on L_s. The substrate used for the

Physical dimensions	
W	1.55 mm
W_1	2 mm
W_2	18.6 mm
W_3	12.7 mm
L_1	14 mm
L_2	26.5 mm
L_3	26.5 mm
W_c	6 mm
L_c	13 mm
W_s	0.44 mm
L_s	11 mm

Table 4.3: Design parameters of the Half-Mode filter

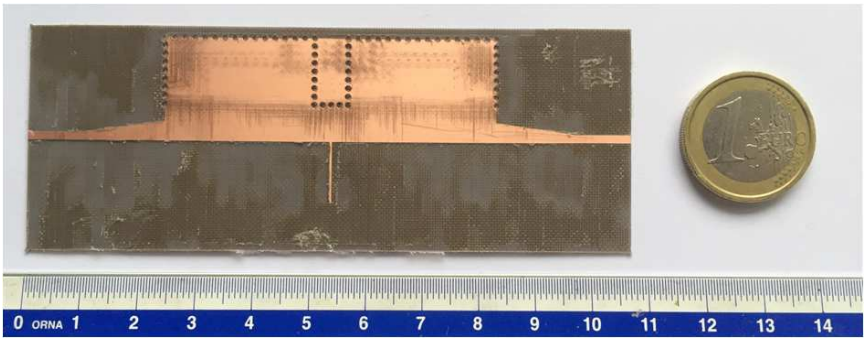

Figure 4.16: Picture of the prototype of the extracted pole Half-Mode filter

filter design is the Taconic TLY-5 (dielectric permittivity $\epsilon_r = 2.2$, loss tangent $\tan\delta = 0.0009$) with thickness 0.51 mm (20 mil). The input and output microstrip tapers are used to couple the filter to the external 50 Ω transmission line.

A prototype of the filter has been fabricated and measured in the Microwave Laboratory of the University of Pavia. A photo of the prototype can be seen in figure 4.16. The response of the filter and the comparison with the simulated model can be seen in figure 4.17. The component has an insertion loss of -1.95 dB. There is a small shift in the frequency of the transmission zero, which lies at ∼4.98 GHz in the measurements and at ∼4.92 GHz in the simulations. This can be attributed to the fabrication tolerance in the dimensions of the resonant stub. The close relation between simulations and measurements confirm the validity of the design. The results have been published in [11].

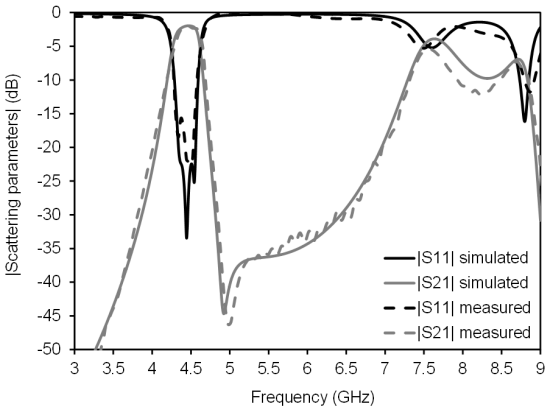

Figure 4.17: Frequency response of the Half-Mode filter

References

[1] C. Tomassoni, L. Pelliccia, F. Cacciamani, P. Vallerotonda, R. Sorrentino, J. Galdeano, and C. Ernst, "Compact broadband waveguide filter with wide spurious-free range based on mixed TM and combline resonators," in *2017 47th European Microwave Conference (EuMC)*, pp. 985–988, 2017.

[2] C. Tomassoni, N. Delmonte, G. Macchiarella, M. Bozzi, and L. Perregrini, "A technique for spurious suppression in substrate integrated waveguide filters," in *2018 48th European Microwave Conference (EuMC)*, pp. 753–756, 2018.

[3] R. J. Cameron, R. Mansour, and C. M. Kudsia, *Microwave Filters for Communication Systems: Fundamentals, Design and Applications*. Wiley, 2007.

[4] S. Amari and J. Bornemann, "Using frequency-dependent coupling to generate finite attenuation poles in direct-coupled resonator bandpass filters," *IEEE Microwave and Guided Wave Letters*, vol. 9, no. 10, pp. 404–406, 1999.

[5] L. Szydlowski, N. Leszczynska, and M. Mrozowski, "Generalized chebyshev bandpass filters with frequency-dependent couplings based on stubs," *IEEE Transactions on Microwave Theory and Techniques*, vol. 61, no. 10, pp. 3601–3612, 2013.

[6] G. Macchiarella, G. G. Gentili, C. Tomassoni, S. Bastioli, and R. V. Snyder, "Design of waveguide filters with cascaded singlets through a synthesis-based approach," *IEEE Transactions on Microwave Theory and Techniques*, vol. 68, no. 6, pp. 2308–2319, 2020.

[7] G. Macchiarella, G. Gentili, and L. Accatino, "Stopband singlet: A novel structure implementing resonating couplings," *IEEE Microwave and Wireless Components Letters*, vol. 30, no. 5, pp. 473–476, 2020.

[8] G. Macchiarella, G. Gentili, N. Delmonte, L. Silvestri, C. Tomassoni, L. Perregrini, M. Mrozowski, and M. Bozzi, "Accurate modeling of stubs used as resonant coupling elements in SIW filters," *IEEE Microwave and Wireless Component Letters*, vol. 30, no. 12, pp. 1125–1128,, 2020.

[9] S. Amari and U. Rosenberg, "New building blocks for modular design of elliptic and self-equalized filters," *IEEE Transactions on Microwave Theory and Techniques*, vol. 52, no. 2, pp. 721–736, 2004.

[10] S. Amari and G. Macchiarella, "Synthesis of inline filters with arbitrarily placed attenuation poles by using nonresonating nodes," *IEEE Transactions on Microwave Theory and Techniques*, vol. 53, no. 10, pp. 3075–3081, 2005.

[11] E. Massoni, N. Delmonte, G. Macchiarella, L. Perregrini, and M. Bozzi, "Half-mode SIW filters with resonant couplings implementing transmission zeros," in *2018 IEEE/MTT-S International Microwave Symposium - IMS*, pp. 701–703, 2018.

Chapter 5

Reconfigurable SIW antenna arrays with amplitude based beam steering

In the last few years, the demand for reconfigurable antennas with beam-forming capabilities has been increasing. For instance, the automotive industrial sector has been studying the implementation of microwave radars as sensors for assisted or autonomous driving systems [1, 2]. In this application, using directive antennas with beam steering capabilities allow for a reduction in the number of required sensors. Another example is the 5G mobile telecommunication standard. In this context, beam-forming antennas are used to maximise the quality of the connection between mobile user and base station, allowing for better coverage and higher data throughput [3, 4].

Reconfigurable antennas can be particularly complex structures, since they may require a large amount of mechanical or active electronic elements in order to operate. This can lead to high fabrication costs, which may limit the scope where these components may be employed.

In this chapter, a particularly simple technique that can be used to obtain an antenna with electronic beam steering capabilities based on phased array technology will be presented. Its advantages over traditional reconfigurable antennas will be shown, along with its drawbacks and limitations.

This chapter is structured as follows: the first section shows an overview of antenna beam steering methods. Particular focus is given to phased arrays, since it acts as the basis of the proposed steering method. The second section presents the simple amplitude based steering technique. Last two sections show the development of two different antennas based on the SIW technology which employ the aforementioned steering method.

All the work presentend in this chapter has been made in collaboration with the research group of Huawei Technologies Italia (Segrate, Milan).

Figure 5.1: Picture of the Sardinia Radio Telescope, example of a deep space antenna employing mechanical beam steering

5.1 Beam steering antennas

The term ”reconfigurable antenna” refers to a device whose radiation properties can be modified and controlled. In particular, an antenna with ”beam steering capabilities” can change its maximum radiation direction. There are two main categories of beam steering techniques: mechanical and electronic.

Mechanical beam steering basically consists in changing the position of the radiation lobes by physically rotating the antenna. This kind of steering method can commonly be seen in large structures like aviation radars and radio telescopes. Mechanical steering has a number of drawbacks. First of all, it requires some sort of motor or actuator in order to obtain the steering effect. Usually, devices with moving parts are subject to wear and may reduce the reliability of the system, or require additional maintenance over time. The physical supports for the radiator has to be sturdy enough to deal with the mechanical stress, which can limit the integration and miniaturization capabilities of the antenna. Moreover, the change in direction of the radiation pattern is limited by the physical turning speed of the antenna, which makes this unsuitable for applications that require very high speed switching. Finally, the high complexity of mechanical steering systems usually result in high fabrication costs.

Electronic beam steering refers to techniques that involve changing the direction of maximum radiation of an antenna without physically moving it. There are many possible strategies that can be used to achieve this effect. An example are antennas with frequency controlled beam steering. these devices usually employ radiators whose radiation pattern changes depending on the frequency of operation. This behaviour can usually be found in electrically large structures, such as leaky-wave antennas [5] or dielectric lenses [6]. Beam-scanning is obtained by simply modifying the frequency of the signal fed into the antenna. While this method can be useful in radar

applications [7, 8], this behaviour may be undesirable when the steering should be applied to a signal with a fixed band (like in telecommunications). Perhaps the most important and flexible electronic beam steering technique is the phased array, which will be discussed in detail in the next section.

5.1.1 Antenna arrays and phased arrays

An antenna array is defined as a group of radiating elements which operate concurrently. Arrays are typically used to obtain antennas with high directivity from simple radiators. An important feature is the possibility to design the radiation pattern of an array by properly selecting its geometrical and electrical properties.

Figure 5.2 shows the example of an array made up of N identical radiating elements. Each element is denoted by the tags $E_1, \ldots, E_N$, and their position relative to the origin is given by the vectors $\mathbf{r}_1, \ldots, \mathbf{r}_N$. Each element is fed by a signal with a certain phase and amplitude. Usually, the values of these signals are normalized to an arbitrary reference value (typically unity). The ratio between the actual excitation of each array element and the reference value is called the *excitation coefficient*, and is indicated by $C_1, \ldots, C_N$. The main tool used to design or study the behaviour of an array is the *array factor* (AF). For a given pointing direction $\hat{\mathbf{r}}$, the array factor can be obtained using the following equation:

$$AF(\theta, \phi) = \sum_{n=1}^{N} C_n e^{j\frac{2\pi}{\lambda}\mathbf{r}_n \cdot \hat{\mathbf{r}}} \tag{5.1}$$

where j is the imaginary unit and λ is the free space wavelength at the operating frequency. After this calculation, all the radiation properties of the array can be obtained by multiplying the radiation pattern of the single radiating element with the array factor (this principle is called *pattern multiplication*). For example, given an array element with the radiation intensity pattern $K_0(\theta, \phi)$, the pattern of the entire array will be:

$$K(\theta, \phi) = K_0(\theta, \phi)|AF(\theta, \phi)|^2 \tag{5.2}$$

A particularly important type of array is the so called *linear uniform array* [9], which is shown in figure 5.3. In this layout all the radiating elements are placed along a straight line, while the distance and the excitation phase difference between adjacent elements is constant throughout the entire array. The synthesis of the array factor of a uniform linear array is particularly convenient. The complex excitation coefficient of each element can be written as:

$$C_n = a_n e^{n\beta} \tag{5.3}$$

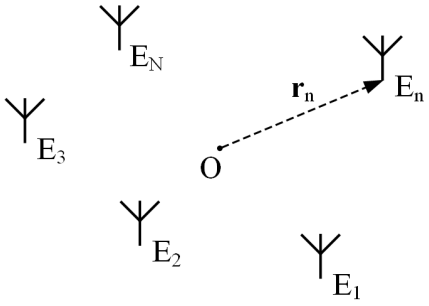

Figure 5.2: Generic antenna array layout

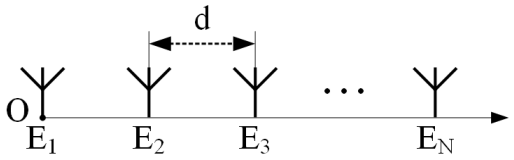

Figure 5.3: Uniform linear array layout

where β is the difference in the phase of the excitation between adjacent array elements. The value of the amplitude a_n is the same for each element, and it is often normalized at the value 1. The formula for the array factor then becomes:

$$AF(\theta) = \sum_{n=1}^{N} a_n e^{j(n-1)(kd\cos\theta+\beta)} \tag{5.4}$$

Thanks to the pattern multiplication principle, the pointing direction of the array is the angle θ_{max} where the amplitude of the array factor reaches its maximum value. The array factor maximum can be easily obtained from the following formula:

$$\theta_{max} = \cos^{-1}\left(\frac{\lambda\beta}{2\pi d}\right) \tag{5.5}$$

It is important to notice that as d grows larger, the equation 5.4 might have one or more maxima in addition to the one computed with equation 5.5. This leads to the appearance of grating lobes and a reduction in the directivity of the array. For this reason, the distance between two elements is usually limited to $d < \lambda/2$.

Equation 5.5 shows that the pointing angle of the linear uniform array depends only on two parameters: the distance d and the excitation phase difference β between adjacent elements. An array with the desired radiation angle can easily be synthesised by selecting the proper values of d and β. Moreover, the array can be designed in order to be able to change these

values during operation. In this way, angle of maximum radiation θ_{max} can be swept, enabling beam steering. In order to modify d, the array element position needs to be changed; this can be complex, especially in the case of arrays with a large amount of elements, and is usually avoided. On the other hand, the excitation phase β can be modified electronically.

An array that exploits the excitation phase of its elements in order to achieve beam steering capabilities is called a *phased array*. Although it is most easily explained and illustrated in the context of uniform linear arrays, the concept of phased arrays is very flexible and can be extended to other topologies, like circular [10] or planar arrays [11, 12], offering a wide range of beam-shaping capabilities.

5.2 Proposed amplitude based beam steering technique

Classic phased array systems allow for a large amount of control in the radiation pattern of the antenna. However, they require the precise tuning of the excitation phase of each and every element of the array. The circuitry that distributes the signal between all the array elements is called the *beam-forming network*, and its design is crucial for the performance of the array. Control over the excitation phase is usually achieved by employing *phase shifters*. A phase shifter is a microwave component which can modify the phase of a signal. In order to scan the radiation pattern, a phased array requires a change in the phase of each element. For this reason, beam-forming networks usually have one phase shifter for each array element. Figure 5.4 shows a couple of examples of beam-forming network layouts.

Phase shifters, like other other active control element, can introduce non-linearities, distortion and additional losses in the array system. Moreover, they increase and the complexity of the beam-forming network and the production costs of the system. The steering mechanism presented in the following section has been developed with the aim of minimizing the amount of control elements in the array, allowing for the design of simple and inexpensive antennas with beam steering capabilities.

5.2.1 Amplitude based steering

The simplest way to illustrate the proposed steering method starts by analyzing a traditional uniform linear phased array. As an example, Figure 5.5 shows a 6 element array, but this study can be extended to any number of elements. The graphs on the left show the distribution of the excitation coefficients along the elements of the array. The value of the coefficients is shown as the combination of amplitude $|A|$ and phase ϕ. Note that being a uniform array, the value of the amplitude is the same for all the elements.

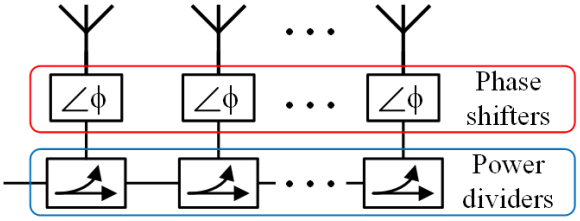

(a) Inline configuration

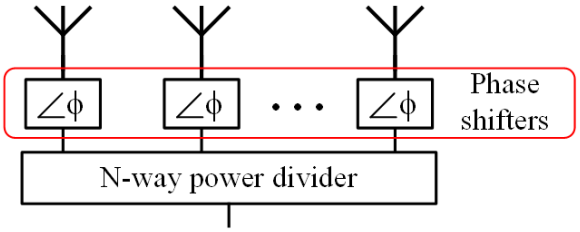

(b) Corporate configuration

Figure 5.4: Examples of beam-forming network layouts

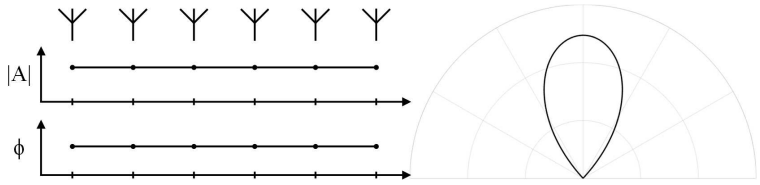

(a) Broadside radiation

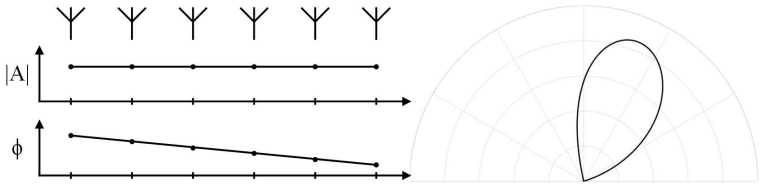

(b) Beam steering

Figure 5.5: Classic phased array steering mechanism

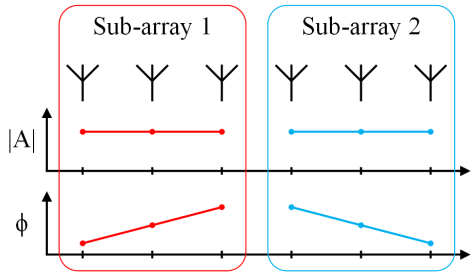

Figure 5.6: Splitting the antenna in two sub-arrays

On the other hand, the plot of the phase distribution forms a line with a certain slope. This slope governs the direction of maximum radiation of the array. In traditional phased array systems, beam steering is obtained by changing this phase slope using phase shifters.

Designing an array without phase shifters means that the phase profile of the system is fixed. It is then necessary to act on different parameters in order to obtain beam steering capabilities. A solution for this problem is to divide the entire array in two equal sub-arrays, as shown in figure 5.6. Each sub-array can be designed independently. Since no phase shifters have to be used, the phase profile of each sub-array is fixed, and so is their radiation pattern. Figure 5.7 shows that what happens to the radiation pattern of the entire array if only one of the two sub-arrays is fed. The value of the amplitude for the elements of the active sub-array is set to 1, while the other elements have an amplitude of 0. In these conditions, the behaviour of the entire array coincides with the single sub-array

Simply switching the feed between the two sub-arrays does not provide actual beam steering, since the entire structure would only radiate towards one of the two directions given by the sub-arrays. In order to properly sweep the radiation pattern, both sub-arrays have to be fed simultaneously, as in figure 5.7c. The graph of the excitation amplitude $|A|$ shows that some amount of signal power is being fed into each sub-array. Under certain conditions that will be explained later in this section, the complete array will radiate towards an intermediate direction between that of the two sub-arrays. This direction can be controlled by changing the ratio of signal power given to each sub-array. When both sub-arrays are fed with the same amount of power, the entire array will radiate towards the mid point. If the phase profile of the two sub-arrays is symmetric (as in figure 5.7c), this will coincide with the broadside radiation.

With this configuration, the sub-arrays effectively dictate the maximum and minimum pointing angle of the entire array. Since their phase profile is fixed, they do not require any phase shifter or other tuning element, and can be fabricated in a cost-effective way by employing simple static transmission lines. The only control element required for this setup is a tunable power

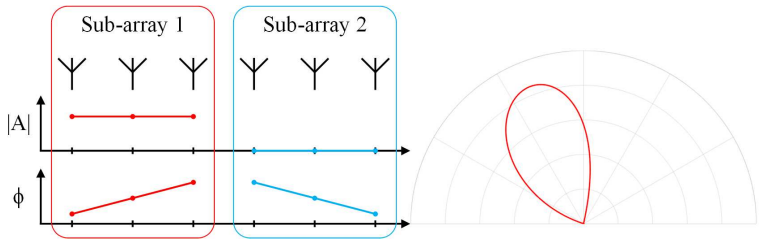

(a) Only sub-array 1 active

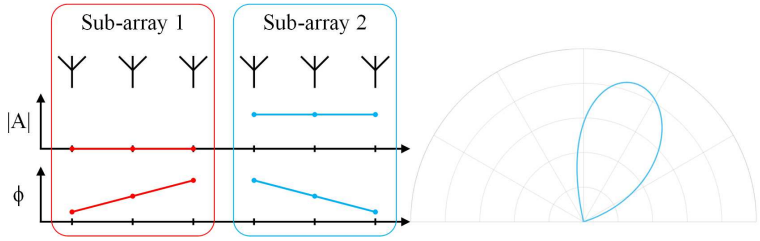

(b) Only sub-array 2 active

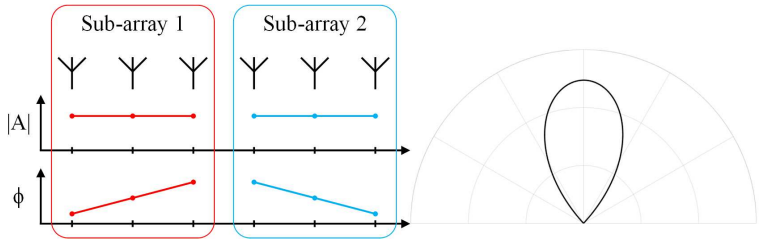

(c) Both sub-arrays active

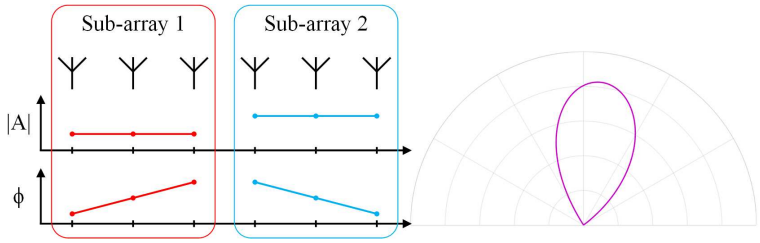

(d) Different sub-array power ratio

Figure 5.7: Amplitude steering method

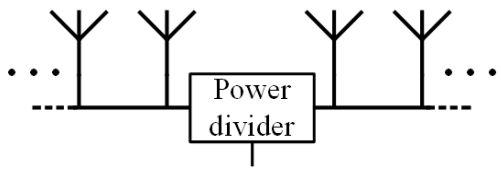

Figure 5.8: Beamforming network with the amplitude steering method

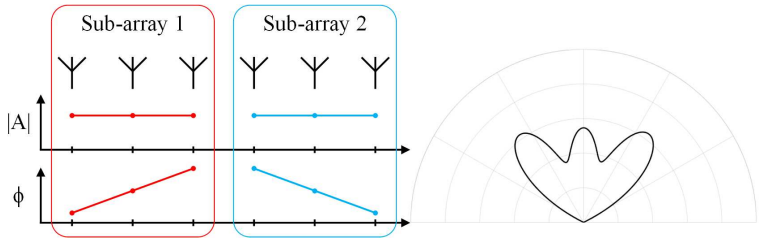

Figure 5.9: Radiation pattern degradation from exceeding pointing angle limits

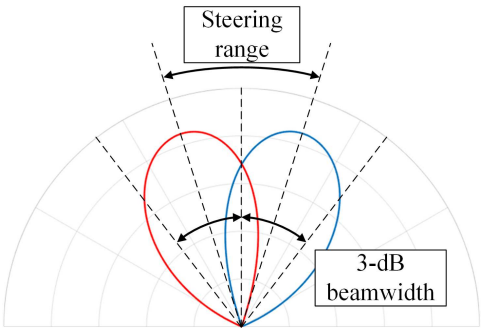

Figure 5.10: Relation between steering range and sub-array main lobe beamwidth

divider that can change the signal power ratio between the sub-arrays. The layout of this configuration is shown in figure 5.8.

5.2.2 Limitations and restrictions of amplitude based beam steering

In order to obtain a smooth and continuous beam-scanning behaviour, some restrictions must be placed in the design of the sub-arrays. In particular, the main radiation lobe of the two sub-arrays must partly overlap. The reason for this is shown in figure 5.9. If the pointing angles of the two sub-arrays are too far apart, when the entire array is fed it will show a radiation pattern with two main lobes. Each of these lobes will point towards the maximum radiation direction of the two sub-arrays. On the other hand, if the radiation pattern of the two sub-arrays is close enough, the entire array will always show a single main radiation lobe. The direction of this lobe depends on the amount of signal power given to each of the sub-arrays.

For this reason, the maximum amount of steering that can be obtained with this method depends on the angular beamwidth of the sub-arrays. The optimal difference in pointing direction of the two sub-arrays that maximises the steering capabilities is equal to their 3-dB beamwidth, as shown in figure 5.10. In this situation, the directivity of the array remains constant in all

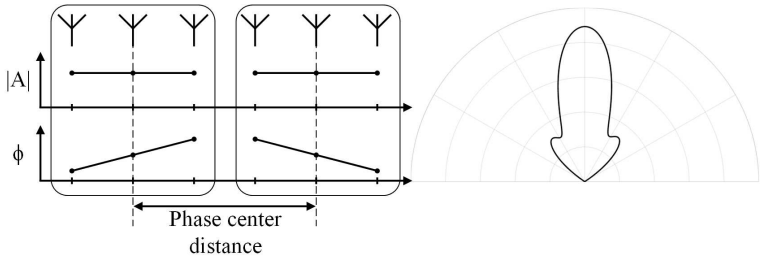

Figure 5.11: Radiation pattern degradation from phase centre distance

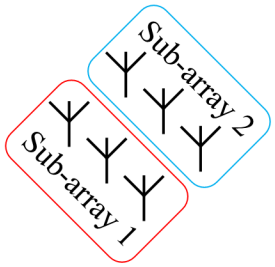

Figure 5.12: Side-by-side sub-array disposition

possible pointing angles. This condition will be called *3-dB rule*. If the sub-arrays don't follow this design rule, the main effect on the behaviour of the array is the onset of *scan loss*, which means that the directivity or gain of the antenna varies with the pointing direction. When the sub-arrays radiation angle difference is smaller than the 3-dB beamwidth, the gain of the entire array will be higher when pointing towards the broadside direction. On the other hand, if the sub-arrays pointing direction is higher than the 3-dB beamwidth, the array will experience a reduction of gain towards broadside. As this difference gets higher, the two main lobes of figure 5.9 start to appear. In all cases, the magnitude of scan loss increases as the design gets further from the 3-dB rule.

When dealing with any kind of antenna, the values of gain, directivity and beamwidth are closely related. High gain, high directivity structures will have small beamwidths and vice versa. The 3-dB rule puts a limit on the amount of steering that can be achieved with the proposed technique for an array with a given directivity.

Another aspect to take into consideration when designing the antenna is the distance between the two sub-arrays. The middle point of each sub-array can be defined as its *phase centre*. As the distance between the phase centres increases, some grating lobes start to appear as shown in figure 5.11. This degrades the performance of the antenna when both sub-arrays are active. In order to avoid this problem, the phase centre distance should ideally be equal to zero. This can be achieved by placing the to sub-arrays side by side

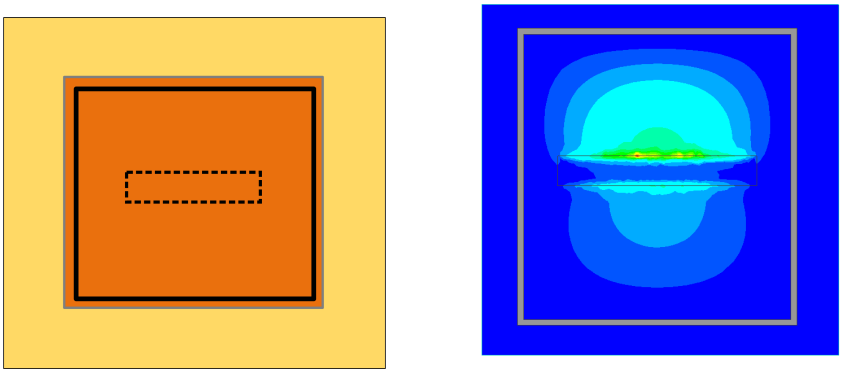

(a) Layout (b) Modal fields

Figure 5.13: Cavity-backed slot antenna element

as in figure 5.12. In this way, the problem is completely avoided. This can be particularly useful as the size of the sub-arrays grows larger.

Finally, an important aspect of the proposed steering technique is related to its efficiency. At any given time, only part of the array is actually being exploited. When the array is pointing towards the maximum steering direction, only one of the two sub-arrays is being fed. When the array is pointing broadside, all the radiation elements are active, but the rooftop phase profile makes the directivity of the structure lower than that of a classic phased array. In all situations, an array of N elements designed with the proposed steering method will have the directivity of a classic phased array of $N/2$ elements. This makes the main deciding factor between the two steering methods the trade-off between the cost and design complexity reduction of the proposed method and the flexibility and efficiency of classic phased arrays.

5.3 5-element SIW cavity-backed slot array

The antenna shown in this section has been developed to demonstrate the potential applications of the proposed amplitude based steering method. The array has been designed to operate at around 27 GHz, at the centre of a band dedicated for 5G communications. The type of radiating element allows for a particularly convenient way to control the signal amplitude distribution along the structure.

5.3.1 SIW cavity-backed slot antenna element

The radiator chosen for the development of the array is the SIW cavity-backed slot antenna [13]. The layout of this radiator is shown in figure

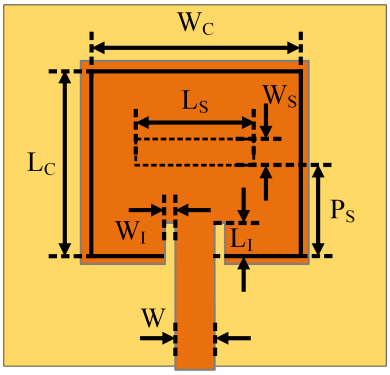

Figure 5.14: Physical parameters of a cavity-backed slot antenna

Physical dimensions	
W	0.71 mm
W_C	4.77 mm
L_C	4.9 mm
W_S	0.5 mm
L_S	3.35 mm
P_S	2.3 mm
W_I	0.1 mm
L_I	0.8 mm

Table 5.1: Design parameters of the cavity-backed slot antenna

5.13a. The antenna consists in a square SIW resonator, with a rectangular cut applied to one of the metal layers of the structure (dashed lines). The resonant mode of the cavity generates an electric field pattern on the open side of the component, which then radiates like a traditional slot antenna. The resonant field distribution of a cavity-backed slot antenna is shown in figure 5.13b.

The radiation properties of the structure depend on its physical design parameters. The dimensions of the array mainly control the frequency of operation of the antenna. The size and position of the slot has an effect on the directivity, bandwidth and frequency of the component. This kind of radiator can obtain good values of directivity and radiation efficiency; however, since the working principle of the antenna is based on the resonant behaviour of the cavity, its frequency bandwidth is relatively small.

An example of cavity-backed slot antenna is shown in figure 5.14. The structure is fed using an microstrip line. In order to properly excite the resonant mode of the cavity, two small insets are placed at the input of the resonator. The component has been designed to work at 27.1 GHz, and is

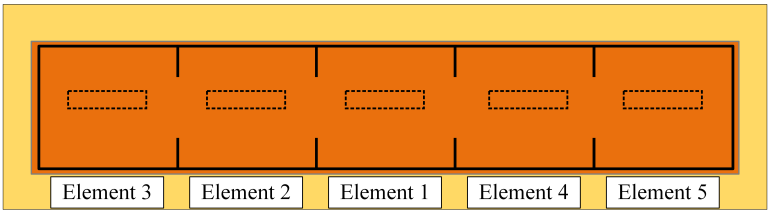

Figure 5.15: Layout of the cavity-backed slot antenna array

based on a substrate with dielectric permittivity $\epsilon_r = 3.34$ and thickness $h = 0.2$ mm. The design parameters of the antenna are shown in table 5.1. The radiator has a -10 dB frequency bandwidth of 200 MHz and a peak directivity of 6.6 dB.

5.3.2 Array design

When creating an antenna array than employs cavity-backed radiators, the presence of the backing resonator can be exploited to reduce the size and complexity of the feeding network. The layout of the designed 5-elements antenna array is shown in figure 5.15. The topology of the array is similar to that of an inline microwave filter: the cavities of adjacent radiators are connected through inductive irises. The coupling between the resonators distributes the signal to all the elements of the array. For this reason, a single microstrip input line has to be connected to only one of the cavities of the structure.

The design goal of the array is to obtain a system gain of 10 dB with at least 20° of scanning range, centred at broadside. Having the steering angle requirements symmetric in respect to the broadside radiation direction greatly decreases the design complexity of the structure, since in this case the radiation pattern of the two sub-arrays simply need to mirror each other. For this reason, the entire array structure will be symmetric. The two sub-arrays are composed of 3 elements which share the central radiator.

The radiation properties of the array are mainly controlled by the amplitude and phase profile of the signal radiated by each element. In this case, the signal power is distributed to the radiating slots by the resonant electromagnetic modes excited in the cavities. This means that all the physical parameters of the antenna (cavity, coupling iris and slot size and relative position) have an effect on the radiated signal distribution. Since there is no analytical or approximate formula for the modal field distribution inside the device, this design step requires the use of numerical simulations.

The signal properties of each radiator have been obtained by measuring the magnitude and phase of the electric field which appear in the middle of each slot, as shown in figure 5.16. This ensures a close relation between the computed parameters and the properties of the fields emitted by each

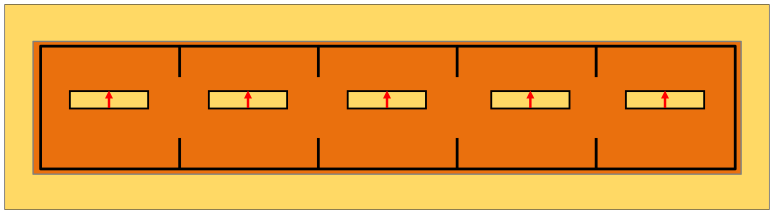

Figure 5.16: Location of electric field used for signal distribution calculation (in red)

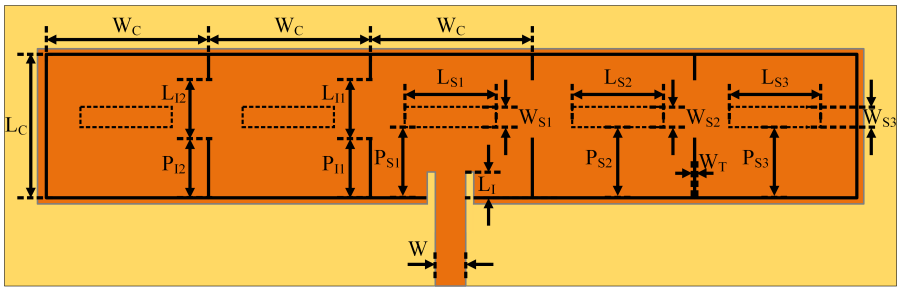

Figure 5.17: Physical parameters of the cavity-backed slot antenna array

radiator.

After the connection of an input microstrip line to the central resonator, the layout of the array is shown in figure 5.17. Using the physical dimensions presented in 5.2 on a substrate with dielectric permittivity $\epsilon_r = 3.34$ and thickness $h = 0.2$ mm, the signal amplitude and phase profiles reported in table 5.3 are obtained at 27.1 GHz. The phase values have been calculated relative to the central slot radiator, which acts as the reference of the array. It can be noticed that the amplitude of the radiated signal decreases for the antenna elements which are further from the input. Overall, the excitation profiles of the sub-arrays result in radiation in a direction 12° from broadside.

5.3.3 Beam steering implementation

In order to obtain beam steering capabilities, it is necessary to control the amount of electromagnetic power that reaches each radiator. A possible strategy consists in acting on the resonant frequency of the backing cavities. If one or more of the antenna elements are detuned, they will no longer accept and radiate the signal.

As it was explained in the previous sections, the frequency of operation of a cavity-backed slot radiator is strongly dependent on the size of the SIW resonator. A smaller cavity corresponds to a higher working frequency. One way to alter the size of a resonator is introducing a shorting via inside the cavity, as shown in figure 5.18a. The metallic via disrupts the modal fields, resulting in an electrically smaller resonator. The effect of the shorting via

Physical dimensions	
W	0.71 mm
W_C	4.5 mm
L_C	4.8 mm
W_{S1}	0.5 mm
W_{S2}	0.5 mm
W_{S3}	0.55 mm
L_{S1}	3.35 mm
L_{S2}	3.4 mm
L_{S3}	3.8 mm
P_{S1}	2.25 mm
P_{S2}	2.25 mm
P_{S3}	2.325 mm
L_{I1}	1.6 mm
L_{I2}	1.4 mm
P_{I1}	2 mm
P_{I2}	1.9 mm
W_I	0.1 mm
L_I	1.1 mm

Table 5.2: Design parameters of the cavity-backed slot antenna array

Element #	3	2	1	4	5
Phase (deg)	-129°	-36°	0°	-36°	-129°
Amplitude (A.U.)	6	18	43	18	6

Table 5.3: Signal excitation profile of the cavity-backed slot antenna array

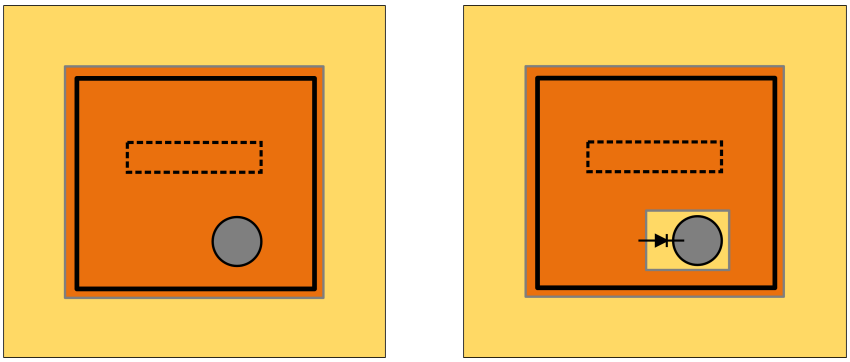

(a) Fixed (b) With PIN diode

Figure 5.18: Shorting via in a cavity-backed slot antenna

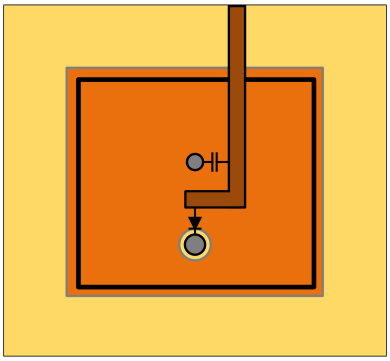

(a) Top view

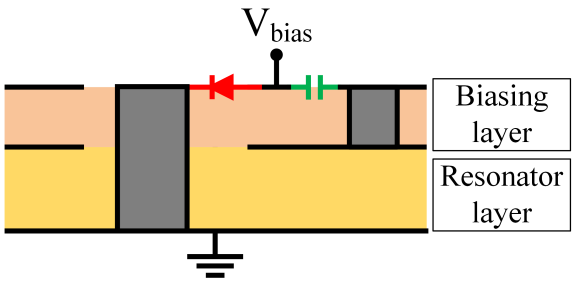

(b) Side view

Figure 5.19: Biasing network for PIN diodes

depends on its size and position. Placing the via where the resonant field (figure 5.13b) is stronger results in a higher frequency shift.

The effect of the shorting vias on the cavities can be controlled electronically with the use of semiconductor devices such as PIN diodes, as shown in figure 5.18b. The PIN diode acts as the connection between the shorting via and the rest of the metal structure. At rest, the diode does not allow any current to flow through it. For this reason, the resonant mode is unaffected by the presence of the via. On the other hand, when a DC voltage is applied to the terminations of the diode, the resistivity of the component drops and the via becomes electrically connected with the metal layers of the cavity, thus shifting the resonant frequency.

The use of PIN diodes requires a biasing network. In order to obtain a useful amount of frequency shift, the shorting via should be placed in the inner parts of the cavity, far from the side walls. In order to deliver the DC biasing signal to that position, a multilayer topology is required. A simple and effecting biasing network is shown in figure 5.19. The resonator lies in the bottom substrate. The shorting via pierces both dielectric layers and is connected to the PIN diode. The biasing voltage is brought to the diode by the L-shaped microstrip, placed above the top substrate. A smaller via closes the circuit by bringing the RF signal back to the resonator. This path

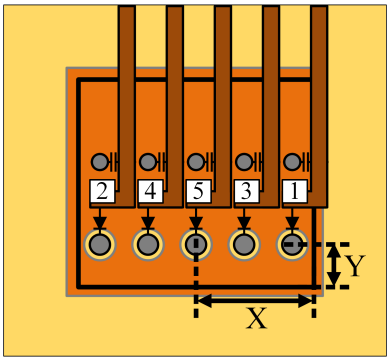

Figure 5.20: Numbering order and physical parameters of multiple shorting vias in cavity-backed slot antennas

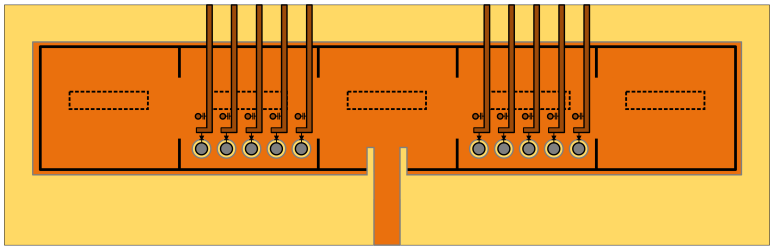

Figure 5.21: Final layout of the cavity-backed slot array with bias networks

is blocked to the DC signal by the use of a small decoupling capacitor.

The amount of power accepted and radiated by the cavity-backed antenna element depends on how much its resonant frequency corresponds to the frequency of the signal. A small detuning results in a small decrease in the radiated power, and vice versa. The resonant frequency of an element can be finely controlled with the use of multiple shorting vias, as shown in figure 5.20. Different combinations of active PIN diodes result in different resonant frequencies. In the context of the array, this means different amount of power entering a sub-array, resulting in multiple pointing angles.

The final layout of the antenna is shown in figure 5.21. Beam steering is obtained by placing 5 PIN controlled shorting vias in two of the side cavities. Since the path of the signal is blocked by tuning these two cavities, is not necessary to place shorting vias in the elements at the edge of the array. All the design parameters are the same as the fixed array shown in the previous section (table 5.2). The size and position of the shorting vias, referring figure 5.20, are shown in table 5.4. All the shorting vias have a diameter of $d = 0.3$ mm. The substrate used for the biasing layer should be thin, in order to have a small impact on the performance of the array. The designed structure employs a substrate with dielectric permittivity $\epsilon_r = 2.2$ and thickness $h = 0.09$ mm. The properties of the PIN diode

Via position		
PIN 1	X_1	0.35 mm
	Y_1	1.3 mm
PIN 2	X_2	3.855 mm
	Y_2	1.3 mm
PIN 3	X_3	1.15 mm
	Y_3	1.1 mm
PIN 4	X_4	2.95 mm
	Y_4	1.1 mm
PIN 5	X_5	2.1 mm
	Y_5	1.8 mm

Table 5.4: Position of the shorting vias of the cavity-backed slot antenna array

Active PIN #	All off	1	2	3	4	5
Pointing angle (deg)	0°	1°	2°	3°	7°	12°
Gain (dB)	10	9.9	9.9	9.8	9.7	9.2

Table 5.5: Radiation properties of the cavity-backed slot antenna array

and the decoupling capacitors have been modelled on the characteristics of two commercially available components for high frequency application. The diode corresponds to a Macom MA4AGBLP912 device, while the capacitor is a Murata 935152722410 component.

The input matching and radiation pattern of the designed array in different PIN diode configurations are shown in 5.22. The antenna parameters at the central frequency of 27.1 GHz are detailed in 5.5. The array has a maximum pointing angle of 12°(resulting in a steering range of 24°), a maximum gain of 10 dB and a scan loss of 0.8 dB.

The results proves the applicability of the amplitude based beam steering technique for SIW antennas operating in the 5G 27 GHz frequency band. However, some problems can be noticed. For example, table 5.5 shows that most of the PIN diodes have a low impact on the pointing angle of the array. This is because ue to space constraints, some of the shorting vias have to be placed on the sides of the cavities, where the intensity of the modal fields is lower. Another thing to take into account is the useful frequency bandwidth of the antenna. While figure 5.22b shows that the array has a fairly wide -10 dB impedance bandwidth of about 880 MHz for all the steering configurations, the signal phase distribution strongly depends with the frequency. For this reason, the array suffers from beam squint effects.

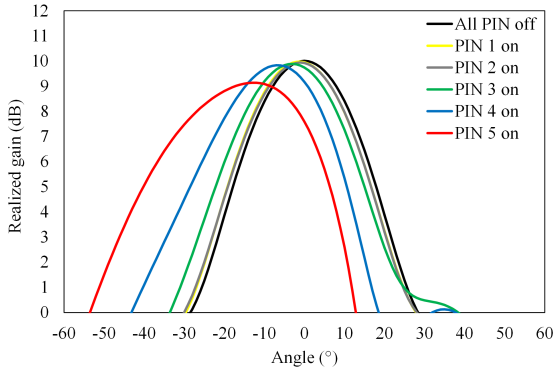

(a) Radiation pattern

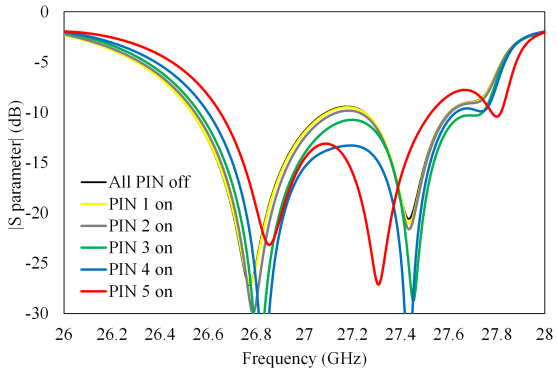

(b) Input matching

Figure 5.22: Behaviour of the cavity-backed slot antenna array

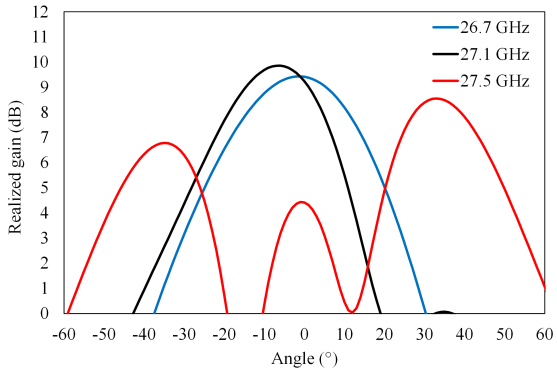

Figure 5.23: Variation of pointing direction of the array in band, when PIN 4 is active

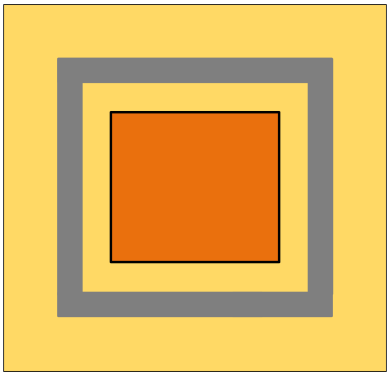

Figure 5.24: Layout of the cavity-backed patch antenna element

Figure 5.23 shows the radiation pattern of the array at different frequencies inside the matching band while PIN 4 is active. This is an intrinsic limit of the topology due to the use of coupled resonators, since different frequencies correspond to different resonant field distributions.

5.4 4x2-element SIW cavity-backed patch array

The problems and limitations of the cavity-backed slot array can be mitigated by employing a different kind of radiator and sub-array topology. This section will present the design of a new array based on the SIW cavity backed antenna element and working in the 28 GHz frequency bandwidth.

5.4.1 SIW cavity-backed patch antenna and element and sub-array design

The layout of a cavity-backed patch radiator is shown in figure 5.24. It consists of a simple microstrip patch resonator, surrounded by SIW metallic walls on all sides. The working principle of this antenna is the same as the classic microstrip patch radiator: the resonant mode of the patch creates some fringing fields along the edge of the metal. The illumination from these fields radiate the electromagnetic power outside the structure. Compared to traditional patch antennas, cavity-backed structures have improved frequency bandwidth and reduced parasitic coupling effects [14, 15]. The complexity of the cavity-backed patch antenna is comparable to the simple patch radiator, and it is compatible with inexpensive fabrication techniques such as PCB. Patch antennas have a high level of versatility. Depending on the design requirements, the patch can take many different shapes. In the context of this work, the simple rectangular patch topology has been selected in order to obtain a clean linearly polarized radiated field.

An example of cavity-backed patch antenna is shown in figure 5.25. The

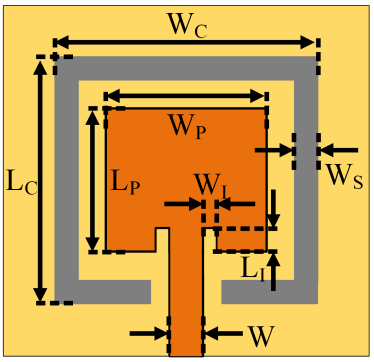

Figure 5.25: Physical parameters of a cavity-backed patch antenna

Physical dimensions	
W	0.2 mm
W_C	4.55 mm
L_C	4.55 mm
W_P	3.15 mm
L_P	3.15 mm
W_I	0.1 mm
L_I	0.93 mm
W_S	0.2 mm

Table 5.6: Design parameters of the cavity-backed patch antenna

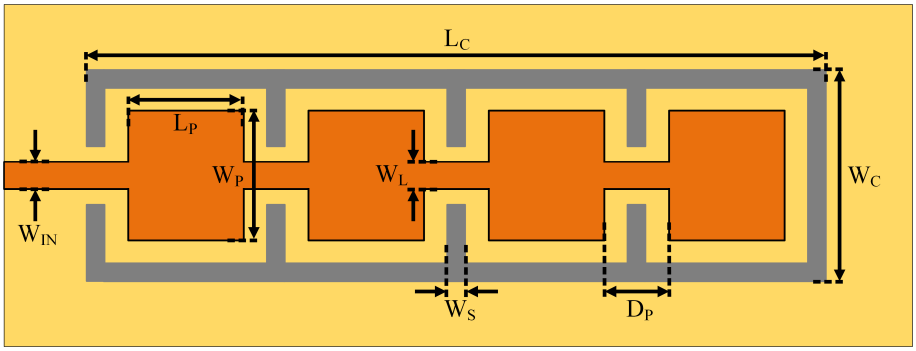

Figure 5.26: Layout of the cavity-backed patch antenna sub-array

Physical dimensions	
W_{IN}	0.4 mm
W_C	5 mm
L_C	24.44 mm
W_P	3.6 mm
L_P	3.3 mm
D_P	2.76 mm
W_L	3.35 mm
W_S	0.2 mm

Table 5.7: Design parameters of the cavity-backed patch antenna sub-array

resonator is connected with the output through a short microstrip line. Two small insets are used to properly couple the radiator with the output fields. The resonant frequency of the antenna is mainly controlled by the physical dimensions of the patch, while the backing SIW cavity has a lower impact on the radiation properties. The component has been designed to work at 28 GHz, on a substrate with dielectric permittivity $\epsilon_r = 2.2$ and thickness $h = 0.76$ mm. Note that, due to the relatively high thickness and low permittivity of the substrate, the antenna is matched to a microstrip line with impedance of 150 Ω. This was done since a canonic 50 Ω transmission line would have been much wider and more difficult to couple. However, since the radiators presented in this section do not need to be connected directly to a measurement device or a signal source, the input impedance has no effect on the performance of the structure. The design parameters of the antenna are shown in table 5.6. The radiator has a -10 dB frequency bandwidth of 1.5 GHz and a peak directivity of 6.4 dB.

The first step in the creation of the array is the design of the sub-arrays. When dealing with patch resonators, a very simple and effective topology is the inline configuration shown in figure 5.26. A number of patches are

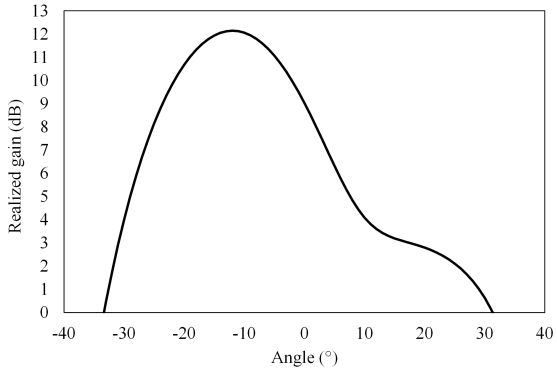

(a) Radiation pattern

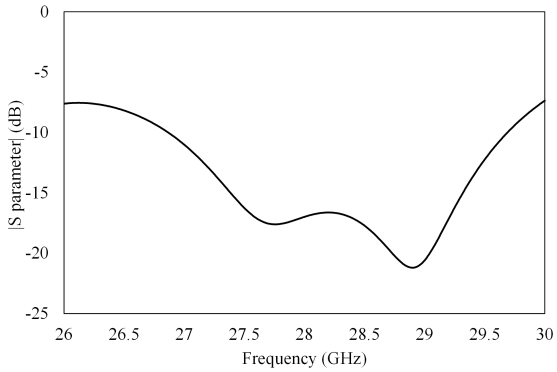

(b) Input matching

Figure 5.27: Behaviour of the cavity-backed patch antenna sub-array

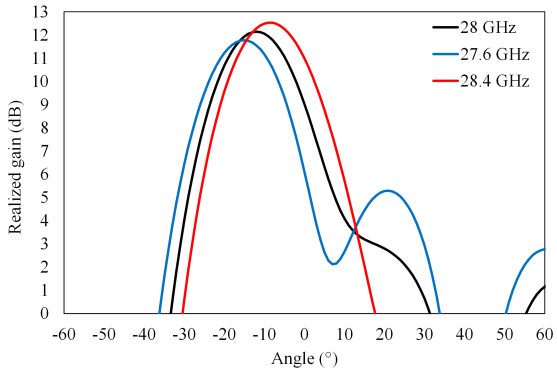

Figure 5.28: Variation of pointing direction of the sub-array in the matching band

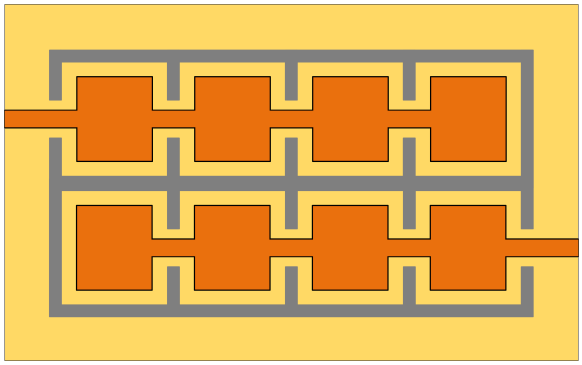

Figure 5.29: Side by side configuration of the sub-arrays

	27.6 GHz	28 GHz	28.4 GHz
Pointing angle (deg)	15°	12°	9°
Gain (dB)	11.7	12.1	12.6

Table 5.8: Radiation properties of the cavity-backed slot antenna sub-array

placed in series, and are connected using some microstrip lines. The signal can travel through these lines, and can reach all the radiators of the sub-array. The signal phase distribution, and as a consequence the direction of the main radiation lobe of the structure, depends on the distance between the patches and the length of the connecting microstrip lines. The overall array requires 20° of scanning range centred at broadside. For this reason, the sub-array has been chosen to have 4 radiating elements. The physical parameters of the designed sub-array are presented in table 5.7. All the patches of the sub-array have the same dimensions. The structure is based on a substrate with dielectric permittivity $\epsilon_r = 2.2$ and thickness $h = 0.76$ mm. The input matching and the radiation pattern of the structure are shown in figure 5.27. The structure features a very wide -10 dB matching bandwidth of 2.8 GHz, and a peak directivity value of 12.1 dB at 28 GHz.

Since the steering range of the overall array is symmetric in respect to the broadside direction, the two sub-arrays are simply the mirrored copy of each other. The two sub-arrays can be placed beside each other as shown in figure 5.29. This topology minimizes the distance between the sub-arrays, ensuring that no grating lobes appear in the radiation pattern of the array.

The signal phase distribution along the element of the inline sub-array will change depending on the frequency. This will result in a change in the direction of the main radiation lobe at different frequencies. Figure 5.28 shows the radiation pattern of the antenna at 27.6 GHz and 28.4 GHz. The radiation parameters at those frequencies are summarised in table 5.8. Even

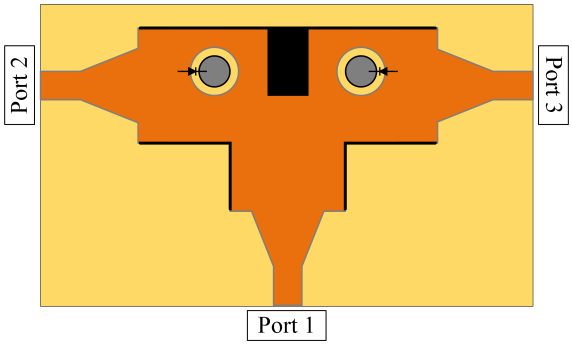

Figure 5.30: Layout of the SIW reconfigurable power divider

if the problem has not been completely eliminated, the cavity-backed patch array shows a large improvement in the amount of beam squint compared to the structure based on cavity-backed slot radiators.

5.4.2 Steering implementation

In order to control the pointing direction of the array, the overall system requires a device that can route the right amount of signal power to each sub-array. For that reason, a reconfigurable power divider has been designed. The layout of the component is shown in figure figure 5.30. The structure is based on a matched SIW tee junction. Port 1 is the input of the device. In normal conditions, the structure divides the incoming signal power equally between port 2 and port 3. The signal is delivered to the structure through microstrip waveguides. The transition to the SIW is obtained by tapering the microstrip. The metal inset placed in the centre of the topology ensures a good level of isolation between the output ports. The structure has been modified by placing two shorting vias on the sides of the junction. These vias are controlled by PIN diodes. When a via is connected to the metal layer of the device, it blocks the signal from travelling through the side of the structure where it is placed. This effect is illustrated by the electric field patterns that are created inside the structure, shown in figure 5.31.

The PIN diodes require a DC biasing voltage in order to operate. The bias signal can be delivered to the diodes with a dual layer setup similar to the one employed for the cavity-backed slot radiators (figure 5.19). In this case, four PIN diodes have been used for each shorting via, in the configuration shown in figure 5.32. The induced modal current gets distributed between the multiple diodes, resulting in lower effective series resistance. The cross configuration allows to better intercept the modal current distribution, increasing the effectiveness of the shorting via. Moreover, the redundancy increases the tolerance of the structure to fabrication and assembly errors.

The physical dimensions of the designed divider referring to figure 5.33

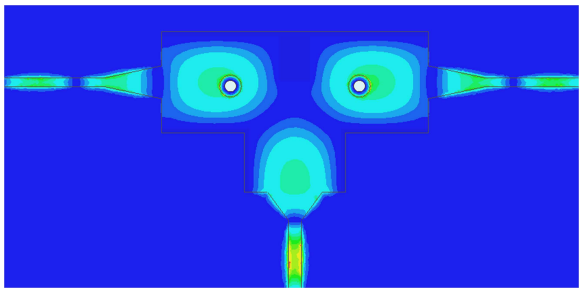

(a) All PIN diodes off

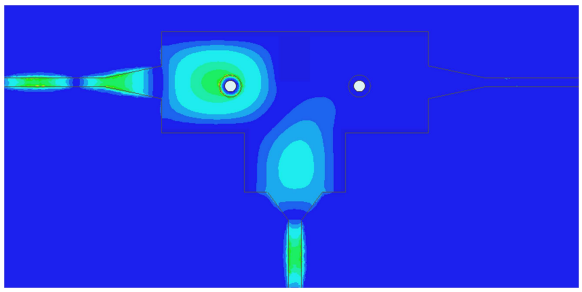

(b) Right PIN diode on

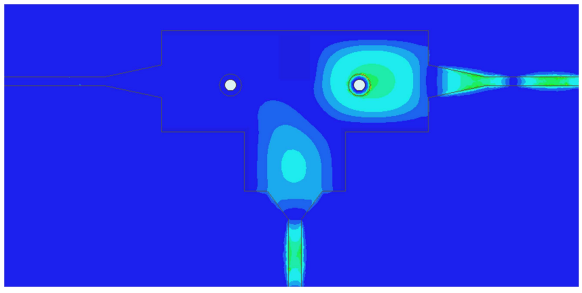

(c) Left PIN diode on

Figure 5.31: Electric field patterns inside the SIW reconfigurable power divider

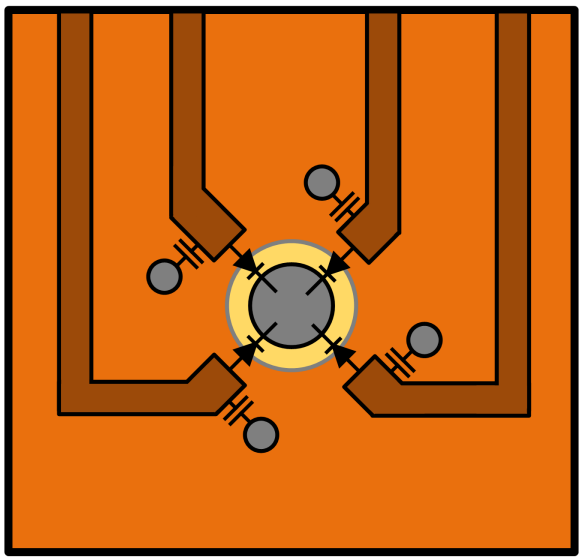

Figure 5.32: Cross configuration of the PIN diodes for the shorting vias of the reconfigurable power divider

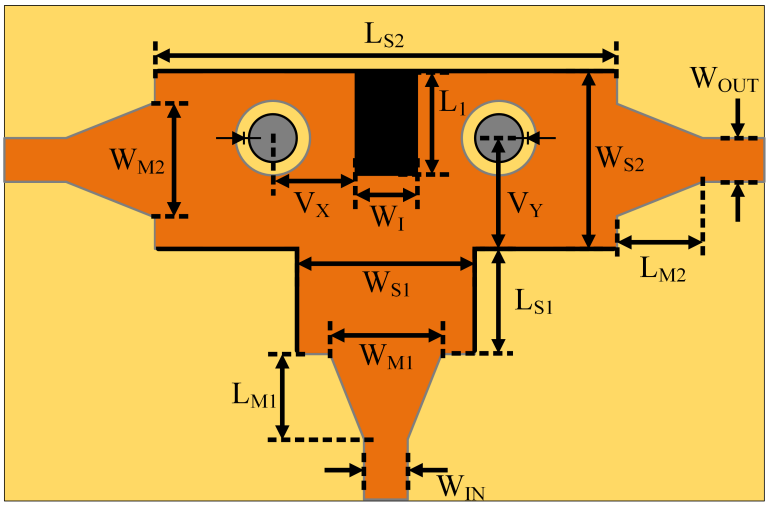

Figure 5.33: Physical parameters of the SIW reconfigurable power divider

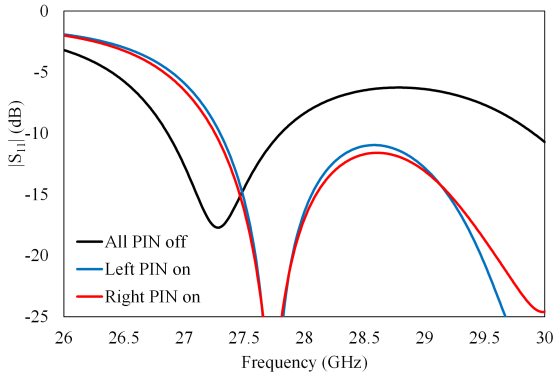

(a) Input matching

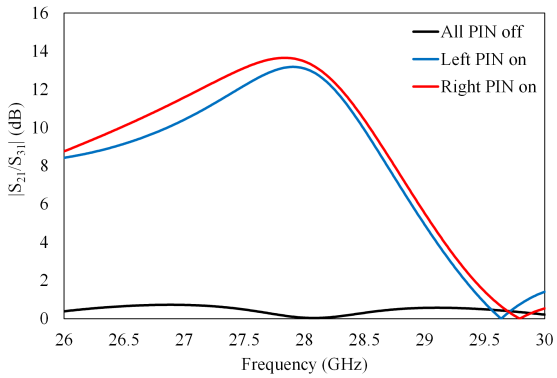

(b) Output power ratio

Figure 5.34: Frequency response of the SIW reconfigurable power divider

Physical dimensions	
W_{IN}	0.6 mm
W_{OUT}	0.4 mm
W_{S1}	4.4 mm
W_{S2}	4.4 mm
L_{S1}	3 mm
L_{S2}	12.63 mm
W_{M1}	2.6 mm
W_{M2}	1.56 mm
L_{M1}	1.35 mm
L_{M2}	2.75 mm
W_I	1.39 mm
L_I	2.1 mm
V_X	2.365 mm
V_Y	2.02 mm

Table 5.9: Design parameters of the SIW reconfigurable power divider

are shown in table 5.9. The structure is symmetric, so the position of the vias are the same for both sides of the device. The divider employs a dual layer topology. The main substrate layer where the SIW structure can be found is tall $h_1 = 0.13$ mm, while the layer used for the biasing network has thickness $h_2 = 0.09$ mm. Both layers are made up of a substrate with dielectric permittivity $\epsilon_r = 2.2$. The shorting vias of the structure have diameter $d = 0.54$ mm. The input matching of the device is shown in 5.34a. The response of the device suffers from a shift as the diodes are activated. Figure 5.34b shows the ratio of signal delivered between the two ports. The device can reach up to 13 dB of difference in the frequency band around 28 GHz. This value is enough to ensure that the array can reach the maximum amount of steering given by the sub-array design.

5.4.3 Complete array layout

In order to save space and increase the miniaturization of the array, the power divider and the radiators can be placed on top of each other, employing a multilayer configuration as shown in figure 5.35. The two layers at the bottom of the figure are both dedicated to the power divider: in particular, one of them will have the bias and control circuitry, while the other will contain the SIW tee junction. The cavity backed patch radiators lay on the top layer. The signal can be routed between the substrate layers by using metallized vias. The reconfigurable power divider (area ∼12.6 x 3.9 mm) can comfortably fit under the footprint of the two sub-arrays (∼22.4 x 10

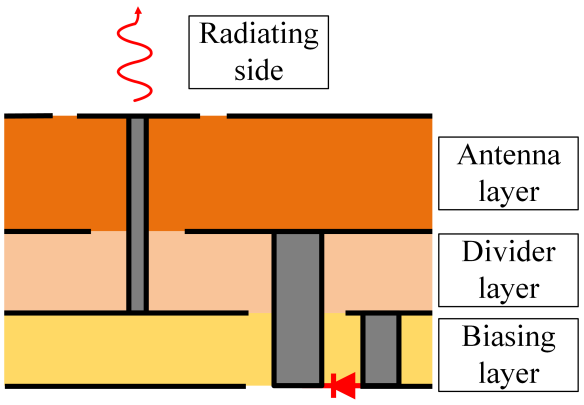

Figure 5.35: Multilayer configuration of the final cavity-backed patch antenna array design

mm). An advantage of this topology is that the signal input and control systems are separated from the radiating side of the array, making the antenna easier to connect and measure.

After the integration of the power divider with the radiators, the antenna structure will be composed of 3 dielectric substrates and 4 metal layers. The final antenna design has been engineered in order to be suitable for the fabrication of a physical prototype. The substrate chosen for the antenna layer is the Taconic TLP-5 ($\epsilon_r = 2.2$, $\tan\delta = 0.0009$) with thickness $h_1 = 0.787$ mm. The dielectric used for the layers of the SIW tee junction and the control circuitry is a Taconic TLY-5 laminate (same properties of the TLP-5), with thickness of $h_2 = 0.19$ mm and $h_3 = 0.089$ mm respectively.

The layouts of all the metal layers of the final array design are shown in figure 5.36. The antenna radiates from the side of metal layer 1 (figure 5.36a), where the cavity-backed patches can be found. The sub-arrays receive the signal from the rest of the system trough two small metallized vias placed at the end of the microstrip lines that lay on the side of the structure. Metal layer 2 (figure 5.36b) separates the radiators from the power divider. The via used to transfer the signal power to the sub-arrays passes through the two circular holes found in the sides. The SIW tee junction is placed at the centre of metal layer 3 (figure 5.36c). The signal is delivered to the radiators using two microstrip transmission lines. The signal path length for the two sub-arrays has a difference of half-wavelength: this is because in order to radiate toward broadside, the signal of the sub-arrays require a 180° offset. Finally, the steering control components and their biasing networks can be found on metal layer 4 (figure 5.36d). The square pads are used to drive the DC bias voltage of the diodes. The RF signal microstrip line in the middle of the structure is the input of the antenna, and it is meant to be connected to a 50 Ω RF connector. The holes at the bottom are required

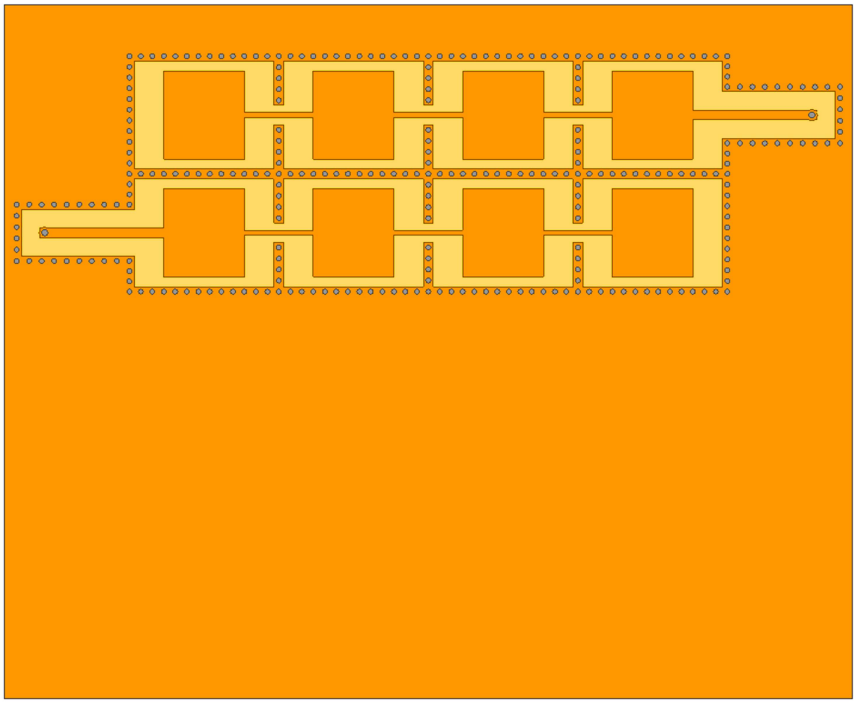

(a) Metal layer 1: patch radiators

(b) Metal layer 2: transition

Figure 5.36: Final structure of the cavity-backed patch antenna array

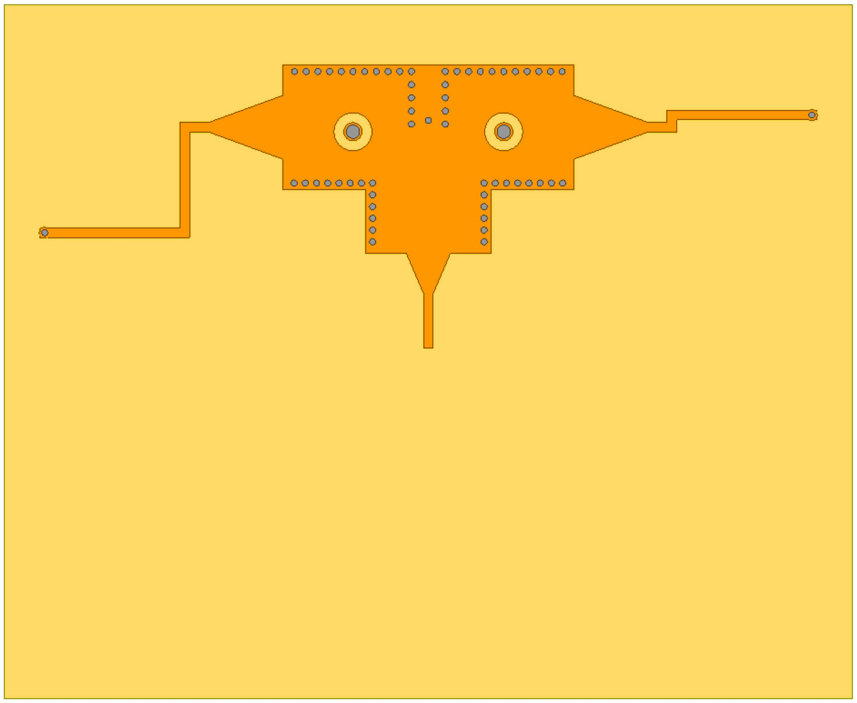

(c) Metal layer 3: SIW divider

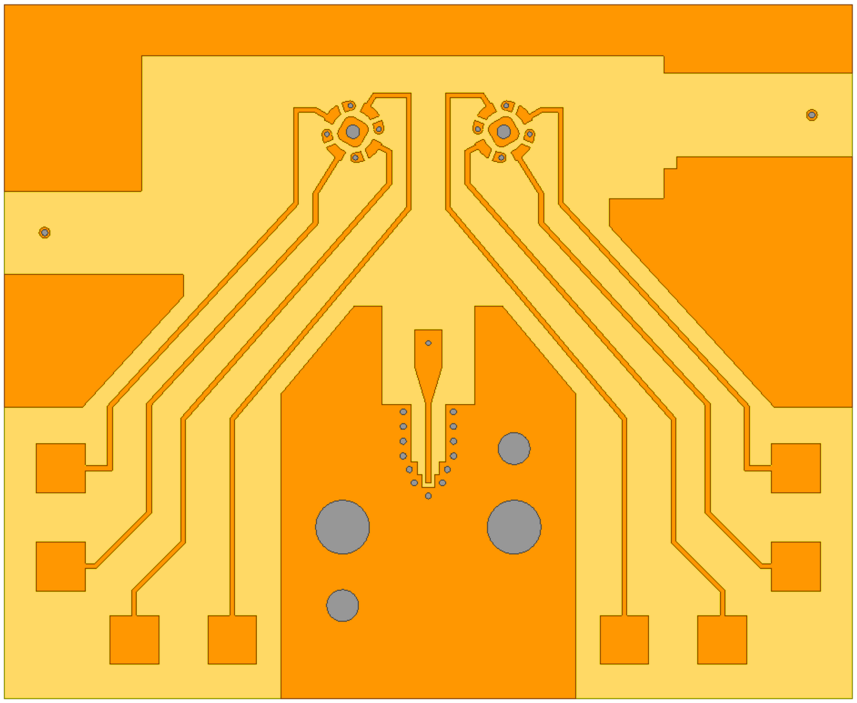

(d) Metal layer 4: input and biasing

Figure 5.36: Final structure of the cavity-backed patch antenna array

Active PIN	All off	Left on	Right on
Pointing angle (deg)	0°	11°	-11°
Gain (dB)	9.7	9.8	9.6

Table 5.10: Radiation properties of the complete cavity-backed patch antenna array at 28 GHz

for the alignment pins and the matching of the connector.

The integration process requires a re-tuning of all the physical dimensions of the structure. Figures 5.37-5.40 show in detail the design parameters of the main parts of the structure. The dimensions have been calculated taking into account the effects of the fabrication process on the prototype. The substrate layers are connected using a 50 μm sheet of the adhesive film Rogers Bondply 2929 ($\epsilon_r = 2.94$, $\tan\delta = 0.003$). The PIN diode chosen for the implementation of the array is the Macom MA4GP907, while the capacitor is the Murata 939114722410. Both components are designed for high frequency application, and rated to work up to 40 GHz. The small form factor of the two components allow to create a compact biasing circuit to minimize their impact over the performance of the antenna. Each array employs a total of 8 PIN diodes and 8 capacitors. The prototypes are going to be connected to the test setup using a Rosenberger 08K80A-40ML5 1.85 RF surface mounted connector.

The results of the simulation of the complete array are shown in figure 5.41 and table 5.10. In the central frequency of 28 GHz, the antenna achieves a 22°scanning range, with a peak gain of 9.8 dB and a scan loss of 0.2 dB. The input matching of the antenna varies with the active PIN configuration, but in all cases the -10 dB bandwidth is larger than 1 GHz. The gain of the system is lower compared to the synthesised sub-array due to extra loss contributions coming from the transitions, the internal transmission lines and the discrete components. Still, the design successfully achieves the beam-steering capabilities employing a simple topology.

The behaviour of the array has been studied in a 800 MHz band around the central frequency. Figure 5.42 and table 5.11 show the radiation properties of the array at 27.6 GHz and 28.4 GHz. As it was shown in the previous section, the radiated signal phase profile inside the inline patch sub-array tends to vary with the frequency, resulting in the change of the sub-array pointing direction. As a consequence, the radiation pattern of the complete array is also affected. When the control PIN diodes are inactive, the array keeps its pointing direction towards broadside thanks to the symmetry of the structure. However, the gain of the antenna changes, lowering by around 2.2 dB in the worst case. When the PIN diodes are active, the array suffers from a decrease in gain and a change in the maximum radiation direction

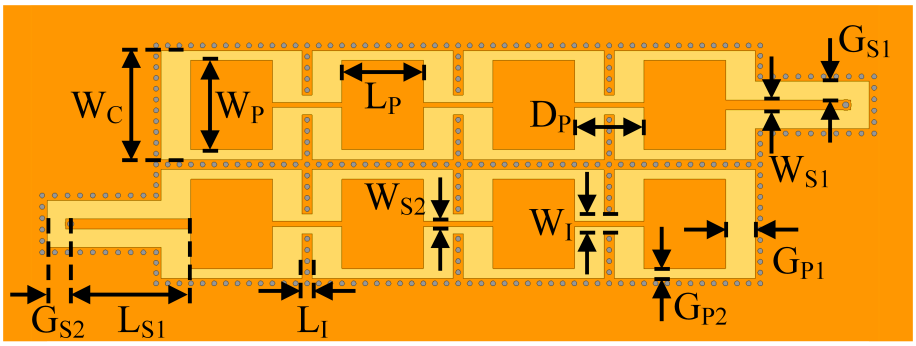

(a) Layout

Physical dimensions	
W_P	3.6 mm
L_P	3.3 mm
D_P	2.8 mm
G_{P1}	1.2 mm
G_{P2}	0.4 mm
W_{S1}	0.4 mm
W_{S2}	0.2 mm
G_{S1}	0.75 mm
G_{S2}	0.75 mm
L_{S1}	4.85 mm
L_I	0.4 mm
W_I	0.8 mm
W_C	4.4 mm

(b) Physical dimensions

Figure 5.37: Detail of the sub-arrays (metal layer 1) of the final cavity-backed patch antenna array design

Frequency		27.6 GHz	28 GHz	28.4 GHz
All PIN off	Pointing angle (deg)	0°	0°	0°
	Gain (dB)	7.5	9.7	10.5
Left PIN on	Pointing angle (deg)	14°	11°	8°
	Gain (dB)	8.7	9.8	8.7
Right PIN on	Pointing angle (deg)	-14°	-11°	-8°
	Gain (dB)	8.8	9.6	8.9

Table 5.11: Effect of frequency on the radiation of the complete cavity-backed patch antenna array

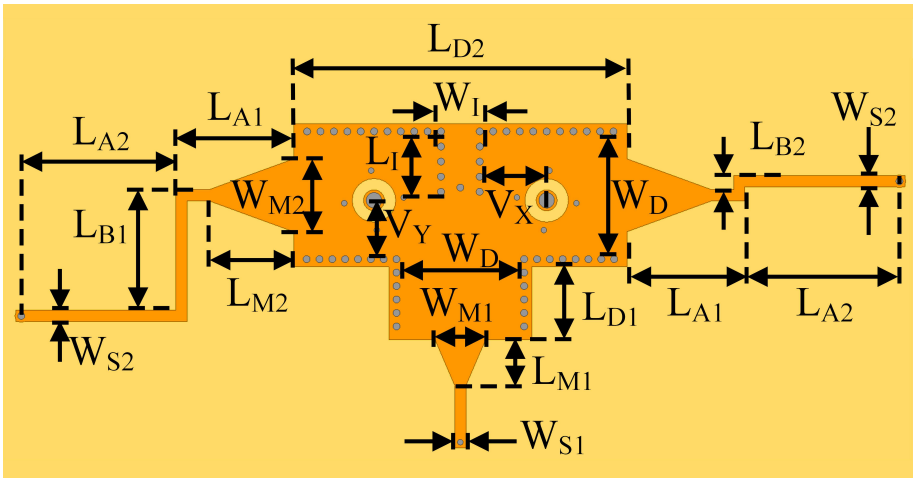

(a) Layout

Physical dimensions	
L_{D1}	2.875 mm
L_{D2}	11.875 mm
W_D	4.55 mm
W_{S1}	0.4 mm
W_{S2}	0.4 mm
W_{M1}	1.8 mm
W_{M2}	2.6 mm
L_{M1}	1.63 mm
L_{M2}	3.02 mm
L_{A1}	4.2 mm
L_{A2}	5.512 mm
L_{B1}	4.3 mm
L_{B2}	0.5 mm
W_I	1.38 mm
L_I	1.15 mm
V_X	2.387 mm
V_Y	2.095 mm

(b) Physical dimensions

Figure 5.38: Detail of the SIW tee junction (metal layer 3) of the final cavity-backed patch antenna array design

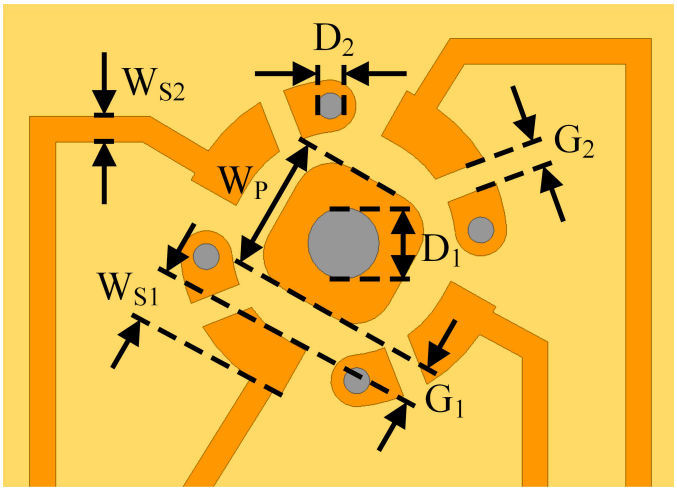

(a) Layout

Physical dimensions	
D_1	0.55 mm
D_2	0.2 mm
G_1	0.33 mm
G_2	0.2 mm
W_P	1.07 mm
W_{S1}	0.4 mm
W_{S2}	0.2 mm

(b) Physical dimensions

Figure 5.39: Detail of the PIN diode biasing network (metal layer 4) of the final cavity-backed patch antenna array design

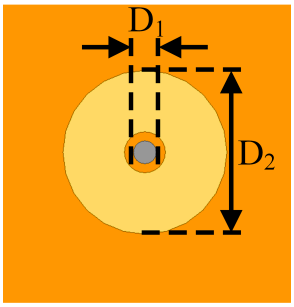

(a) Layout

Physical dimensions	
D_1	0.25 mm
D_2	1.8 mm

(b) Physical dimensions

Figure 5.40: Detail of the connection between power divider and sub-arrays (metal layer 2) of the final cavity-backed patch antenna array design

In all cases, the squint of the beam reaches 3°.

A set of assembled physical prototypes of the SIW cavity-backed patch antenna array system has been commissioned. Figure 5.43 shows a few pictures of the prototypes.

The designed array shows that the SIW technology and the amplitude based steering technique have potential applications in the 5G 28 GHz frequency band. Further research can improve the performance of the current array design in a number of ways. For example, right now the SIW power divider only operates in three different states. The development of a more refined component with an increased number of control items can lead to the creation of a power divider with more available dividing ratios, allowing the array to obtain an increased number of intermediate pointing angles. Another research avenue is an increase of the directivity of the array. In order to increase the gain without sacrificing the maximum achievable steering angle, a set of amplitude based arrays can be cascaded as shown in figure 5.44. The arrays effectively act as the elementary radiating elements of a larger phased array. Depending on the order the directivity of each amplitude based array, this configuration may still result in a reduced number of phase shifter and control elements compared to an equivalent antenna based on the traditional phased array topology. Preliminary investigations are being conducted on a set of 4 amplitude based arrays (figure 5.45).

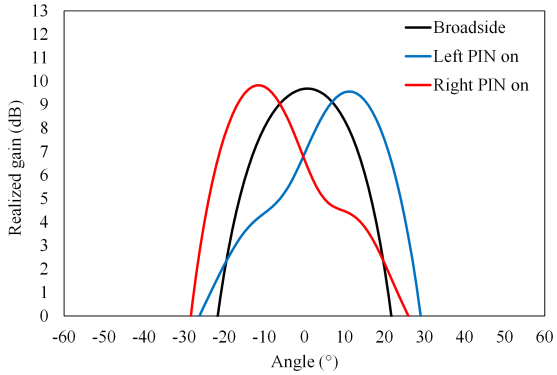

(a) Radiation pattern at 28 GHz

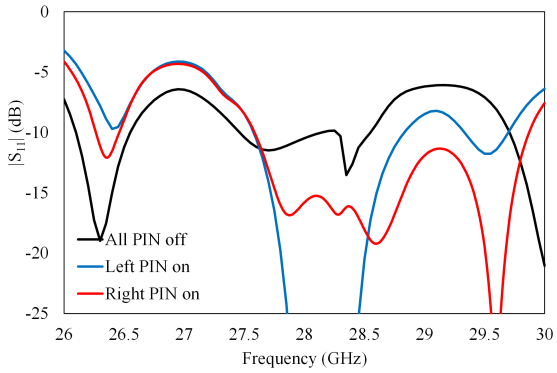

(b) Input matching

Figure 5.41: Behaviour of the complete cavity-backed patch antenna array

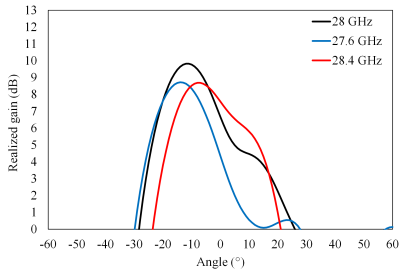

(a) Right PIN on

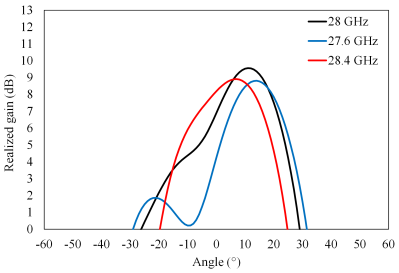

(b) Left PIN on

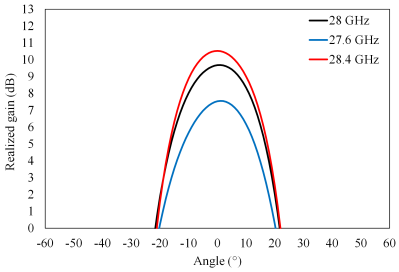

(c) All PIN off

Figure 5.42: Variation of radiation pattern of the sub-array in the matching band

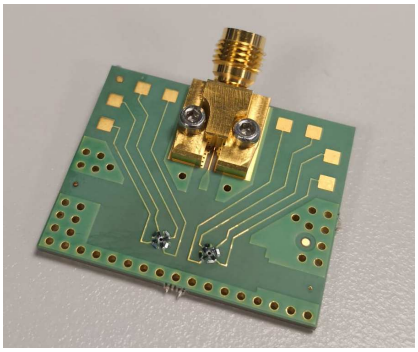

(a) Input and bias side

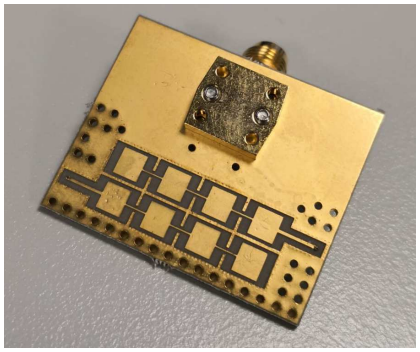

(b) Radiating side

Figure 5.43: Pictures of the cavity-backed patch antenna array physical prototypes

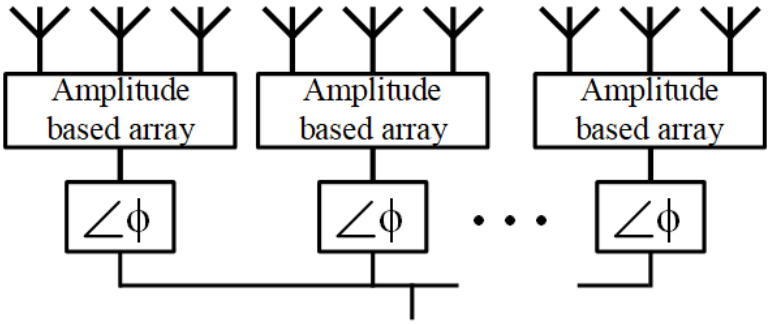

Figure 5.44: Multistage array configuration for improved directivity

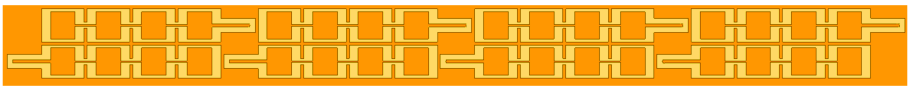

Figure 5.45: 4x1 topology of amplitude based cavity-backed patch arrays

References

[1] M. Dudek, I. Nasr, G. Bozsik, M. Hamouda, D. Kissinger, and G. Fischer, "System analysis of a phased-array radar applying adaptive beam-control for future automotive safety applications," *IEEE Transactions on Vehicular Technology*, vol. 64, no. 1, pp. 34–47, 2015.

[2] U. Chipengo, "Full physics simulation study of guardrail radar-returns for 77 GHz automotive radar systems," *IEEE Access*, vol. 6, pp. 70053–70060, 2018.

[3] W. Roh, J. Seol, J. Park, B. Lee, J. Lee, Y. Kim, J. Cho, K. Cheun, and F. Aryanfar, "Millimeter-wave beamforming as an enabling technology for 5G cellular communications: theoretical feasibility and prototype results," *IEEE Communications Magazine*, vol. 52, no. 2, pp. 106–113, 2014.

[4] E. G. Larsson, O. Edfors, F. Tufvesson, and T. L. Marzetta, "Massive MIMO for next generation wireless systems," *IEEE Communications Magazine*, vol. 52, no. 2, pp. 186–195, 2014.

[5] R. Ranjan and J. Ghosh, "SIW-based leaky-wave antenna supporting wide range of beam scanning through broadside," *IEEE Antennas and Wireless Propagation Letters*, vol. 18, no. 4, pp. 606–610, 2019.

[6] H. Yi, S. Qu, K. Ng, C. H. Chan, and X. Bai, "3-D printed millimeter-wave and terahertz lenses with fixed and frequency scanned beam," *IEEE Transactions on Antennas and Propagation*, vol. 64, no. 2, pp. 442–449, 2016.

[7] D. A. Schneider, M. Rösch, A. Tessmann, and T. Zwick, "A low-loss W-band frequency-scanning antenna for wideband multichannel radar applications," *IEEE Antennas and Wireless Propagation Letters*, vol. 18, no. 4, pp. 806–810, 2019.

[8] A. Shoykhetbrod, A. Hommes, and N. Pohl, "A scanning FMCW-radar system for the detection of fast moving objects," in *2014 International Radar Conference*, pp. 1–5, 2014.

[9] C. A. Balanis, *Antenna Theory: Analysis and Design, 3rd Edition*. Wiley, 2005.

[10] N. C. Karmakar, M. E. Bialkowski, and S. K. Padhi, "Microstrip circular phased array design and development using microwave antenna CAD tools," *IEEE Transactions on Antennas and Propagation*, vol. 50, no. 7, pp. 944–953, 2002.

[11] D. Pozar and D. Schaubert, "Analysis of an infinite array of rectangular microstrip patches with idealized probe feeds," *IEEE Transactions on Antennas and Propagation*, vol. 32, no. 10, pp. 1101–1107, 1984.

[12] Y. Cheng, X. Ding, W. Shao, M. Yu, and B. Wang, "2-D planar wide-angle scanning-phased array based on wide-beam elements," *IEEE Antennas and Wireless Propagation Letters*, vol. 16, pp. 876–879, 2017.

[13] G. Q. Luo, Z. F. Hu, L. X. Dong, and L. L. Sun, "Planar slot antenna backed by substrate integrated waveguide cavity," *IEEE Antennas and Wireless Propagation Letters*, vol. 7, pp. 236–239, 2008.

[14] M. H. Awida, E. Elkhouly, and A. E. Fathy, "Low-cost high-efficiency substrate-integrated cavity-backed single element antenna," in *2010 IEEE Antennas and Propagation Society International Symposium*, pp. 1–4, 2010.

[15] M. H. Awida and A. E. Fathy, "Design guidelines of substrate-integrated cavity backed patch antennas," *IET Microwaves, Antennas Propagation*, vol. 6, no. 2, pp. 151–157, 2012.

Chapter 6

Conclusions

The work presented in this thesis focused on a few different topics.

The systematic study of the compact SIW resonators has shown that the Half-Mode technique can be iterated to obtain very high levels of size reduction. However, all compact resonator topologies experience a noticeable drop in the quality factor compared to the traditional square SIW structures. An investigation on the loss mechanisms of the devices has shown that the main reason behind this phenomenon is the leakage of electromagnetic power from the open side of the component trough radiation. This effect is strongly dependent on the characteristics of the substrate. In particular, radiation losses are more pronounced on substrates with high thickness and low dielectric constant. This is because in these conditions a lower amount of electromagnetic field in confined inside the metal structure of the resonator. These effects are amplified at higher frequencies, since the substrate appears taller compared to the wavelength. However, SIW structures become naturally smaller as the frequency increases, and so the benefits of the compact topologies become lower. The use of the shielding metal wall near the open edge of the resonators can offer a visible increase in the performance with a low impact on the footprint of the components.

The filters that combine SIW and microstrip resonators to obtain wide spurious-free bands and special routing topologies prove the high level of versatility and integration that can be achieved using this technology.

The amplitude based reconfigurable array configuration has been developed with the intent of minimizing the complexity of the system. By removing as many control elements as possible and employing mostly passive, fixed power transmission networks it is possible to decrease the fabrication costs of the array, making it appealing for applications with large volumes of production. The trade-off is a reduction in the antenna efficiency and a limit on the maximum achievable steering range depending on the required directivity. The SIW technology complements the array topology by providing high quality radiating and power routing elements. The SIW cavity-backed

arrays presented in the work have been designed for high frequency 5G base station applications. Another possible application field is in automotive radars. Further research can lead to the improvement of the performance of amplitude-based reconfigurable arrays, for example with the implementation of hybrid multi-stage phased arrays of amplitude-based radiators.

Appendix A

Appendix

During the three years of PhD activity, some collaborations with research groups from different departments and universities involved the realization of a number of microwave components and publications. This chapter will present the results of these side projects.

A.1 Microwave sensors

A collaboration between the Microwave Laboratory of the University of Pavia and the Department of Microwave and Antenna Engineering of the Gdansk University of Technology was aimed at the design of a few microwave sensors.

A.1.1 CSRR-based angular displacement sensor

The first structure to be developed in an angular displacement sensor based on the interaction between a microstrip line an a Complementary Split-

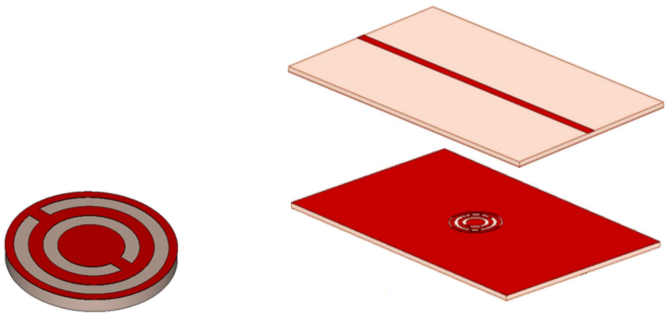

(a) CSRR topology (b) CSRR sensor layout

Figure A.1: Layout of the CSRR angular displacement sensor

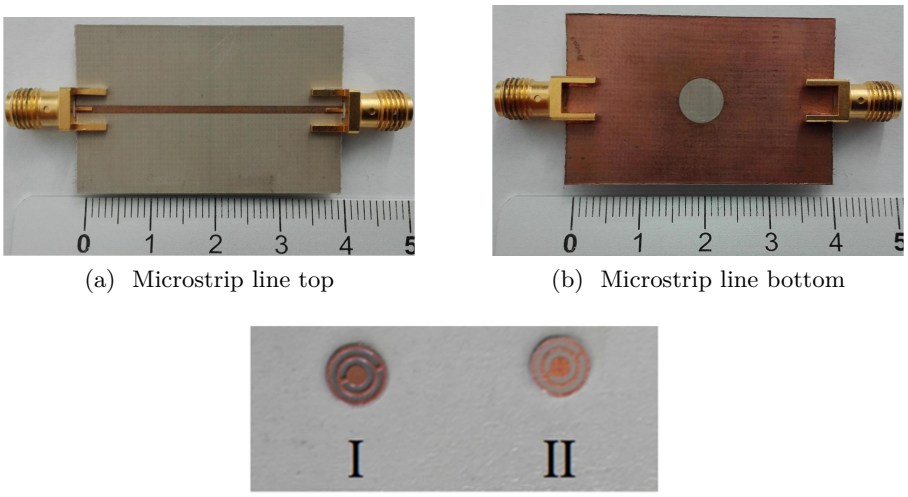

(a) Microstrip line top

(b) Microstrip line bottom

(c) CSRR rotors

Figure A.2: Pictures of the prototype of the CSRR angular displacement sensor

Ring Resonator (CSRR). CSRRs are simple resonant structures that can be commonly found in filter [1] or sensor [2] applications. Figure A.1a shows the topology of the employed CSRR. It consists in a circular metallic structure with a pattern etched into it. The metal is supported by a small dielectric substrate disk.

The CSRR can be coupled to a microstrip line with the configuration shown in figure A.1b. The CSRR acts as a defect in the bottom metal layer of the microstrip. The response of the microstrip shows a reflection peak at the frequency of resonance of the CSRR. The coupling between the transmission line and the resonator has a capacitive and an inductive contribution. The amount of inductive coupling depends on the orientation between the CSRR and the microstrip. By modifying the rotation angle, the frequency of the reflection peak will change. By measuring the frequency response of the line is then possible to infer the orientation of the resonator.

Figure A.2 shows a picture of the prototype of the sensor. The microstrip like acts as a stator, while the CSRR is the rotor. A circular hole has been etched on the bottom metallization layer of the transmission line in the region where the rotor must be placed. The design of the component has been conducted in the Gdansk University, while the fabrication and measurement of the device was done in Pavia. The results (figure A.3) show good agreement between simulations and measurements. Compared with other kind of similar sensors, the device shows a good level of sensitivity

The development of this component resulted in the following publication: [3].

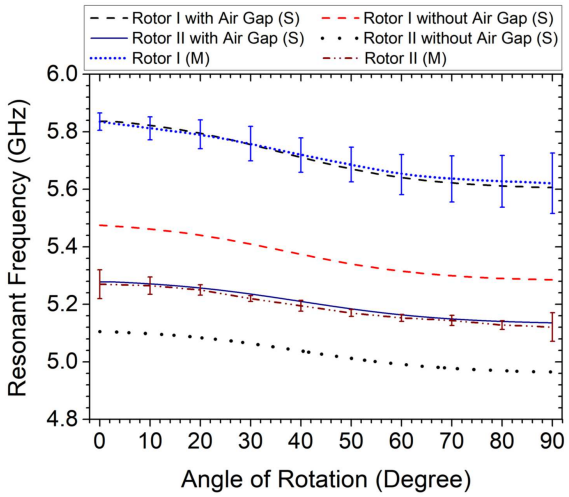

Figure A.3: Measurements of the CSRR angular displacement sensor

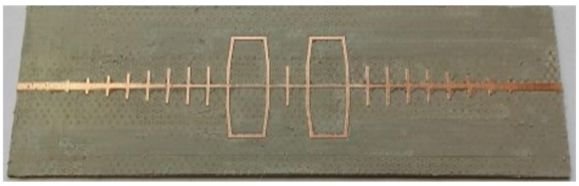

Figure A.4: Prototype of the dielectric sensor based on Bragg reflection

A.1.2 Dielectric sensor with Bragg reflector

Another component resulting from the collaboration is a dielectric sensor based on a periodic topology. Bragg reflection is a phenomenon commonly used at optical frequency for the creation of mirrors and filters. In the microwave regime, a Bragg reflector consists of a transmission line modified with periodical deformations [4].

The proposed design can be seen in figure A.4. The base structure is a simple microstrip line, loaded with side stubs. The layout has been modified with the introduction of two hexagonal line structures. The component shows three different pass-band behaviours, which depend on different design parameters such as the length and distance between the stubs and the size of the hexagonal lattice. In particular, the central pass-band region is mainly controlled by the length of the stub placed in the middle of the structure. The electrical length of the stubs can be artificially modified by placing a sample of dielectric material above it. In this way, the properties of the sample can be extracted from the shift of the pass-band frequency.

The component has been manufactured in Pavia and measured in Gdansk. The results table A.1 show linear behaviour and high sensitivity. The design and characteristics of this sensor have been published in [5].

Material under test	Dielectric constant	Resonant frequency (GHz)	Frequency shift (MHz)
TMM-3	3.45	6.0625	97.5
Kappa-438	4.38	6.0325	112.5
CER-10	10	5.9325	227.5
TMM-13i	12.2	5.8925	267.5

Table A.1: Measurement of dielectric samples with Bragg reflection based sensor

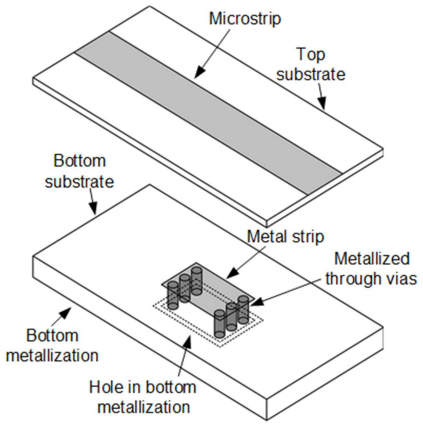

Figure A.5: Layout of the MNZ magnetodielectric sensor

A.1.3 Mu-Near-Zero magnetodielectric sensor

The last device is a particular kind of sensor for the measurement of electric and magnetic properties of a sample. The component is based on the Mu-Near-Zero (MNZ) effect. A MNZ transmission line section presents a quasi-static magnetic field distribution, with no phase variation along it. This kind of behaviour can be obtained by abrupt variations in the height of a microstrip transmission line.

Figure A.5 shows the topology of the sensor. The jump in the thickness of the substrate has been emulated by employing a dual-layer configuration. The metallic patch in the middle of the structure is not connected to the metallic vias. The electric field tends to be confined in the top substrate due to the capacitive effect of the internal patch, while the magnetic field is more intense in bottom substrate. Part of the magnetic field is extracted through some cuts placed in the bottom metal layer.

The frequency response of the microstrip line presents a transmission zero. By placing a material sample near the bottom metal layer hole, the position of the zero can be shifted. This behaviour can be used to extract

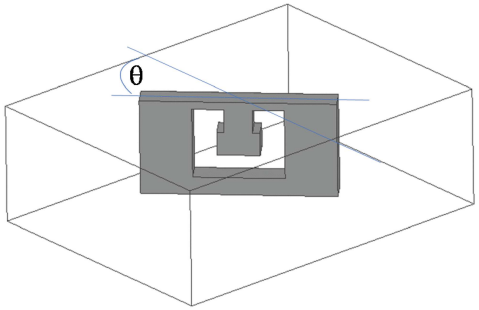

Figure A.6: Topology of the slanted ridge resonator

the magnetic properties of the material.

Once again, the sensor has been designed and measured in Gdansk and fabricated in Pavia. The results have been published in [6].

A.2 Additive manufacturing for microwave applications

Additive manufacturing technologies allow for the cheap, fast and reliable fabrication of complex mechanical structure. 3-D printing has found applications in multiple engineering fields, such as the automotive [7] and aerospace [8] sectors.

In the case of microwave and RF applications, additive manufacturing can be used to create non-planar components and prototypes in a cost-effective way. Recently, this topic has become the subject of intense research activity. The design of 3-D printed antennas [9] and filters [10] can be found in the literature.

These new manufacturing technologies enable the realization of new and complex microwave structures which would be unfeasible with classic methods. This section will present the design of a few of such structures. The fabrication of these devices has been made in collaboration with the Department of Civil Engineering and Architecture of the University of Pavia.

A.2.1 Slanted ridge resonators

The first component is a slanted ridge waveguide resonator. The topology of the resonator can be seen in figure A.6. The structure is intended to be placed inside a rectangular waveguide. The topology has been obtained by modifying a classic capacitive iris. First, a C-shaped slot is carved in the middle of the structure. Then, the iris is rotated around the central axis of the transmission line. This structure has two resonant The structure exhibits two resonant behaviours: one is related to the slot in the metal, while the

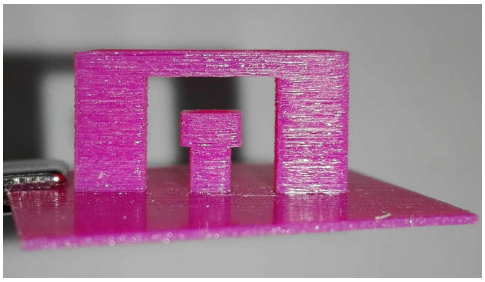

(a) Picture of the prototype

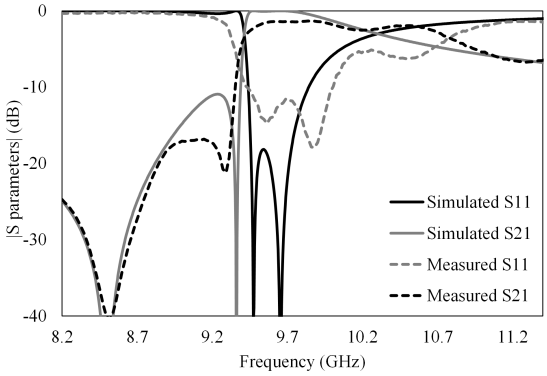

(b) Measurements

Figure A.7: Slanted ridge resonator prototype

other involves the gap between the iris and the walls of the waveguide. The interaction between the resonator and the travelling TE_{10} mode results in a frequency response with two poles and two finite transmission zeroes. The response can be tuned by acting on the physical dimensions and rotation of the iris and the slot. The topology of this resonator is extremely difficult to obtain with classical fabrication technologies. Instead, 3-D printing can be used to realize the slanted irises, which can then be inserted in a standard metallic waveguide.

There are many different types of additive manufacturing methods [11]. Some of them, such as the Direct Metal Laser Sintering (DMLS), can directly fabricate a metallic structure. However, these techniques are expensive, and the resulting components do not reach the amount of spatial precision required for microwave applications. Moreover, the surface roughness of 3-D printed metal components may degrade the electromagnetic performance.

A different approach consists in the creation of a plastic model of the component. The exterior of the structure can then be copper-plated via galvanic electrodeposition. The technologies for 3-D printing of plastic polymers are more refines, less expensive and can reach an high level of spatial resolution. Figure A.7a shows a prototype before the metallization process.

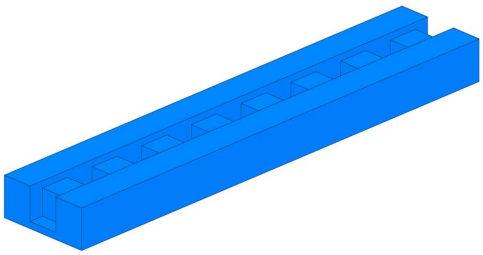

Figure A.8: Topology of the Bragg reflector bandpass filter

The component has been fabricated with the material jetting technology. This method allows for the simultaneous printing of two different plastic materials. One of them acts as a support that assists in the realization of the slot, and has later been removed. The resulting component is a faithful recreation of the desired model.

The metallization of the device is made in two steps. First, the plastic component is covered with a conductive silver-based paint. Care should be applied to obtain an even coating along the entire surface. Particular attention should be placed on the internal angles and faces of the structure. After letting the paint dry, the component is then metallized using a classic galvanic electrodeposition process.

The results presented in figure A.7b show that the printed structure follows the behaviour of the simulated model. The noisy behaviour of the measurements can be attributed to fabrication imperfections, indicating that the component building and metallization process can be further refined. The results have also been published in [12, 13].

A.2.2 Bragg bandpass filter

As it was discussed in the previous section, Bragg reflectors are periodic structures that show strong reflection in certain frequency bands. A rectangular waveguide can be modified by placing a ridge along its middle axis. If the height of the ridge is modified periodically, then the transmission line will experience Bragg reflection effects. This can be exploited for the creation of bandpass filters.

The layout of the proposed structure can be seen in figure A.8. The bandwidth of the filter depends on the amount of difference between the height of the ridges, while the frequency of the pass-band is controlled by the period of the perturbation. The length of the structure has an effect on the selectivity and the out-of-band signal rejection rate.

While the topology of the device is simple to describe, its realization using standard manufacturing techniques like mechanical milling is long and complex. Instead, this topology can easily be fabricated with 3-D printing technology. The finished prototype of the filter can be seen in figure

Figure A.9: Prototype of the Bragg reflector bandpass filter

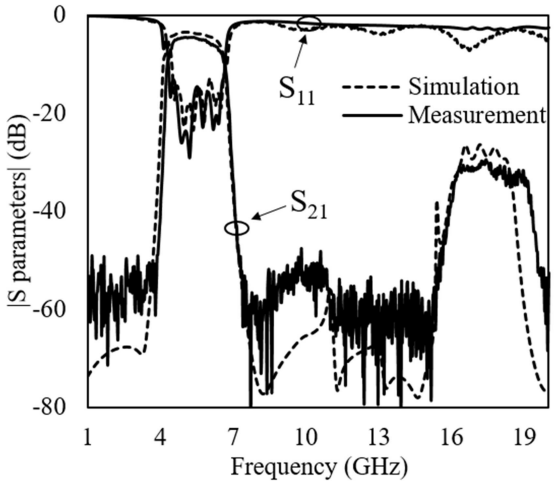

Figure A.10: Measurements of the Bragg reflector bandpass filter prototype

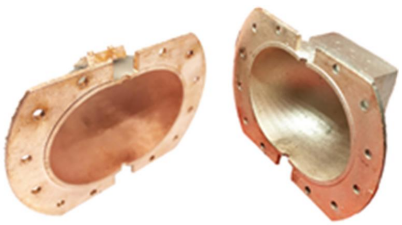

Figure A.11: Pictures of the pumpkin-shaped resonator

A.9. The device has been fabricated using a simple Fused Deposition Manufacturing (FDM) machine. The chosen material is a PLA filament with dielectric permittivity $\epsilon_r = 2.8$ and loss tangent $\tan\delta = 0.02$. In this case, the plastic material support acts as the interior of the device. For this reason, the filter will experience higher losses compared to one based on empty rectangular waveguides. The additive manufacturing technology offers a trade-off between fabrication cost and electromagnetic performance. The measurements of the device (figure A.10) confirm the validity of the design.

The results of this work have been published in [14].

A.2.3 Pumpkin-shaped resonator for dielectric sensor applications

The cavity perturbation method is one of the most reliable techniques for the characterization of dielectric materials [15]. It consists in the measurement of the shift of resonant frequency that a cavity experiences when a dielectric sample is introduced inside. From this shift, the dielectric permittivity of the material can be obtained. More refined systems can also detect a change in the quality factor of the resonator, in order to extract the amount of losses given by the sample.

The sensitivity and precision of such devices is affected by the quality factor of the employed cavity. The technologies that allows for the creation of resonators with the highest value of Q are the circular and rectangular waveguides. However, waveguide cavities are typically bulky and expensive to fabricate. By creating these components using additive manufacturing technologies, it is possible to decrease the cost and weight of the sensors.

The spherical cavities shown in figure A.11 have been developed for the characterization of fluids. In order to maximise the quality factor of the resonator, it has to be empty. The structure has been split in two halves in order to have an access to the inner parts of the cavity, allowing the metallization of the internal walls. The device has been fabricated with a stereolithographic (SLA) process: this ensures an high level of precision and smoothness of the cavity walls. The name of pumpkin-shaped resonator comes from its topology: the poles at the top and bottom of the sphere have been slightly compressed, isolating the resonant mode used for the measurement from the others. During operation, a liquid is inserted in the cavity through a small 3-D printed pipe. The system that employs the presented cavity resonator can extract the dielectric and loss parameters of the liquid within an error of 5%. The results have been presented in [16].

References

[1] F. Wei, P. Qin, Y. J. Guo, C. Ding, and X. W. Shi, "Compact balanced dual- and tri-band BPFs based on coupled complementary split-ring resonators (C-CSRR)," *IEEE Microwave and Wireless Components Letters*, vol. 26, no. 2, pp. 107–109, 2016.

[2] N. K. Tiwari, Y. Tiwari, and M. J. Akhtar, "Design of CSRR-based electronically tunable compact RF sensor for material testing," *IEEE Sensors Journal*, vol. 18, no. 18, pp. 7450–7457, 2018.

[3] A. K. Jha, N. Delmonte, A. Lamecki, M. Mrozowski, and M. Bozzi, "Design of microwave-based angular displacement sensor," *IEEE Microwave and Wireless Components Letters*, vol. 29, no. 4, pp. 306–308, 2019.

[4] T. Lopetegi, F. Falcone, and M. Sorolla, "Bragg reflectors and resonators in microstrip technology based on electromagnetic crystal structures," *International Journal of Infrared and Millimeter Waves*, vol. 20, no. 6, pp. 1091–1102, 1999.

[5] A. K. Jha, M. Mrozowski, N. Delmonte, A. Lamecki, and M. Bozzi, "Planar microwave bragg reflector resonant dielectric sensor," in *2019 IEEE MTT-S International Microwave Workshop Series on Advanced Materials and Processes for RF and THz Applications (IMWS-AMP)*, pp. 160–162, 2019.

[6] A. K. Jha, M. Mrozowski, N. Delmonte, A. Lamecki, and M. Bozzi, "Novel MNZ type microwave sensor for testing of magnetodielectric materials," *Scientific reports*, vol. 10, no. 16985, 2020.

[7] R. Lwal, F. M. Barreiros, L. Alves, F. Romeiro, J. C. Vasco, M. Santos, and C. Marto, "Additive manufacturing tooling for the automotive industry," *The International Journal of Advanced Manufacturing Technology*, vol. 92, no. 5, pp. 1671–1676, 2017.

[8] C. W. J. Lim, K. Q. Le, Q. Lu, and C. H. Wong, "An overview of 3-D printing in manufacturing, aerospace, and automotive industries," *IEEE Potentials*, vol. 35, no. 4, pp. 18–22, 2016.

[9] S. Zhang, D. Cadman, and J. Y. C. Vardaxoglou, "Additively manufactured profiled conical horn antenna with dielectric loading," *IEEE Antennas and Wireless Propagation Letters*, vol. 17, no. 11, pp. 2128–2132, 2018.

[10] C. Tomassoni, G. Venanzoni, M. Dionigi, and R. Sorrentino, "Compact quasi-elliptic filters with mushroom-shaped resonators manufac-

tured with 3-D printer," *IEEE Transactions on Microwave Theory and Techniques*, vol. 66, no. 8, pp. 3579–3588, 2018.

[11] V. Dwivedi, M. Raj, A. Yadav, and A. K. Sharma, "Additive fabrication and additive technique: A survey," in *2019 4th International Conference on Information Systems and Computer Networks (ISCON)*, pp. 395–399, 2019.

[12] C. Tomassoni, L. Silvestri, N. Delmonte, M. Bozzi, L. Perregrini, S. Marconi, G. Alaimo, and F. Auricchio, "A new class of doublet based on slotted slant ridge in additive manufacturing technology," in *2019 IEEE MTT-S International Microwave Workshop Series on Advanced Materials and Processes for RF and THz Applications (IMWS-AMP)*, pp. 10–12, 2019.

[13] C. Tomassoni, L. Silvestri, N. Delmonte, M. Bozzi, L. Perregrini, S. Marconi, G. Alaimo, and F. Auricchio, "Different strategies for the additive manufacturing of slotted slant ridge filtering doublet," in *2019 IEEE MTT-S International Microwave and RF Conference (IMARC)*, pp. 1–3, 2019.

[14] H. García-Martínez, E. Ávila-Navarro, G. Torregrosa-Penalva, N. Delmonte, L. Silvestri, S. Marconi, G. Alaimo, F. Auricchio, and M. Bozzi, "Design and fabrication of a band-pass filter with EBG single-ridge waveguide using additive manufacturing techniques," *IEEE Transactions on Microwave Theory and Techniques*, vol. 68, no. 10, pp. 4361–4368, 2020.

[15] L. F. Chen, C. K. Ong, C. P. Neo, V. V. Varadan, and V. K. Varadan, *Microwave Electronics: Measurement and Materials Characterization*. Wiley, 2004.

[16] G. M. Rocco, N. Delmonte, D. Schreurs, S. Marconi, F. Auricchio, and M. Bozzi, "3D-printed pumpkin-shaped cavity resonator to determine the complex permittivity of liquids," *Microwave and Optical Technology Letters*, vol. 63, no. 4, pp. 1061–1066, 2021.

Appendix B

List of Publications

Journals

[1] N. Delmonte, L. Silvestri, M. Bozzi, and L. Perregrini, "Compact half-mode SIW cavity filters designed by exploiting resonant mode control," *International Journal of RF and Microwave Computer-Aided Engineering*, vol. 26, pp. 72–79, Sept 2016.

[2] A. K. Jha, N. Delmonte, A. Lamecki, M. Mrozowski, and M. Bozzi, "Design of microwave-based angular displacement sensor," *IEEE Microwave and Wireless Components Letters*, vol. 29, pp. 306–308, April 2019.

[3] Y. Zhou, H. Jin, Y. M. Huang, S. Ding, D. Xu, N. Delmonte, M. Bozzi, and L. Perregrini, "An effective mixed extracting method for electromagnetic parameters of periodically loaded substrate integrated waveguide units and its applications," *IEEE Transactions on Microwave Theory and Techniques*, vol. 68, pp. 543–554, Feb 2020.

[4] H. García-Martínez, E. Ávila-Navarro, G. Torregrosa-Penalva, N. Delmonte, L. Silvestri, S. Marconi, G. Alaimo, F. Auricchio, and M. Bozzi, "Design and fabrication of a band-pass filter with EBG single-ridge waveguide using additive manufacturing techniques," *IEEE Transactions on Microwave Theory and Techniques*, vol. 68, pp. 4361–4368, Oct 2020.

[5] A. K. Jha, M. Mrozowski, N. Delmonte, A. Lamecki, and M. Bozzi, "Novel MNZ type microwave sensor for testing of magnetodielectric materials," *Scientific reports*, vol. 10, no. 16985, 2020.

[6] G. Macchiarella, G. Gentili, N. Delmonte, L. Silvestri, C. Tomassoni, L. Perregrini, M. Mrozowski, and M. Bozzi, "Accurate modeling of stubs used as resonant coupling elements in SIW filters," *IEEE Microwave and Wireless Component Letters*, vol. 30, no. 12, pp. 1125–1128, 2020.

[7] N. Delmonte, C. Tomassoni, L. Perregrini, and M. Bozzi, "Modified quarter-mode substrate integrated waveguides cavities: Performance study and application to filters," *International Journal of RF and Microwave Computer-Aided Engineering*, vol. 31, no. 3, p. e22524, 2021.

[8] G. M. Rocco, N. Delmonte, D. Schreurs, S. Marconi, F. Auricchio, and M. Bozzi, "3D-printed pumpkin-shaped cavity resonator to determine the complex permittivity of liquids," *Microwave and Optical Technology Letters*, vol. 63, no. 4, pp. 1061–1066, 2021.

Conferences

[1] S. Moscato, N. Delmonte, L. Silvestri, M. Bozzi, and L. Perregrini, "Half-mode versus folded SIW filters: Modeling and design," in *2015 IEEE MTT-S International Conference on Numerical Electromagnetic and Multiphysics Modeling and Optimization (NEMO)*, pp. 1–3, Aug 2015.

[2] S. Moscato, N. Delmonte, L. Silvestri, M. Pasian, M. Bozzi, and L. Perregrini, "Compact substrate integrated waveguide (SIW) components on paper substrate," in *2015 European Microwave Conference (EuMC)*, pp. 24–27, Sep. 2015.

[3] M. Bozzi, S. Moscato, L. Silvestri, N. Delmonte, M. Pasian, and L. Perregrini, "Innovative SIW components on paper, textile, and 3d-printed substrates for the internet of things," in *2015 Asia-Pacific Microwave Conference (APMC)*, vol. 1, Dec 2015. invited paper.

[4] S. Moscato, L. Silvestri, N. Delmonte, M. Pasian, M. Bozzi, and L. Perregrini, "SIW components for the internet of things: Novel topologies, materials, and manufacturing techniques," in *2016 IEEE Topical Conference on Wireless Sensors and Sensor Networks (WiSNet)*, pp. 78–80, Jan 2016. invited paper.

[5] M. Bozzi, S. Moscato, L. Silvestri, E. Massoni, N. Delmonte, G. M. Rocco, M. Pasian, L. Perregrini, and C. Tomassoni, "Novel materials and fabrication technologies for SIW components for the internet of things," in *2016 IEEE International Workshop on Electromagnetics: Applications and Student Innovation Competition (iWEM)*, pp. 1–3, May 2016. invited paper.

[6] S. Moscato, L. Silvestri, N. Delmonte, M. Bozzi, L. Perregrini, and C. Tomassoni, "Compact filter solutions in substrate integrated waveguide (SIW) technology," in *2016 IEEE International Workshop on*

Electromagnetics: Applications and Student Innovation Competition (iWEM), pp. 1–3, May 2016. invited paper.

[7] M. Bozzi, N. Delmonte, L. Silvestri, C. Tomassoni, and L. Perregrini, "Compact cavity resonators in substrate integrated waveguide (SIW) technology for rfid applications," in *Progress In Electromagnetics Research Symposium (PIERS 2017)*, Nov 2017. invited paper.

[8] N. Delmonte, C. Tomassoni, M. Bozzi, and L. Perregrini, "Compact resonators in substrate integrated waveguide technology," in *2018 IEEE MTT-S International Wireless Symposium (IWS)*, pp. 1–3, May 2018.

[9] E. Massoni, N. Delmonte, G. Macchiarella, L. Perregrini, and M. Bozzi, "Half-mode SIW filters with resonant couplings implementing transmission zeros," in *2018 IEEE/MTT-S International Microwave Symposium - IMS*, pp. 701–703, June 2018.

[10] N. Delmonte, M. Bozzi, L. Perregrini, and C. Tomassoni, "Cavity resonator filters in shielded quarter-mode substrate integrated waveguide technology," in *2018 IEEE MTT-S International Microwave Workshop Series on Advanced Materials and Processes for RF and THz Applications (IMWS-AMP)*, pp. 1–3, July 2018.

[11] N. Delmonte, M. Bozzi, L. Perregrini, and C. Tomassoni, "Miniaturization and quality-factor in substrate integrated waveguide cavities," in *2018 IEEE MTT-S International Conference on Numerical Electromagnetic and Multiphysics Modeling and Optimization (NEMO)*, pp. 1–4, Aug 2018.

[12] N. Delmonte, C. Tomassoni, M. Bozzi, and L. Perregrini, "Performance study of compact substrate integrated waveguide resonators," in *XXII Riunione Nazionale di Elettromagnetismo (XXII RiNEm)*, pp. 1–3, Sep. 2018.

[13] C. Tomassoni, N. Delmonte, G. Macchiarella, M. Bozzi, and L. Perregrini, "A technique for spurious suppression in substrate integrated waveguide filters," in *2018 48th European Microwave Conference (EuMC)*, pp. 753–756, Sep. 2018.

[14] N. Delmonte, M. Bozzi, L. Perregrini, and C. Tomassoni, "Miniaturized SIW filters based on shielded quarter-mode cavities," in *2019 IEEE MTT-S International Conference on Numerical Electromagnetic and Multiphysics Modeling and Optimization (NEMO)*, pp. 1–3, May 2019.

[15] A. K. Jha, M. Mrozowski, N. Delmonte, A. Lamecki, and M. Bozzi, "Planar microwave bragg reflector resonant dielectric sensor," in *2019 IEEE MTT-S International Microwave Workshop Series on Advanced*

Materials and Processes for RF and THz Applications (IMWS-AMP), pp. 160–162, July 2019.

[16] C. Tomassoni, L. Silvestri, N. Delmonte, M. Bozzi, L. Perregrini, S. Marconi, G. Alaimo, and F. Auricchio, "A new class of doublet based on slotted slant ridge in additive manufacturing technology," in *2019 IEEE MTT-S International Microwave Workshop Series on Advanced Materials and Processes for RF and THz Applications (IMWS-AMP)*, pp. 10–12, July 2019.

[17] A. K. Jha, M. Mrozowski, N. Delmonte, A. Lamecki, and M. Bozzi, "Novel MNZ type microwave sensor for testing of magnetodielectric materials," in *2019 IEEE Asia-Pacific Microwave Conference (APMC)*, Dec 2019.

[18] C. Tomassoni, L. Silvestri, N. Delmonte, M. Bozzi, L. Perregrini, S. Marconi, G. Alaimo, and F. Auricchio, "Different strategies for the additive manufacturing of slotted slant ridge filtering doublet," in *2019 IEEE MTT-S International Microwave and RF Conference (IMARC)*, pp. 1–3, Dec 2019.

[19] M. Bozzi, L. Silvestri, N. Delmonte, C. Tomassoni, and L. Perregrini, "Engineering the resonant cavities in substrate integrated waveguide technology," in *2019 IEEE MTT-S International Microwave and RF Conference (IMARC)*, pp. 1–5, Dec 2019. invited paper.